UNIVERSITY OF CALIFORNIA

Santa Barbara

Investigating Cellular Response to Compressive Injury with a Microfluidic MEMS Device

A dissertation submitted in partial satisfaction of the

requirements for the degree of

Doctor of Philosophy

in

Mechanical Engineering

by

Jennifer L Walker

Committee in charge:

Dean Kimberly L. Foster, Chair

Professor Adele M. Doyle

Professor Megan T. Valentine

Professor Beth Pruitt

Professor Kenneth S. Kosik

March 2021

The dissertation of Jennifer L Walker is approved.

_____

Adele M. Doyle

_____

Megan T. Valentine

_____

Beth Pruitt

_____

Ken Kosik

_____

Kimberly L. Foster, Committee Chair

March 2021

Investigating Cellular Response to Compressive Injury with a Microfluidic MEMS Device

by

Jennifer L Walker

ACKNOWLEDGEMENTS

I feel very lucky to have so many supportive people in my life throughout this experience.

I'd like to first thank my Ph.D. advisor, Dean Kimberly Foster, for giving me the opportunity to work on the coolest project! I loved being your first bioengineering student and (maybe) last graduate student. You were always encouraging and optimistic, which was so vital during the seemingly endless hurdles.

I'd also like to thank John Foster for inviting me into Owl. Beyond the opportunity to work with such impressive technology, Owl also is a wonderful community of researchers and engineers. It was invigorating to have a glimpse of my future industry, with supportive and excited co-workers who were so generous with their time and crucial in my project.

To Professor Adele Doyle, I cannot thank you enough for taking me into your lab. I tried to adopt as much of your methods as possible – from organization to structured, methodical troubleshooting. I'm not at all a molecular biologist, but I do feel like a stronger scientist thanks to you. I would also like to thank Professors Beth Pruitt, Megan Valentine, and Kenneth Kosik. Your combined expertise and guidance helped shape this dissertation.

To my family who supported me unconditionally, I feel so lucky to have you. It was difficult being across the country, especially during COVID, but I never felt disconnected. Also, I'm looking forward to teaching you more basic biology.

To George, my best friend/boyfriend/running partner, you made this marathon possible. Not just because I've tried to emulate you and your work ethic, but because you lighten all the stressful days. You are my favorite two-body problem.

VITA OF JENNIFER L WALKER
January 2021

EDUCATION

2016 – 2021	Doctor of Philosophy in Mechanical Engineering University of California, Santa Barbara Graduate Emphasis in Bioengineering
2012 – 2016	Bachelor of Science in Bioengineering Rice University

PROFESSIONAL EMPLOYMENT

2016 – 2021	Graduate Research Fellow and Teaching Assistant Department of Mechanical Engineering, UC Santa Barbara Academic Advisor: Kimberly Foster
2014 – 2016	Undergraduate Research Assistant Department of Bioengineering, Rice University Research Advisor: Antonios G. Mikos
2015	Product Development Intern Owl biomedical

PUBLICATIONS

1. **J.L Walker,** L.H.C Patterson, E. Rodriguez-Mesa, K. Shields, J. Foster, M.T. Valentine, A. Doyle, K. Foster. "Controlled Single Cell Compression with a High Throughput MEMS Actuator" IEEE Journal of Microelectromechanical Systems, pp. 1-7 (2020).

2. L. Patterson, **J. Walker**, M.A. Navier, E. Rodriguez-Mesa, M. Hoonejani, K. Shields, J. Foster, M.T. Valentine, A. Doyle, K. Foster. "Inertial flow focusing: a case study in optimizing cellular trajectory through a microfluidic MEMS device for timing-critical applications" Biomedical Microdevices (2020).

3. L. Patterson, **J. Walker**, E. Rodriguez-Mesa, K. Shields, J. Foster, M.T. Valentine, A. Doyle, K. Foster. "Investigating cellular response with a microfluidic MEMS device," IEEE Journal of Microelectromechanical Systems, 29, pp. 14-24 (2020).

4. L. Patterson, **J. Walker**, E. Rodriguez-Mesa, K. Shields, J. Foster, M.T. Valentine, A. Doyle, K. Foster. "The micro-Hammer: Investigating cellular response to impact with a high throughput microfluidic MEMS device," Proceedings of the Solid-State Sensor, Actuator, and Microsystems Workshop, Hilton Head, SC (2018).

5. **J.L. Walker** and M. Santoro, "Processing and production of bioresorbable polymer scaffolds," in Bioresorbable Polymer for Biomedical Applications: From Fundamentals to Translational Medicine, G. Perale & J. Hilborn, Eds., Woodhead Publishing, 2017, pp. 181-203

6. M. Santoro, S.R. Shah, **J.L. Walker**, A.G. Mikos, "Poly(Lactic Acid) Nanofibrous Scaffolds for Tissue Engineering," Adv. Drug Delivery Rev., 107, pp. 206-212 (2016)

PUBLICATIONS IN PROGRESS

J.L Walker, et al., "Mechanically Sensitive Neuroinflammation Signaling Inhibited in Response to High Strain Rate Injury in Neural Progenitor Cells"

SELECTED ORAL PRESENTATIONS

1. **Walker, J.L.,** Patterson, L.H.C., Rodriguez-Mesa, E., Shields, K., Foster, J., Valentine, M.T., Doyle, A., Foster, K. (2019). The μHammer: A MEMS Device for High Throughput Traumatic Brain Injury. Biomedical Engineering Society (BMES) Annual Meeting, Oct 16-19, Philadelphia, PA.

2. **Walker, J.L.,** Patterson, L.H.C., Rodriguez-Mesa, E., Shields, K., Foster, J., Valentine, M.T., Doyle, A., Foster, K. (2019). UC Bioengineering Symposium, Jun 27-29, Merced, CA.

SELECTED POSTER PRESENTATIONS

1. Patterson, L.H.C.*, **Walker, J.L.*,** Rodriguez-Mesa, E., Shields, K., Foster, J., Valentine, M.T., Doyle, A., Foster, K. (2019). The μHammer: Investigating cellular ramifications of Traumatic Brain Injury. 4th Annual BRAIN Initiative Investigators Meeting, April 9-11, Washington, D.C. *co-presented

2. Patterson, L.H.C. *, **Walker, J.L. *,** Rodriguez-Mesa, E., Shields, K., Foster, J., Valentine, M.T., Doyle, A., Foster, K. (2018). The μHammer: Investigating cellular response to impact with a high throughput microfluidic MEMS device. Solid-State Sensors, Actuators and Microsystems Workshop, June 3-7, Hilton Head Island, SC. *co-presented

3. **Walker, J.L.,** Patterson, L.H.C., Rodriguez-Mesa, E., Foster, J., Doyle, A., Foster, K. (2018). The MEMS μHammer: Impacting Neuroscience One Cell at a Time. Biophysical Society Annual Meeting (BPS), Feb 17-21, San Francisco, CA.

SELECTED HONORS AND AWARDS

2018	Semi-Finalist – UCSB Grad Slam
2017	First Place – UCSB Mechanical Engineering Convocation Grad Slam

SELECTED SERVICE

2018 – 2021	Executive Board – Biomedical Engineering Society, UCSB chapter
2020	Co-organizer – Biotech Industry Talks Biomedical Engineering Society UCSB Center for Bioengineering
2019	Co-organizer – Biotechnology Industry Showcase Biomedical Engineering Society UCSB Center for Bioengineering

ABSTRACT

Investigating Cellular Response to Compressive Injury with a Microfluidic MEMS Device

by

Jennifer L. Walker

Traumatic Brain Injury (TBI) is a leading cause of death and disability worldwide, making it both a global health and economic problem. Despite extensive studies utilizing tissue-level injury models, there is still no effective neural therapeutic available to counteract the neurodegenerative cascade, or secondary injury mechanism, of TBI. In part, this is due to limited understanding of cell-level response to mechanical injury. Prior research has examined the effects of mechanical strain on individual cells, but these studies have involved low strains and low strain rates ($\varepsilon < 10\%$, $\dot{\varepsilon} < 100\ s^{-1}$) leaving a largely unexplored injury regime. Furthermore, many of these tools are low throughput (100s of cells per study) which limits the statistical significance of their findings. To more thoroughly explore the effects of cellular injury, a microfluidic and electromagnetically actuated MEMS device (the 'μHammer') was developed to apply high strains and high strain rates ($\varepsilon > 40\%$, $\dot{\varepsilon} = 200{,}000\ s^{-1}$) to individual cells in a high throughput manner (36,000 cells per minute). With this device, compressive strain was applied to human Neural Progenitor Cells (NPCs), which were then monitored for changes in viability and gene expression. Compression studies revealed TBI secondary injury mechanisms (cell death and apoptosis), mechanically sensitive neuroinflammation signaling elements, and a previously unexplored global expression signature. These results suggest that the μHammer device can be an invaluable tool for furthering the understanding of cellular response to mechanical injury.

TABLE OF CONTENTS

1 Introduction

1.1 Motivation

Traumatic Brain Injury (TBI) afflicts nearly 2.6 million people in the United States each year and is one of the leading causes of disability worldwide[1,2]. TBI is segmented into two injury categories: primary and secondary. Primary injury consists of the immediate damage acquired during the trauma, e.g. focal contusion and hemorrhage. Secondary injury is linked to the resulting biomolecular cascade occurring over minutes to weeks after the trauma and leading to neurodegeneration. Long term effects of TBI include memory loss, changes in behavior, and increased risk of developing Alzheimer's disease[3].

Previous *in vivo* mechanical injury studies have provided insight into the pathophysiology of the secondary injury, identifying injury responses such as increased inflammation and cell death[4], as well as indicators of neuroprotection and even neurogenesis[56]. These investigative methods injure the whole brain, which is comprised of neural, cardiovascular, and immune cells in order to understand the systemic physiologic effects[7]. They also typically apply a point force to a region of the brain and examine the effects of the surrounding tissue. This broad surveillance of injury is thereby complicated by its initial heterogenous cell population as well as the resulting gradient of injury throughout the tissues. Biomolecular effects of the applied load are then obscured due to the inherent noise of the system. It is thereby impossible to connect any cellular response to the source injury, isolated from the response of neighboring tissue.

Applying injury to cells in vitro allows the decoupling of cellular response between tissue types, but the current tools are either limited in range of injury parameters or, more importantly, their throughput of consistent and repeatable injury on single cells. This lack of understanding of

specific cell response to mechanical injury limits the design of effective cell-targeted therapies for mechanically induced, degenerative diseases like TBI.

To address this need for improved tools, we developed the μHammer, an electromagnetically actuated MEMS device that is capable of applying mechanical strain to individual cells *in vitro* at unprecedented high strain rates. The μHammer combines microfluidics with time-gated electromagnetic actuation to achieve high-throughput injury, allowing both single cell and population averages to be calculated. After compression, cells can be recovered and returned to culture, allowing their functions and properties to be monitored over time.

1.2 Organization of this Dissertation

This dissertation comprises seven chapters. The first chapter introduces the need for a tool that can apply injury to cells *in vitro*. The second chapter summarizes the current understanding of TBI disease cellular pathology as well as the provides an overview of previous tools used to injure cells in a controllable manner. This chapter characterizes these tools in regards of the two injury parameters, strain magnitude and strain duration. In the third chapter, I introduce the microfluidic MEMS device, the 'μHammer', as a novel tool for applying high throughput, single-cell compression. The fourth chapter describes the acute response of the Neural Progenitor Cells (NPC) across varied compression injuries supplied by the μHammer. In the fifth chapter, I explore the effect of the varied compressive injuries on the NPC transcriptome, focusing at a single injury timepoint. In the sixth chapter, I specifically examine the temporal response of key signaling pathways by both gene expression and protein expression. The seventh and final chapter summarizes the impact of the collective work and describes remaining areas of exploration possible with the μHammer.

1.3 Techniques

1.3.1 Flow cytometry

Flow cytometry is a high throughout technology that characterizes single cells and particles based on optical metrics[8]. Each cell flows past lasers and is analyzed based on the direction and intensity of the scattered light. Forward scatter (FSC) identifies the relative size of the passing cell and side scatter (SSC) identifies the cell's granularity. These two metrics can distinguish between cell types, such as activated T-cells from inactivated[9], and stem cell pluripotency[10].

The cells can also be analyzed based on their fluorescent emission when stained with fluorescent dyes or fluorescently conjugated antibodies. Cells can also be transfected to express fluorescent proteins. While FSC and SSC are independent of the laser wavelength, fluorescent analysis must be designed such that there is minimal overlap between emission wavelengths. Dichroic filters guide the emitted photons to specific detectors, typically filtering to specific wavelengths. Photomultiplier tubes (PMTs) convert the incident photons to an electric signal. Adjusting the voltage applied to a specific PMT raises or lowers the fluorescent signal accordingly.

When a cell population is characterized by flow cytometry, each detected cell is individually analyzed on its emission intensity at each wavelength of interest. Accumulating these intensities across thousands of cells in the measured population, the overall distribution can be compared across populations as well as identify sub-populations. The increased presence of known proteins of differentiation, for example, can indicate the ratio of enrichment of neurons compared to glial cells in a population by varied directed differentiation methods[11].

1.3.2 Fluorescently activated cell sorting

Fluorescently activated cell sorting (FACS) expands on the optical characterization technology of flow cytometry by isolating cell populations of interest. With multi-parameter analysis, specific

populations of cells within a larger, heterogenous population can be sequestered in a high throughput manner[12]. The cells are first centered in the channel by sheath flow then analyzed by flow cytometry. Based on the analysis, each cell is selected or rejected for subsequent isolation from the overall population. All cells are excreted into single droplets as they are ejected through the FACS nozzle and a charge is applied to the droplets containing the selected cells. All droplets pass between deflecting plates, such that charged droplets are redirected electrostatically into a separate collection vessel.

While some studies report there is no effect of electrostatic sorting on gene expression[13,14] or cell cycle[14], others report viability loss[15] and increased oxidative stress[16]. Conflicting reports continue to concern researchers, not wanting to introduce functional change into their populations of interest due to the hydrodynamic stress[17], estimated as high as 100 Pa[18] with shear rate[15] as high as 5×10^5 s^{-1}. As such, MEMS magnetic cell sorting (i.e. Milteny® Tyto® Cell Sorter) was introduced as an alternative to electrostatic sorting to remove the hydrodynamic stress on cells during sorting[19]. Instead, cells remain in suspension and are pressure driven through wide microfluidic channels. A magnetically actuated valve redirects chosen cells down a separate channel with minimal change in flow.

1.3.3 Probe-based hybridization assay

The probe-based assay provides simultaneous analysis of thousands of genes, enabling associations between the transcriptome and cell function[20]. The cellular transcriptome encompasses the RNA transcribed at the time of investigation. Typically only 5% of a cell's DNA is expressed at a given time and the central dogma of cell biology assumes transcribed RNA indicates translated protein. While protein expression is the most accurate indication for a cell's state, far more technology has built around RNA expression as it is a more robust molecule.

Probe-based technology first requires RNA to be reverse-transcribed into complementary DNA (cDNA), exchanging Uracil for Thymine, but otherwise a copy of the RNA sequence. The cDNA sequences are then hybridized to complementary sequences fixed on a glass surface. These complementary sequences are probes, specific to genes of interest and fixed at pre-determined locations along the surface. The cDNA with high complementary base pairs will bind more strongly to the probes and resist being washed away. After loosely adhered cDNA is washed away, fluorescent molecules are added that specifically binds the remaining cDNA. The intensity of the measured fluorescence, therefore, is relative to the amount of cDNA bound to the probes and this intensity can then be compared across arrays, each performed for separate samples.

2 Background

2.1 Basic Cell Mechanics

The cell is in a balance of tension and compression provided by long chains of cytoskeletal proteins (Figure 2.1). The cytoskeleton includes actin filaments, intermediate filaments, and microtubules. Actin filaments typically provide stabilizing structure by resisting tension with long connections from the plasma membrane to nucleus. Actin filaments are active in that the monomers polymerize and depolymerize quickly, enabling cell motility. Similar to actin, intermediate filaments stabilize the cell by resisting tension but are inactive. Microtubules are the largest cytoskeleton component and resist compression. They are also critical to cell division and cell trafficking.

Cells also communicate with each other through adherens proteins that propagate forces from one cell to the other. Integrin proteins connect the intracellular actin filaments to the extracellular matrix (ECM) environment of the cell, enabling mechanical transduction between cells and their

environment. Cells communicate and interact with their mechanical surroundings, through both sensing forces and stiffness[21] as well as producing forces. From adhering to a surface to transmigrating between cell-cell junctions, typical mechanical loads a cell will experience or generate are on the order of pN [22] and kPa [23–25].

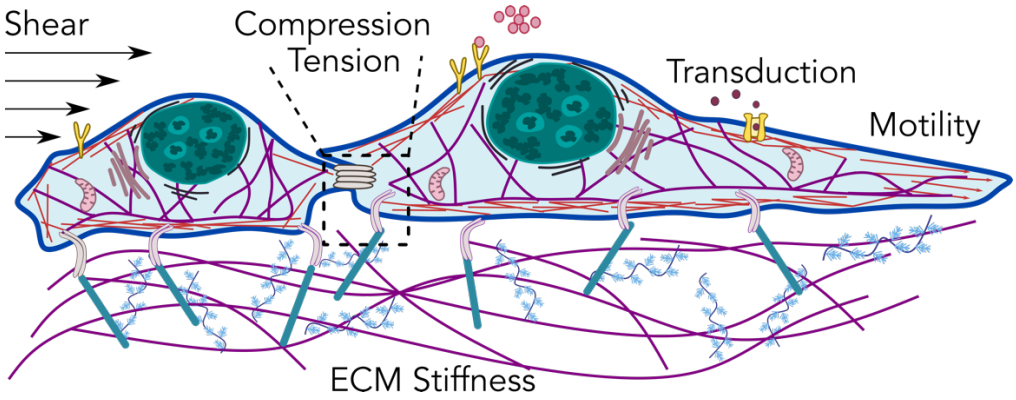

Figure 2.1 Cellular biomechanics enables sensing, transduction, and production of forces. Adapted from Haase (2015), cells perceive environmental mechanical cues such as shear stress, compression, and tension through mechanically sensitive proteins. These proteins can be located at the cell-ambient interface to detect fluid flow as well as at the cell-ECM interface, sensing substrate stiffness. Cell-cell junction proteins enable force transmission between neighboring cells. Cells will also respond to cues, by mechanical transduction influencing protein expression as well as produce forces through cytoskeletal organization, such as with cell motility.

The mechanical characterization of cell types, or mechano-phenotyping, is a relatively recent area of biological interest. Like any material, cells will deform predictably to applied force and stiffness measurements can be made. The mechanical forces can be tension, compression, and shear with the material responses described in terms of stress (σ), strain (ε), and Young's modulus (E) (Figure 2.2). The Young's modulus describes a materials resistance to deform under applied force, where an elastic material will deform linearly with stress. A viscoelastic material will deform linearly at low strain but non-linearly with increasing strain, it is also time- and frequency-

dependent.

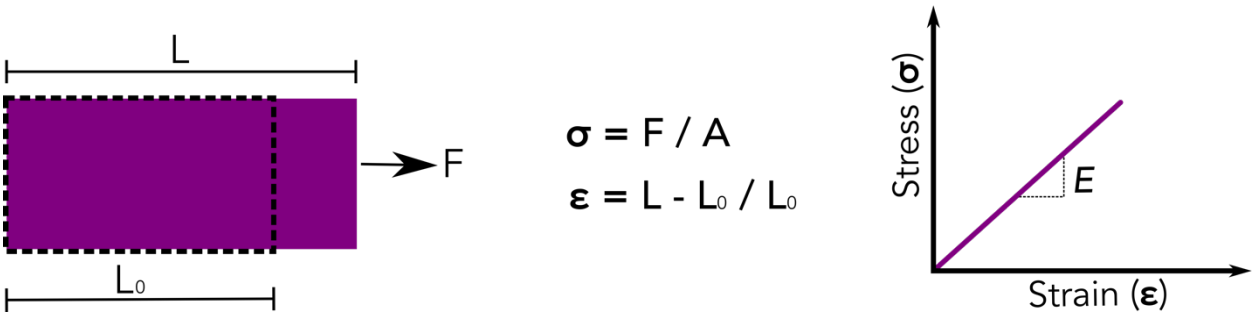

Figure 2.2 Stress versus strain for a linearly elastic material. When a force (F) is applied to the cross sectional area (A) of a linearly elastic material, the material will uniaxially deform in a stress-dependent manner. The ratio of the stress (σ) applied to the resulting strain (ε) is characterized by the Young's modulus.

A single cell is found to behave as a viscoelastic material. As such, the deformation depends on the rate of the applied stress, where higher strain rates correlate with higher modulus[26–30]. At very long time scales and low frequencies ($f < 100$ Hz), however, cells have behaved as a soft glassy material whereas at extremely high rates ($100 < f < 1000$ Hz) a pure viscus material (Figure 2.3) [31]. As a living material, a cell's stiffness will change when dead[32] and different cell types have been found to have unique mechanophenotypes[33,34], providing a novel characterization method for cell analysis as well as distinguishing disease states [35–40].

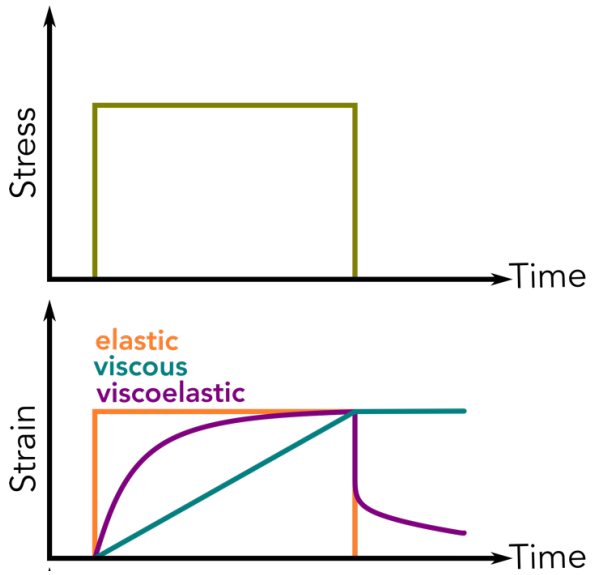

Figure 2.3 Material deformation in response to applied stress. Material deformation due to an applied load and load rate determines the modulus, or resistance to deformation, for that material. Elastic materials can be approximated as deforming linearly with increasing applied stress whereas a viscous and viscoelastic material will have a time-dependent response to the applied load.

As an active material, the downstream cellular response to an applied force is dependent to the applied strain and strain rate[27–29] and cells have coupled behavior change to their deformation. Cells interact with their environment mechanically, adjusting their movement, influencing differentiation pathways. Understanding the relationship between applied force and cellular response, therefore, is an important key in understanding cell state and disease progression.

2.2 Mechanosensing & Mechanotransduction

Similar to chemical sensing, cellular mechanical sensing is achieved through specialized proteins [26,41,42]. One subset are ion protein channels, which convert mechanical signals into electrochemical signals. Positioned across the lipid bilayer, these protein channels regulate the flux of small ionic molecules across the membrane. The family of Piezo ion channels, for example, respond to shear stress and tension applied to the cell membrane[43–45] and have been found to respond to applied force within milliseconds[46]. The two-pore domain K^+ channels (K2P) are

similarly sensitive to membrane stretch and tension[47], activated by pressures the order of kPa[48] but with slower reaction kinetics than the PIEZO proteins[47].

A second subset are proteins tethered, forming connections between the cytoskeleton and adherens or integrins proteins . When force channeled through to the tethered protein, it deforms. Deformation can expose or conceal a binding site, affecting many downstream signaling pathways[49,50].

Hair cells are especially sensitive to mechanical forces. These cells have specialized protrusions, arranged in according to length. The tip of each protrusion has a mechanically sensitive channel protein that is connected by a cytoskeletal filament to the taller neighbor. These mechanically sensitive channels have been recorded to respond to stress within 40 μs and predicted to respond in as little as 11 μs[51]. The response time of these channels have also been shown to be quicker when protrusion deflection is greater[52].

The focal adhesions at cell-cell and cell-ECM contacts contain many other proteins involved signaling cascades and forces transduced at these points become significant sources of cell signaling[53–55]. Mechanical cues are propagated faster than biochemical and can travel along the cytoskeleton up to 30 μm/s [56]. The components of a cell are connected by the cytoskeleton proteins, such that a force applied at the surface of the cell can displace an organelle up to 20 μm away[57].

Mechanical force can modulate nuclear architecture, thereby influencing transcription as well as epigenetics[50,58,59]. This is exemplified by stem cell differentiation, where stem cell fate is guided not just by biomolecular cues but also the stiffness of the microenvironment[50,34,60]. The nucleus has a mechanical structure unique to the rest of the cell (Figure 2.4). Nuclear nesprin proteins connect the outer nuclear membrane to cytoskeleton proteins residing in the cytoplasm. Woven lamin proteins supply structural integrity to the nucleus and are located under the inner nuclear

membrane. Nuclear pore complexes span the inner and outer nuclear membranes, regulating the transfer of molecules across.

Within the nucleus, DNA is organized by chromatin proteins. Tight packing of DNA limits transcription by restricting polymerase binding sites. Heterochromatin controls the dense packing of DNA and is found to connect to the cytoskeleton through the lamin proteins[61,62]. Forces applied at the plasma membrane, therefore, can transmit through the cytoskeleton to the nucleus and effect chromatin packing and gene expression[63]. The mechano-regulation of gene expression plays an important role in the direction of cell differentiation[64–69] as well as the progression of many diseases, such as Traumatic Brain Injury[70–91]

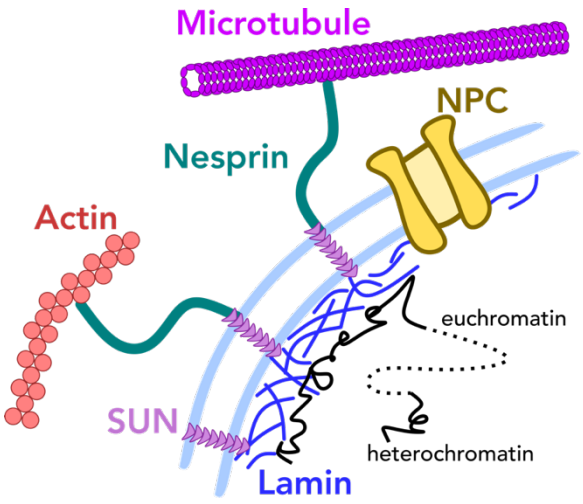

Figure 2.4 Nuclear mechanotransduction. Adapted from Maurer (2019), there are several proteins involved in the nuclear mechanotransduction. The cytoskeletal filaments, e.g. actin and microtubules, are linked to the outer nuclear membrane by nesprin proteins. The outer nuclear membrane is then connected to the inner membrane through SUN proteins, which transmit mechanical force to the nuclear lamin proteins. The lamin proteins interact with chromatin as well as nuclear pore complexes (NPCs).

2.3 Disease Motivation: Traumatic Brain Injury

Traumatic Brain Injury (TBI) is one of the leading causes of death and disability worldwide, making it a significant global health challenge and economic burden[1]. Common causes of TBI

include automobile accidents and falling. As such, nearly 40% of Americans will experience TBI within their lifetime[92] and one third will develop long-term disability[3,93], with neurological disability rates increasing with the severity of TBI[94].

The severity of TBI is commonly classified using the Glasgow Coma Scale. Within the first 48 hours of the injury, patients are assessed on their eye opening, verbal response, and motor response[95,96,70]. While 75-85% of TBIs are classified as 'mild', the long term effects associated will still cost the US nearly $17 billion each year[97].

The injury, whether due to blunt trauma, sudden acceleration, or blast exposure, translates force to the brain tissue, causing it to strain. Accelerometer data suggests the majority of the strain occurs within the corpus colosum[98,99] – the region of the brain that connects the two hemispheres and is located mid-depth of the brain. The resulting injury includes both damage to the structural integrity of the brain as well as functional loss. To distinguish between the mechanical damage to the tissue during the applied force and the molecular cascade that follows, the injuries have been categorized into primary and secondary TBI.

2.3.1 Primary Injury

The primary TBI injury occurs during the acceleration of the head and shearing of the brain tissue. While the injuring incident only occurs on the duration of milliseconds, clinical records outline resulting vascular damage such as hemorrhaging and contusions as well as axonal tearing[100]. These physiological changes can occur both at the point of impact as well as diffuse through the brain.

Axonal shearing or tearing, or diffuse axonal injury (DAI), is linked to increased risk for Alzheimer's Disease and Parkinson's Disease. The injury was found to be dependent both on strain

and strain rate during neuronal compression[101]. Injury has also led to reduced neural length[102], contributing to functional loss of excitatory neuronal signaling.

2.3.2 Secondary Injury

The primary injury initiates the secondary TBI injury, which takes place immediately after the applied load ceases. The secondary injury develops over time and functional loss can be detected years post-injury. A complex series of mechanisms yet to be fully understood, the secondary injury consists of dynamic changes to the cellular environment, encompassing damage to vascular, immune, and neural systems[103]. A subset of these changes include apoptosis, mitochondrial generation of reactive oxygen species (ROS), inflammation, and excitotoxicity [89,104,7,105].

Apoptotic cell death is a significant indicator of secondary TBI. The causing mechanism of apoptosis is not shown to be limited to a single pathway, as studies have found both caspase-dependence (intrinsic and extrinsic) as well as caspase independence [7,105]. Caspase-dependent apoptosis is likely due to the multi-faceted signaling cascades occurring within the cell whereas caspase-independent apoptosis is likely the result of the mitochondrial dysregulation.

Just as the cytoskeleton mechanically links the nucleus, other organelles such as the mitochondria are likewise susceptible to the chain of mechanical perturbation [106,107,108]. As the primary source of reactive oxygen species (ROS), dysregulation of the mitochondria can lead to damaging levels of ROS[109]. Mitochondrial proteins such as uncoupled protein receptor (UCP2), however, traditionally regulates free radical production[110] but after brain injury, UCP2 has been found to be overexpressed[111].

Brain inflammation is then initiated by the molecules released from dead and dying cells[112] and occurs within 24 hours of the trauma[103]. These molecules, DNA, RNA, ROS, and cellular debris, bind to specific receptors on the surface of microglia and astrocytes in the brain[103,113]. These

cells in turn release communication molecules such as cytokines to recruit immune cells[114]. "Dysregulation of the acute immune response" will maintain and further inflammation – resulting in cell death and dysfunction, with glial activation persisting years following the TBI.

Chronic activation of glial cells and astrocytes can result in neurotoxicity, as previously shown in degenerative diseases like Alzheimer's Disease and Parkinson's Disease[112,115]. Excitotoxicity describes a lethal increase in glutamate or aspartate –two primary neurotransmitters. Glutamate binds to the mechanical stretch-induced receptor, n-methyl-d-aspartate (NMDA), which in turn controls calcium influx[116]. Excessive calcium in the cell can activate apoptosis, promote free radical formation, and lead to DNA damage[115].

Neutrophils are the first immune cell type recruited, reaching the damaged tissue within hours to remove the cellular debris. As the activity of neutrophils tapers around day 3, monocytes and other immune cells are typically found up through 2 weeks after injury[117]. At the same time, activated microglial cells and astrocytes are recruited but remain at the injury site for months and years after the initial event [118]. Both cell types release factors found to be neuroprotective as well as damaging, such as promoting blood-brain-barrier permeability and chronic neurotixocity[112,119,120]. While both cell types are mechanically sensitive[121], previous research has focused on chemical activation, rather than by mechanical injury.

In addition to the many factors leading to neurodegeneration, there is also ample evidence of neurogenesis occurring as a result of TBI [122–126]. The subventricular zone (SVZ) of the brain, for example, has the ability to generate new neurons. After TBI, the neural progenitor cells (NPCs) in the SVZ will proliferate, migrate to the injury cite, and differentiate[127]. Located alongside the lateral ventricle and near the corpus collosum, the SVZ cells are likely mechanosensitive to the injury strain, causing mechanotransduction and their subsequent activation. Never the less, the vast

majority of studies focus on understanding the guiding relationship between molecules secreted from injured cells and SVZ cell activation and migration[128,129] rather than mechanical cues. One group recently, however, has shown that adult NSCs proliferation was induced by shear stress through a mechanically sensitive sodium channel[130].

In order to establish effective therapeutics that prevent or mitigate TBI brain degeneration as well as promote neurogenesis, comprehensive understanding of the secondary cascade is vital. Identifying the key regulators and pathways will discern effective drugs as well as optimal therapeutic windows. Unfortunately, this therapeutic has yet to be identified, in part due to the current methods of relating mechanical injury to cellular response.

2.4 Current in vivo methods of applying mechanical injury

A significant portion of our current understanding of the primary injury and second injury cascade is through accumulated results across *in vivo* experiments, spanning decades of TBI research. Using animal models, the injury conditions can be re-created to mimic several aspects of the human TBI pathophysiolgoy[131–133]. These methods can apply mechanical trauma through direct impact to the animal cranium as well as non-impact acceleration and percussive blast[134]. Animal models also enable further investigation into the behavioral and psychological ramifications of TBI. Many studies attempt to couple cognitive decline post-injury of specific animal samples to the tissue degeneration examined post-mortem[100].

2.4.1 Impact Methods

Two of the most common *in vivo* methods to apply direct impact force are fluid percussive injury (FPI), controlled cortical impact (CCI), with FPI as the most common model of TBI across all *in vivo* methods[135]. The FPI model creates a fluid pressure pulse on an intact dura of the animal. A pendulum strikes a piston, displacing the fluid held within the piston reservoir[136]. The FPI is

capable of inducing brain hemorrhage and swelling as well as damage to the grey matter of the brain[132,137–139]. The damaged tissue is then analyzed for secondary injury markers[140,141] and coordinated gene expression changes[73,77,82,87,90,142]. The height of the FPI pendulum is only mechanical parameter that can be changed across studies. The injury severity, therefore, is determined by fluid pressure pulse strength. Pneumatic actuation has been more recently adopted to provide improved injury repeatability[100] .

The CCI method provides more adaptable parameters for the applied injury. Typically a piston of set diameter is pneumatically driven into the brain at a specified velocity for a pre-determined dwell time and compression depth[143–146]. CCI can induce pathophysiology of TBI such as vascular degeneration change, axonal injury, concussion, behavioral changes, and cognitive decline[100,147]. Similar to FPI, the tissue can be used for gene expression analysis [72,81,83,85,86,89,148,149].

2.4.2 Non-Impact Methods

To understand the neurodegeneration resulting from acceleration of the brain alone, without the focal contusion, *in vivo* head acceleration models were also developed. Experimental setups include both free motion of the head as well as constrained, with the rotation generated using pneumatic shock. Depending on the experiment, the head will angularly displace within a few milliseconds and results in widespread DAI similar to that in human TBI[150]. The extent of tissue injury has been found scale with the rotational acceleration[151].

Blast chambers are also used to apply non-direct blast TBI. Anesthetized animals are held in a metal tube and pressure waves are created at one end using either explosives or compressed air. The peak pressure wave is typically kilopascal range and traverses the brain over microseconds to milliseconds[152], resulting in cytoskeletal damage, ROS generation, and cognitive dysfunction[84,100,153,154].

2.4.3 Limitations of in vivo TBI models

While critiques of using these models to better understand TBI include their inability to mimic clinical observations[132,155,156] and the inherent physiological differences between animal brain structure and organization and human[157,132], their main inadequacy in regards to this dissertation is their inability to apply controlled[139,158,159] and repeatable mechanical injury[160].

While unavoidable, all *in vivo* TBI models are limited by the heterogeneity and anisotropic nature of brain tissue[26]. A nonlinear viscoelastic material, the brain's deformation will depend on the rate of applied force[161]. Beyond this characterization, reported stiffness values of the brain can vary across experiments by several orders of magnitude[162]. In part, this is attributed to the location of the brain chosen for rheology measurements, as the local stiffness across the brain can depend on the ratio of white to grey matter present, as white matter is shown to be 39% stiffer[163]. There is also direction-dependence of white matter mechanical properties[164]. Without accurate mechanical characterization of the material injured in a TBI model, it is incredibly challenging to interpret the resulting tissue damage and functionality loss in terms of mechanical injury parameters.

This relation is further blurred, as each experiment using *in vivo* TBI models incorporates unique experimental parameters like injury probe geometry, tissue displacement, and loading rate. This is exemplified by a recent systematic review on the weight drop injury (WDI) model[165]. Comparing across over 400 WDI studies in rodents, the projectile weights ranged over two orders of magnitude and drop heights ranged over 3 orders of magnitude. The estimated injury force, therefore, ranged from μN to kNa and estimated pressure at the interface between the tip and tissue ranged from Pa to over MPa.

2.5 Current in vitro tools for applying mechanical injury

Efforts to discern the cellular effects of mechanical injury have expanded into the *in vitro* model system as well[166]. These tools enable higher control over the applied strain and simplify the material system to the cell-level. Previous single-cell sequencing performed post-FPI identified cell type-specific genetic alterations[142], suggesting *in vivo* tissue gene expression findings may be misrepresentative. Therefore, by exploring the injury effects on individual cell types, the resulting genetic changes identified are more resolved.

Five *in vitro* tools that have been used to apply mechanical stress or strain to cells include Atomic force microscopy (AFM), substrate stretch, microfluidic channels, and blast waves (Figure 2.6). Each tool offers explores a unique mechanical parameter regime as well as limitations, whether in yield or spatial control.

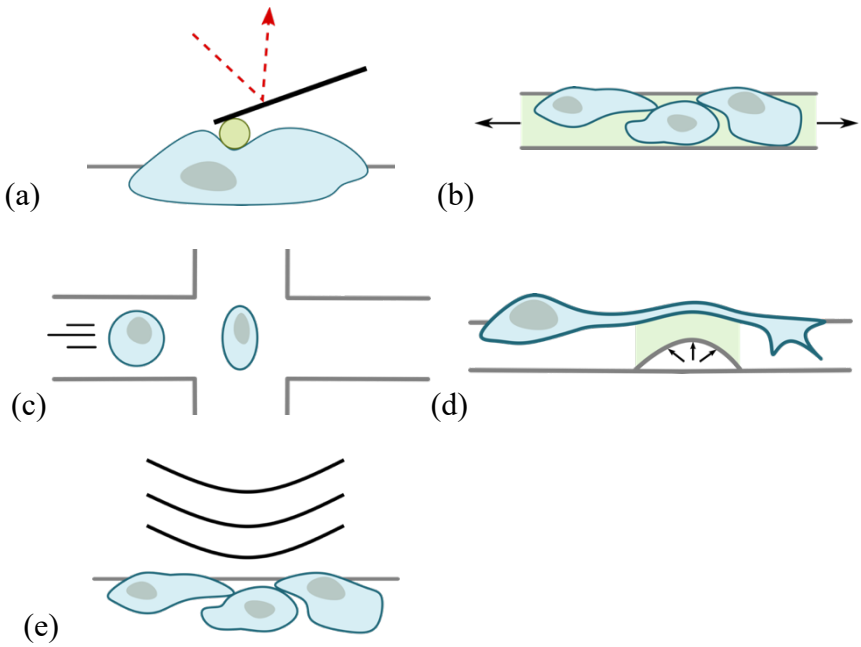

Figure 2.6: Depictions of *in vitro* mechanical perturbation methods reviewed in this chapter. (a) Atomic Force microscopy (b) Substrate stretch (c) Microfluidic rheometry (d) Microfluidic substrate stretch (e) blast wave.

2.5.1 Atomic Force Microscopy

Atomic force microscopy (AFM) is traditionally used for high resolution topography scanning[32]. A cantilever spring tipped either with a sphere or cone is lowered over the sample. The cantilever flexes – either due to electrostatic repulsion between the tip and the sample or direct contact. A beam of light is directed at the end of the cantilever, angled so the reflected beam is detected on a photodiode plane. As the cantilever flexes due to topography differences across the sample surface, the reflected beam will also be diverted, incident on a different location on the photodiode plane. In addition to topography measurement, AFM can be used to apply force to deform materials such as cells[167,168]. The known force applied on the cantilever coupled with the deflection of the tip is used to determine modulus.

While AFM studies have predominantly focused on examining the change in cell modulus post-TBI[32] rather than applying high strain magnitude or inducing cell injury, it has identified a

divergence in the effect of strain magnitude has on mitotic progression[169] as well as the degenerative effect of compression on axons over a 10 minute period[170]. In general, AFM is typically performed at extremely low strain rates and strains magnitudes. Most notable, however, is that the throughput of this technique is extremely low, with typical experimental sample size around 10 cells.

2.5.2 Substrate Stretch

Substrate stretch devices typically consist of adherent cells cultured on a stretchable membrane. Tensile stress is applied to the membrane through the use of motors or applied pressure. The use of stretchable substrates enables a wide range of tensile strain and strain duration on a large monolayers or three-dimensional culture of cell populations. While there strain magnitude is not limited with this method, there strain rate will rarely exceed 10^2 s^{-1}. Further, the specific strain applied to each cell is dependent on the cell's location along the plane of deformaton[171]. Therefore, despite enabling a larger population for study, the mechanical insult is still not completely controlled or consistent.

Due to the commercialized nature of the substrate stretch method, there have been many publications exploring the effects of tension across various cell types, each applying unique strain magnitude and duration. A select few, identified by the use of a neural cell type, applied tension ranging from 7 millisecond intervals to days-long (Figure 2.8). The strain magnitude applied was for the majority below 20%, with a few including strains above 100%. Typically, higher strain was compared to a spectrum of magnitudes, with 6 of the 10 studies comparing the effect of at least 2 magnitudes. Only 2 studies – Skotak (2012) and Feng (2018) – incorporated more than one strain duration. Feng (2018) found that at low strain (5%), longer duration (48 hours) induced senescence in cells whereas 24 hours or fewer did not[172]. Meanwhile a higher strain (20%), stretch

induced senescence occured in as few as 6 hours of strain duration. Skotak (2012) compared strain durations as short as 7 ms to as long as 50 ms, with strain magnitude ranging from 10 % to 140%, but did not design their experiment in a way that enabled decoupling of the effect of the two parameters[173].

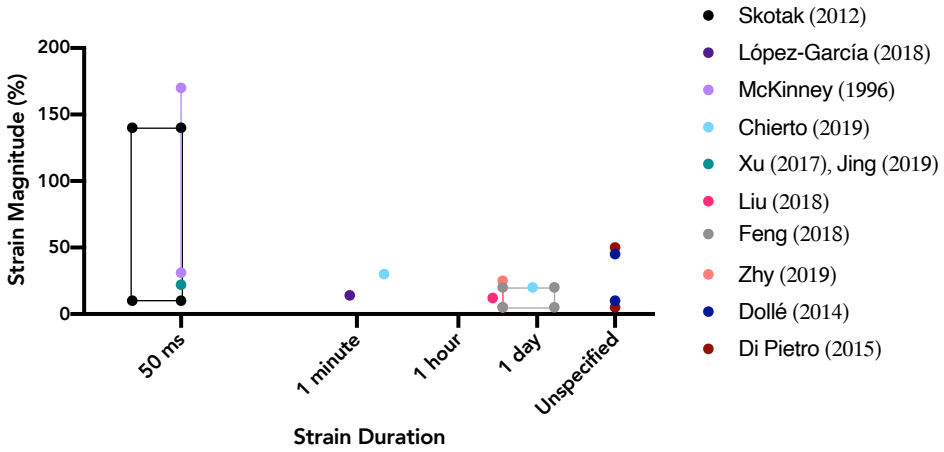

Figure 2.8: Mechanical parameters for selected *in vitro* substrate stretch publications [172–182]. A subset of *in vitro* substrate stretch publications, identified by neurologically related cell type choice, are represented by mechanical injury parameters: strain magnitude and strain duration. Points represent specified strain magnitudes and strain durations (if applicable). Lines connecting points reflect the range of either parameter explored by the researchers. While there are several publications that investigated the genetic response to substrate stretch, these were excluded from the comparison.

The findings identified by each of the 10 publications are varied across 11 categories of cellular response, but in aggregate reflect the secondary injury cascade of TBI (Figure 2.9). Viability loss of strained cells is the most common finding across the publications, investigated in 3 separate cell types. The second most common finding is the generation of ROS, again from investigations varied across 3 different cell types.

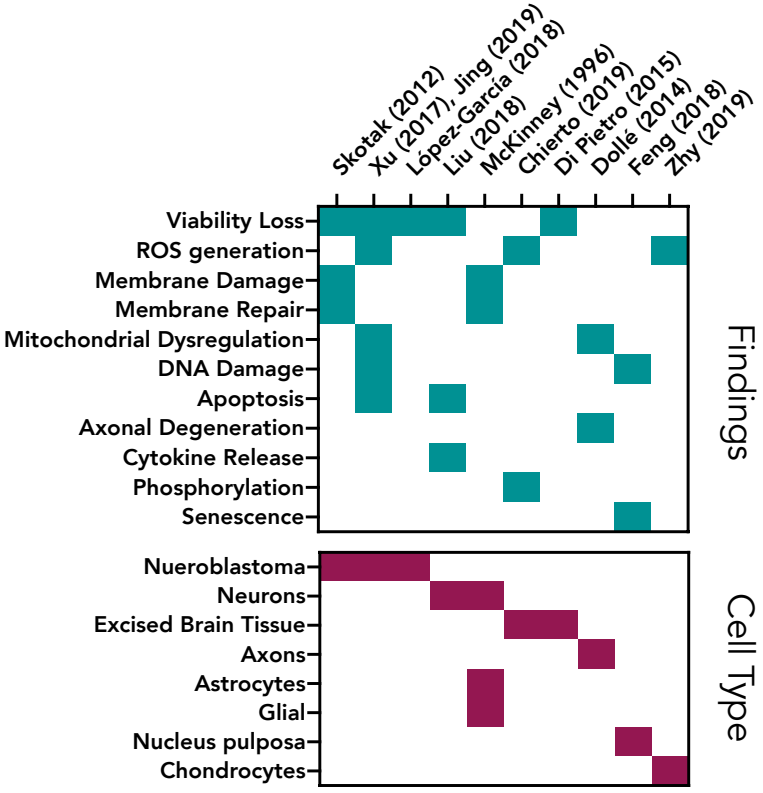

Figure 2.9: Summary of findings and cell type for selected *in vitro* substrate stretch publications[172,173,182,174–181]. A subset of *in vitro* substrate stretch publications, identified by neurologically related cell type choice, are compared across cellular assay findings and cell type of choice. While there are several publications that investigated the genetic response to substrate stretch, these were excluded from the comparison table.

2.5.3 Microfluidic platforms

Microfluidics have been a successful inclusion into the study of mechanobiology[183]. Most significantly, they drastically increase the sample rate for the given experiment, enabling more robust conclusions on a heterogenous population. While widely used to expose cells to laminar flow in order to study effects of physiological shear stress[184–187], microfluidic platforms have recently been re-opted for cell modulus characterization[36,188–192].

Microfluidic systems have also been developed to apply injury-level stress on cells[171]. With similar mechanical parameters to plate stretch, incorporating microfluidic pneumatic actuation

deforms membranes with more spatial precision, with μm[193] to mm[175] resolution. With this method, researchers have applied injury to endothelial cell monolayers[194] as well as specifically the axons of neurons extending through the microchannels[195]. Yap (2014) showed axonal restructuring occurs at tensile strain of 5% and lower [193] while Dollé (2014) demonstrated axonal degeneration occurs over the course of hours as a result of tensile strain at 10% and greater[175].

2.5.4 Blast Wave

Blast TBI (bTBI) is categorized into three classes of injury: primary, secondary, and tertiary. Primary bTBI is the result of the pressure wave, comprised of an initial overpressure followed by a negative pressure. Secondary bTBI is the result of a focal impact on head from a propelled debris and tertiary bTBI is from any sudden acceleration of the head due to the body being propelled. While there are many in vitro methods designed to mimic the shearing and straining events of secondary and tertiary bTBI[196], researchers use barotrauma[197], blast chambers [198], shock tubes[199] [200] [201], and bubble cavitation[202,203] in order to recreate the overpressure and negative pressure phases of the primary blast wave.

The blast pressure wave is both reflected from the body as well as absorbed, traveling through the brain over the course of microseconds to milliseconds[152]. The mechanical injury of primary bTBI is unique in that it results from very high strain rates ($\geq 10^4$ s^{-1}) [204] with low strain ($\leq$ 10%)[205]. Differences in tissue density influence the local propagation of the pressure wave, resulting in differences in each tissue's deformation[152].

To mitigate the heterogeneity of injury, researchers have focused on single cell types, cultured in monolayers[88] or three-dimensionally[204]. Li (2018) applied MPa of pressure by shock wave to individual epithelial cells, finding that there was maximum strain of 12%[204], supporting *in vivo* predictions for whole brain strains of $\leq$ 10% due to bTBI[205]. Kane (2012), exposed microglial

cells to *in vitro* blast injury with kPa of pressure, but found no influence of primary blast wave on microglial activation and little gene expression changes within 6 hours after injury. Human neuroblastoma cells injured by blast exposure showed viability loss over the first 24 hours as well as signs of recovery by 48 hours[199]. VandeVord (2008) did not find any viability loss or apoptotic induction for astrocytes injured with kPa of positive pressure, but there was increased gene expression for a select filament proteins within 24 hours of injury[197].

2.5.5 Limitations of in vitro mechanical injury tools

The aforementioned *in vitro* tools have immeasurably advanced the field's understanding of cell biomechanics. By reducing the material complexity to the single cell level, the relationship between mechanical input and cellular response can be more closely examined. These tools still have their drawbacks, however, especially in regards to exploring the effect of mechanical injury by applying high strain with high strain rate (Figure 2.9). While AFM and plate stretchers offer the widest range of strain magnitudes and strain duration, they are both limited in the strain rate applied to each cell. The use of microfluidics for deforming cells applies much higher strain rates, but are predominantly designed for low strain magnitudes. Similarly, only low strain magnitudes can be achieved using blast wave and bubble cavitation.

In aggregate, these in vitro tools span a wide range of possible strain rates, strain magnitudes, and strain durations. There is clearly an unexplored parameter space, however, for large strain magnitudes that last for only sub-millisecond strain durations.

.

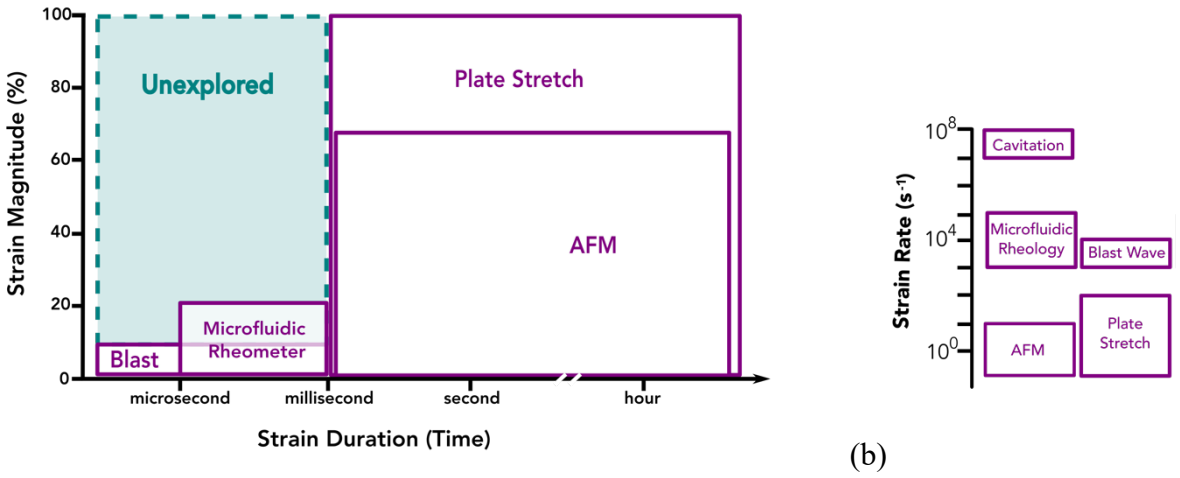

(a) (b)

Figure 2.9: Typical mechanical injury parameters achieved by several *in vitro* methods. AFM, plate stretch, microfluidics, blast wave, and cavitation are each bounded by possible mechanical inputs. (a) Researchers can choose from then entire range of applied strain magnitudes (0 – 100%) as well as strain duration as short as sub-microsecond to even longer than days, but there is an unexplored regime of large strain and sub-millisecond strain duration. (b) Each tool is also limited in its possible strain rate. The tools that achieve the highest strain rates ($> 10^3\ s^{-1}$) also are limited in the magnitude of applied strain (< 25 %).

3 A Microfluidic MEMS Device for Applying Single Cell Mechanical Injury

3.1 Introduction

As just discussed, few *in vitro* tools are capable of applying repeatable strain injury to single cells in a high throughput manner and no current tool is capable of applying extremely high strain rate. To this need, the µHammer device was created. The µHammer is a microfluidic MEMS chip designed to apply consistent mechanical strain to individual cells *in vitro*[206,207,208]. The tool was developed through a collaboration between UCSB and Owl biomedical (USA) and fabricated by Innovative Micro Technology (IMT, USA). Adapted from Owl biomedical's Tyto® Cell Sorter technology, the µHammer is capable of applying repeatable injury to hundreds of cells each second.

Millions of cells can pass through the chip within an hour due to the incorporation of both microfluidics and magnetic actuation. The high speed of the cells through the microfluidic

channels are matched by the rapid magnetic actuation and subsequent spring retraction of the μHammer impact face. Each cell that passes through the chip can thereby be caught and compressed for a specific duration of time before being released and collected for further biological investigation. As this cycle of catch/compress/release repeats for every cell that passes through the device, the mechanical injury applied by the μHammer – strain magnitude, strain duration, and strain rate – remain consistent across each cell in the population. This *in vitro* method thereby establishes a large, homogenous population of injured cells that can be studied further. In this chapter, I described the principles of the μHammer device, the process flow for device utilization, and proof of concept experiments using a human K562 leukemia cell line.

3.2 Principles of the μHammer device

3.2.1 Overview

The μHammer chips are fabricated[19] by IMT and comprise three central materials: a single crystal silicon substrate, electroplated Nickle-Iron (Ni-Fe), and bonded glass (Figure 3.1A). The straight microfluidic channel is etched as 350 μm long, 50 μm deep, and 25 μm wide into the substrate. This channel connects the input via to the output via, setting the path for every cell that enters the μHammer device and is later collected from the output chamber. The curved microfluidic channel of equivalent depth and width connects the input via to the waste via. This channel is an avenue for fluid when the μHammer is actuated and has closed off the flow path to the output via, thereby maintaining fairly continuous fluid flow for the upstream cells.

Similarly etched from a silicon substrate, the μHammer body, impact face, and spring all comprise the impact system (Figure 3.1C). The impact system is released from the surrounding silicon yet pinned to the chip by the spring, enabling its in-plane movement. Due to the

electroplated Ni-Fe layer, the μHammer body is also a component in the magnetic system. This system also includes the tapered Ni-Fe pole and an external solenoid. The pole channels the magnetic field originating from the solenoid, creating a magnetic force on the μHammer body resulting in its actuation and movement across the channel.

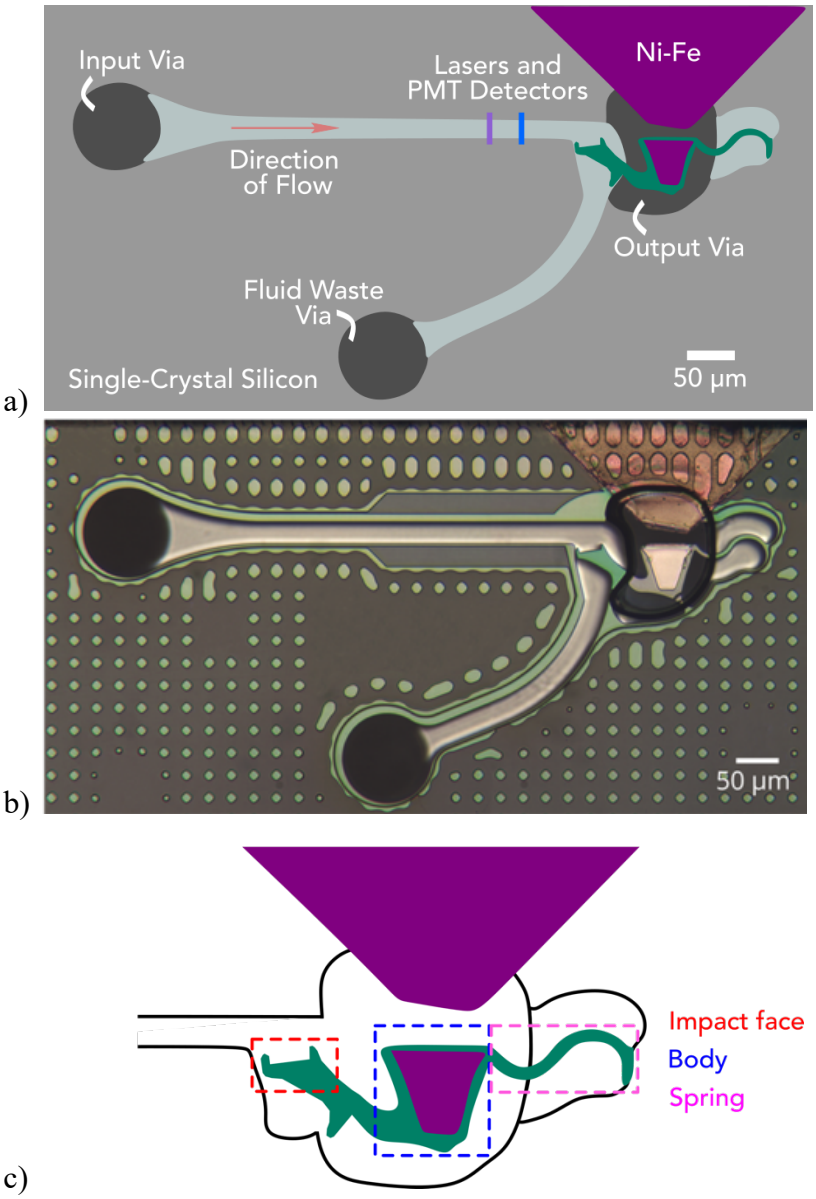

Figure 3.1 The µHammer MEMS chip (a) Labeled schematic and (b) micrograph of the µHammer chip. Fluid enters the chip through the input via and exits through the output via when µHammer impact assembly (teal) is not actuated. During actuation, excess fluid is passed through the lower channel to the waste via. The actuation is achieved magnetically, utilizing electroplated Ni-Fe (purple) on the chip. A magnetic field is created by a solenoid (not shown) that is channeled through the tapered Ni-Fe, attracting the Ni-Fe layer of the impact assembly. (c) The sub-sections of the µHammer impact assembly include the impact face (red box), the body (blue box), and the spring (pink box). During actuation the body is attracted across the open via to the larger pole. The impact face also travels across the channel until it makes contact with the opposite wall. When the magnetic field is released, the spring retracts the body and impact face to its original position.

The μHammer chip is bonded to the sterilized μHammer cartridge and together are loaded into the Tyto® cell sorting system (Fig. 3.2). The bonded glass on the top surface of the chip enables visualization of the chip face by the optical system of the MACSQuant® Tyto® (Miltenyi Biotech, Germany). The Tyto® system houses and controls several necessary components for the μHammer device operation. It applies pressure to the input chamber, driving the fluid through the chip, all the while controlling the flow speed of the cells. It also contains components for controlling the temperature (0ºC – 37ºC). A solenoid is aligned adjacent to the Ni-Fe pole of the chip, such that applied current will trigger the magnetic actuation of the impact system. Finally, two lasers are positioned such that their paths cross the microfluidic channel upstream of the μHammer impact face and output via. With each laser is a paired photomultiplier tube with a corresponding emission filter. Together, the lasers and detectors enable fluorescence-based actuation, similar to FACS (reviewed in Chapter 2.3.2).

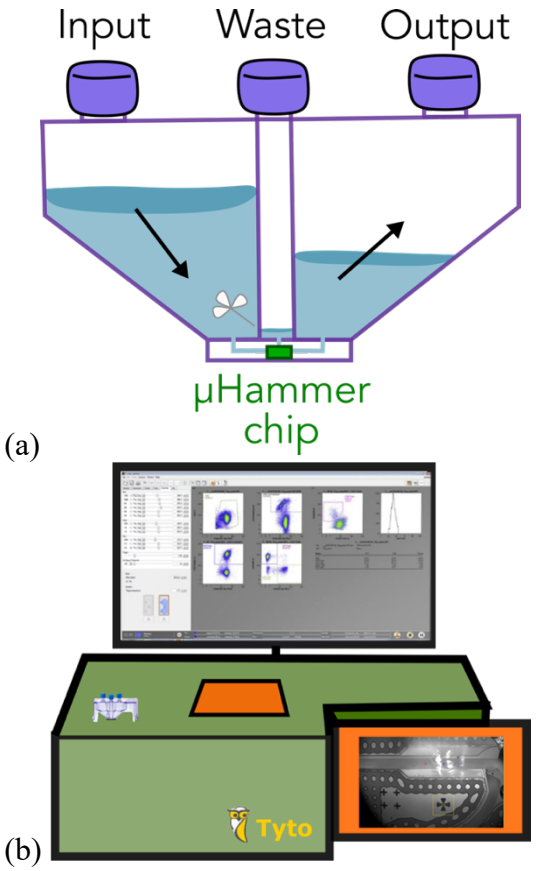

Figure 3.2 The µHammer cartridge and Tyto® Cell Sorter. (a) The µHammer chip is bonded to a cartridge that stores input and output cell solutions. The µHammer cartridge with arrows to depict direction of fluid flow. The cartridge is loaded into the (b)Tyto® system which applies pressure and houses the optical system. Once loaded, the fluid in the input chamber of the cartridge is pressure driven into the µHammer chip, through the microfluidic channel, then out into the output chamber. The solution in the input chamber is gently mixed to maintain consistent cell density. The GUI of the Tyto enables tailoring the actuation settings, temperature, flow rate, and optical detection of the cells.

3.2.2 Compressive Injury Parameters

3.2.2.1 Mechanical Strain Magnitude and Strain Duration

The primary objectives of the µHammer device are to apply mechanical strain to a single cell and apply consistent strain to a large population. The µHammer applies 1D compressive strain to spherical cell (Figure 3.3) resulting in equal tensile extension along other dimensions. Prior to actuation, the face of the µHammer is approximately 20 µm from the opposite channel wall. As the hammer closes on a cell, the distance between the impact face and the far wall decreases. When

the distance is reduced past the original diameter of the cell, there is a mechanical strain applied on the cell (Equation 3.1). The velocity of the impact face (~2.6 m/s) determines the strain rate applied on the cell (Equation 3.2).

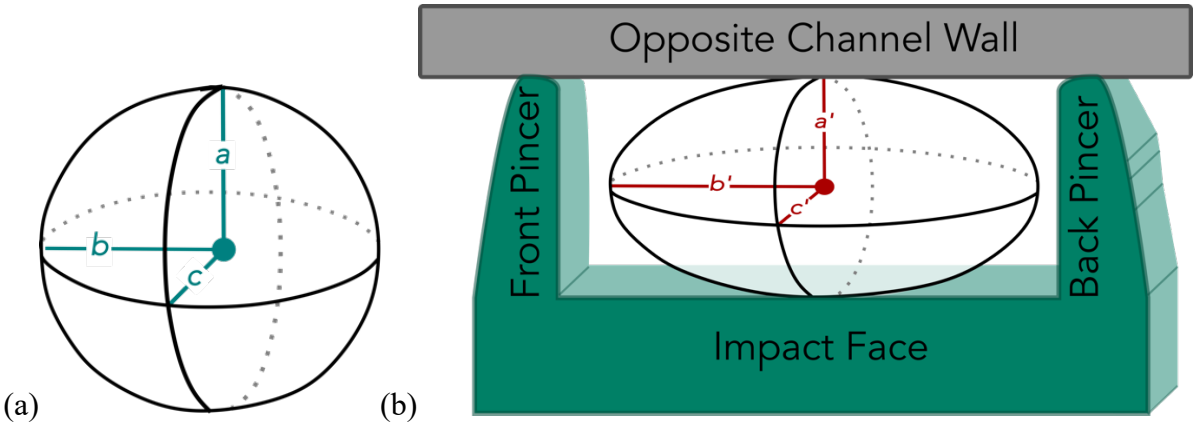

Figure 3.3 One-dimensional strain is applied on a suspended, spherical cell when captured between the μHammer impact face and the opposite channel wall. (a) Cells in solution can be approximated as spheres, with consistent radius. (b) A cell captured by the μHammer impact face is subjected to uniaxial compressive strain. The magnitude of the applied strain is dependent on the original diameter of the cell and the pincer length of the μHammer

Equation 3.1 $$\epsilon = \frac{l_0 - l}{l_0}$$

Equation 3.2 $$\dot{\epsilon} = \frac{v}{l_0}$$

When a cell is caught between the two pincers that flank the impact face, it is fixed between the top glass, the bottom of the channel, and the channel wall. The impact face is 28-μm across and the depth between the top glass and the channel bottom is 50-μm. Therefore, the compressive strain is applied in the dimension of the μHammer impact face and the opposite wall. The magnitude of the compressive strain is dictated by the length of the pincers as these set the final gap size into which the cell is deformed.

For the work described in this dissertation, two µHammer devices designs have been fabricated. These two devices differ solely pincer length, thereby determining the final compression gap size. The resulting strain magnitudes are shown in Table 3.1 for the maximum cell diameter of 20-µm (discussed in section 3.3.1) and the two cell types studied in this dissertation.

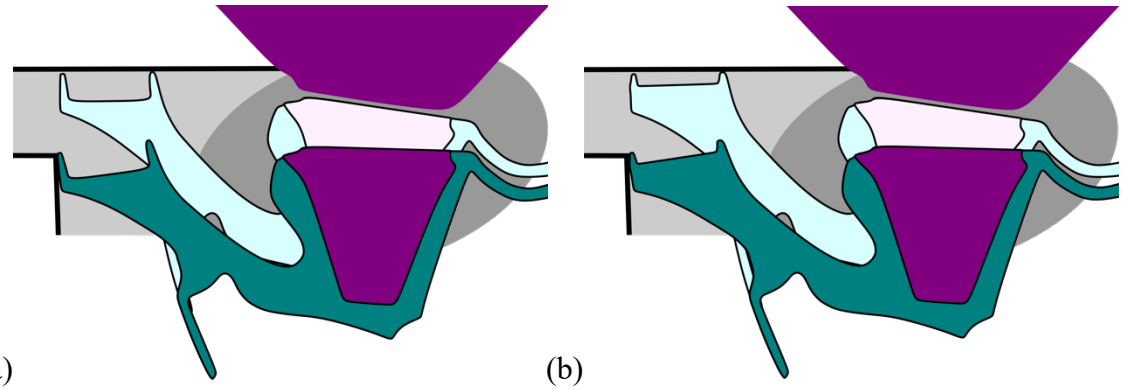

(a) (b)

Figure 3.4 Schematics of two fabricated µHammer chips differing in pincer length. Schematic of the µHammer impact face and body prior to actuation (dark) as well as its positioning at maximum compression (light). The device depicted is fabricated with pincers that are (A) 7.5 µm long and (B) 4.0 µm long. The two devices

Table 3.1 The two µHammers fabricated with either 7.5µm or 4.0 µm pincer lengths results in different compressive strain magnitudes for K562 and Neural Progenitor cells (NPCs) and similar strain rate magnitudes.

		Pincer length		Velocity
		7.5 µm	4.0 µm	2.6 m/s
Cell	Diameter (µm)	Strain Magnitude (%)		Strain Rate (s^{-1})
Maximum	20	63	80	130 x10^3
K562	14	46	71	186 x10^3
NPC	13	42	69	200 x10^3

As discussed in chapter 2, the duration of the compression is also an important parameter for describing injury. While the maximum strain magnitude the µHammer device can apply is 80%, as limited by the maximum allowable cell size in the microchannel, the current maximum

duration the cell can be compressed is 1 millisecond. Comparing these two injury conditions to typical *in vivo* (CCI, FPI, WDI) and *in vitro* (plate stretch, microfluidic rheometer, blast wave) parameters, it is apparent that the μHammer injury spectrum has filled in a previously unexplored region (Figure 3.5). To our knowledge, no prior tool has been shown as capable of applying this range of strain magnitudes for sub-millisecond durations, especially achieving the extremely strain rates with high throughput.

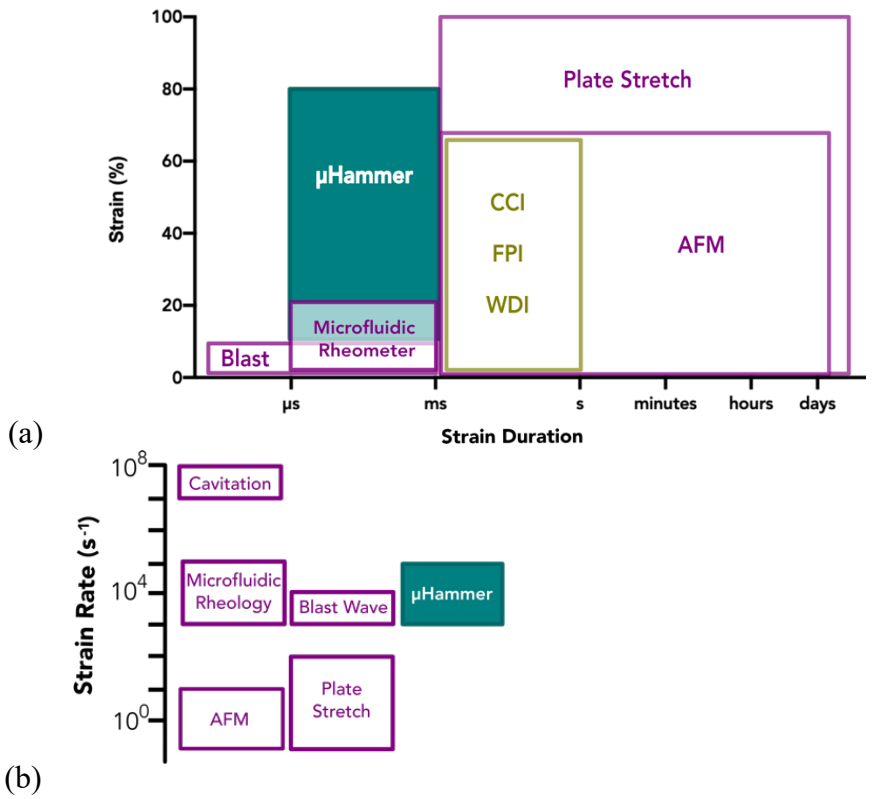

Figure 3.5 The μHammer applies strain magnitude and strain duration parameters previously unachievable by common mechanical injury methods as well as strain rates on the upper end of the spectrum. Comparing the μHammer injury parameters to other typical *in vivo* (gold) and *in vitro* (purple) techniques that apply mechanical strain to cells, the μHammer achieves a previously inaccessible parameter space. (a) The μHammer is capable of strain magnitude up to 80% with strain durations ranging from the microsecond to millisecond. Two techniques with similarly brief strain durations (Blast chamber and microfluidic rheometry) have not reported strain magnitudes greater than 20%. Two techniques commonly used to apply large strains magnitudes (CCI and plate stretch) are incapable of applying strain for fewer than several milliseconds. (b) Aside from the novel use of bubble cavitation, μHammer applies orders of magnitude higher strain rate to single cells than previous tools.

3.2.2.2 Compressive Force and Pressure

As discussed in Chapter 2, the measured modulus of a cell is dependent on the rate at which strain is applied. Nevertheless, the compressive force can still be approximated using a simple Hertz contact model[209] (Equation 3.3) and the reported moduli of both the K562 cell line[210] as well as the human NPC line[211]. For the Hertz contact model, R = radius of the cell, E = Young's modulus,

v = poison's ratio (assumed to be 0.5), and δ is the pincer length. By assumed the volume of a cell remains constant during the deformation, the pressure applied can then be determined (Equation 3.4), where V = volume of the cell. As provided in Table 3.2, the compressive force applied to each cell, either by the 7.5 µm pincer length or 4.0 µm pincer length µHammer, is on the order of nano-Newtons to sub-micro-Newtons and the pressure applied is on the order of kilo-Pascals.

Equation 3.3 $$F = \frac{4\sqrt{R}E(2R-\delta)^{\frac{3}{2}}}{3(1-v^2)}$$

Equation 3.4 $$P = \frac{3FV}{2\delta}$$

Table 3.2 The approximated Force and Pressure applied to K562 cells and NPCs during mechanical compression by the two µHammer devices

Cell	Modulus (kPa)	Force (nN)		Pressure (kPa)	
	Pincer length	*7.5 µm*	*4.0 µm*	*7.5 µm*	*4.0 µm*
K562	0.40	40	71	0.11	0.11
NPC	5.04	295	617	1.28	1.43

3.2.3 High Throughput, Optical Detection

The optical detection of each cell relies on flow cytometry and FACS principles. The cell suspension is driven with low pressure (60 kPa) through the microfluidic channel of the chip. The pressure is adjusted to maintain a cell velocity of 2.5 m/s. Each cell passes between two lasers

fixed upstream of the µHammer impact face (Figure 3.6). A cell is first detected as it crosses the first laser (405 nm) and its emitted fluorescence or scattered photons are collected by the paired photomultiplier tube (PMT) detector. When the cell is detected again 50 µm downstream by the second laser (488 nm) /detector pair, the velocity of the cell is determined and used to time the subsequent magnetic actuation.

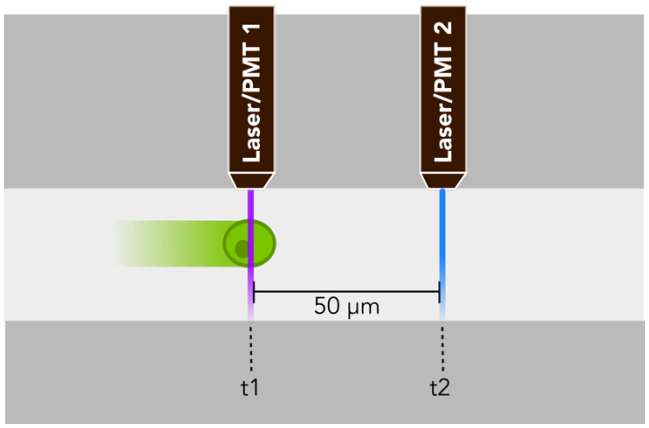

Figure 3.6 Depiction of a cell crossing the two lasers upstream of the µHammer impact face. When a cell crosses the path of the first laser (405 nm), its emitted fluorescence (or backscatter) is collected by the laser's paired photomultiplier tube detector. The second laser (488 nm) is 50 µm downstream of the first and similarly detects the same cell as it crosses the laser path. The typical cell will transit this distance in 20 µs, a speed that is maintained by the Tyto® software with adjustments to the applied pressure. In addition to feeding back to the pressure controller, the specific cell speed also dictates the timing of actuation for the µHammer. This cell-specificity enables high throughput cell capture and injury.

For the µHammer experiments, the applied pressure to the cartridge is used to control the velocity of the cells to maintain a transit time of 20 µs between the two lasers. This speed correlates with the µHammer actuating around 600 times each second to catch each cell.

In addition to feeding back to the pressure controller and triggering the downstream actuation, the Tyto software also characterizes each it based on its photonic scatter and/or fluorescent emission (Figure 3.7). Utilizing flow cytometry principles (Chapter 1), the cells are first gated on by their side scatter to particle noise. This removes the signal from debris, thereby increasing the

software sensitivity for individual cells. Removing debris signal also prevents unnecessary µHammer actuation, thereby increasing overall throughput.

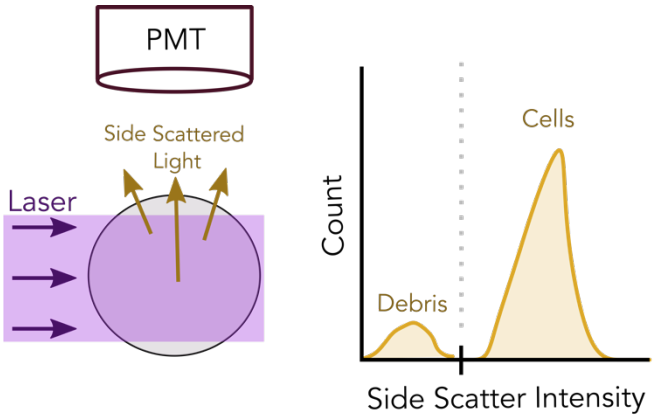

Figure 3.7 Debris particles in the solution are excluded from Tyto® signal detection via side scatter intensity gate. As a cell travels across the laser path, the side scattered light is collected by a PMT detector. The intensity of the collected side scatter light corresponds to the cell's granularity, or density. As a first pass of filtering to improve the signal to noise ratio, the Tyto® Cell Sorter is set to gate on particles with side scatter intensity above a threshold.

In early iterations of µHammer experimentation, these cells were further characterized by their fluorescent emission, establishing the final actuated population. Similar to detecting scatter intensity, the PMT detectors were dedicated to collect the emitted photons from the laser-specific fluorophore excitation. The utilization of fluorescence required staining the starting population of cells with fluorophores that could be excited by the first laser at 405 nm and the second laser at 488 nm. The emissions would pass through a 450 nm +/- 50 nm or a 525 nm +/- 50 nm bandpass filters, respectively, and collected by the PMT detectors. The voltage supplied to the PMTs were established such that the desired signal intensity was amplified and noise was reduced. All experiments, therefore, required consistent and uniform stained cell populations such that each cell would accurately trigger an actuation. Without this, the final injured population would be impure due to the collection of false negatives.

To remove the possibility of a non-uniformly detectable population, the current iteration of the µHammer experimentation does not use fluorescent signal, but instead backscatter (Figure 3.8). This adaptation was first required when the experimental design transitioned from an environmental temperature of 4ºC to 37ºC. At 4ºC, the live cells successfully retained their fluorescent proteins, resulting in a population with consistent emission over the course of the hours-long experiment. At physiological temperature, however, the fluorescence would degrade in under 30 minutes – severely reducing the intensity of the emission and contaminating the output population with uninjured cells.

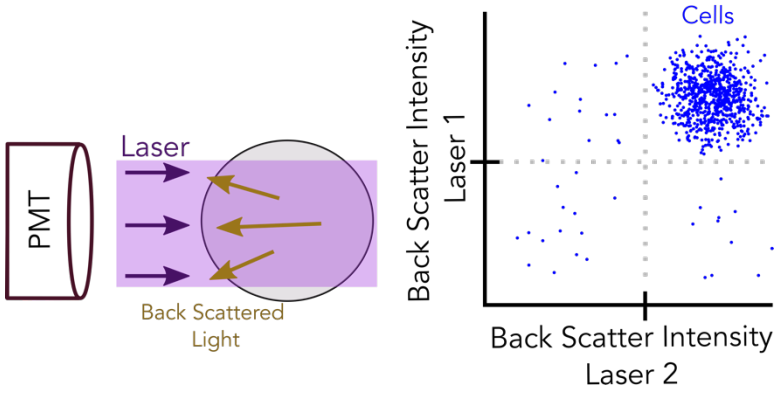

Figure 3.8 The Tyto® Cell Sorter detects cells using dual-back scatter intensity. As a cell travels across the laser path, the backscattered light is collected by a PMT detector. Due to the larger size of a cell compared to cellular debris, the intensity distribution of the backscattered light will be much greater, and fall within a characteristic boundary. A second laser/detector will also characterize the passing cell. Together, the bi-plot of the two backscatter intensities identify the population of cells from cellular debris. The Tyto® Cell Sorter actuates on every cell that with intensity that falls within the upper right quadrant of the bi-plot.

Prioritizing the experimental benefits of physiological temperature, the cells were no longer fluorescently labeled. Instead, as they crossed each laser, their resultant backscatter was detected by the PMTs and used for triggering each actuation. In addition to maintaining consistent cell signal over time and reducing pre-µHammer cell processing, the output cell population was now completely unlabeled. This was an drastic experimental benefit as it left options to use the complete suite of fluorescent wavelengths in follow up biological assays.

3.2.3 Magnetic Actuation and Spring Retraction

Once a cell is detected and its velocity is measured, the Tyto® software predicts the time the cell will reach the end of the channel. To catch a cell within the center of the impact face, the µHammer is actuated typically 16-17 µs prior to the cell reaching the end of the channel. The actuation begins when 5 mA current is supplied to the solenoid that is housed in the Tyto Cell Sorter, external to the µHammer cartridge and chip. The resulting 1.6 T magnetic field is then channeled through the Ni-Fe pole of the µHammer chip, applying an attractive magnetic force (Equation 3.5) on the Ni-Fe on the µHammer body. This draws the released µHammer body across the channel towards the larger, fixed pole.

Equation 3.5 $$\boldsymbol{F} = \Delta(\boldsymbol{m} \cdot \boldsymbol{B})$$

The current is maintained long enough for the µHammer face to travel across the channel and hold contact with the opposite channel wall. When the current is released, the magnetic field dissipates and the S-curved spring retracts the µHammer body to its initial non-actuated position. By continuing to apply current, the cell is held by the µHammer for a user-set duration. The current range is 10 µs - 1 millisecond, boundaries set by the Tyto® Cell Sorter software.

When the current is released and the magnetic field dissipates, the spring retracts the impact system to its resting position within 20 µs. The spring (stiffness, $\kappa \simeq 224\ \mathrm{N/m}$) is the only connection point between the impact assembly and the chip. The spring is responsible for restoring the µHammer body and impact face to their non-actuated position in the channel.

3.3 Process Flow For Device Utilization

The process flow for µHammer device use adapted over time, but this section will describe the most current methods for preparing cells, organizing experiments, and aspects of post-µHammer

device cell processing. Additional details for each specific experiment will be described in subsequent sections.

3.3.1 Preparing the cells for the µHammer device

Whether working with a cell line that is cultured in suspension or adherent, the first steps of preparing cells for the µHammer device focus on washing and filtering (Figure 3.7). Cells should be removed from their culture apparatus, pelleted, and washed with PBS. After a second centrifugation, up to 300,000 cells / mL can be resuspended in Tyto® Running Buffer (TRB, Owl biomedical, USA). The TRB has been designed by Owl biomedical specifically for the high speed microfluidics of the Tyto® such that cells are not prone to adhering and bubbles are minimized. The cell solution must then be filtered to remove all particles larger than 20 µm strain. This step prevents potential clogging in the 25 µm wide channel.

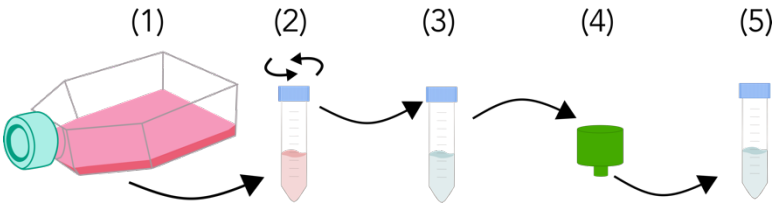

Figure 3.7 Diagram of simplified cell processing steps prior to µHammer use. (1) Cells are first removed from a culture flask, maintained under vendor recommended conditions. (2) The cell solution is pelleted at 300 – 500 g, centrifugation speed set such that the cells separate out of the media supernatant while remaining viable. (3) the pellet is loosened and reconstituted in Tyto® Running Buffer. (4) The cell solution is passed through a sieve to exclude all particles greater than 20-µm in diameter. (5) the final cell solution must then be analyzed for cell density and viability prior to transferring to the input chamber of the µHammer cartridge.

3.3.2 Conducting an experiment with the µHammer

For a typical µHammer experiment, there are at least three conditions compared: baseline/control, sham control, and compressed (Figure 3.8). The baseline/control group consists

of all cells that have been processed up to the starting solution phase but not be transferred to the μHammer input chamber. This population is instead pelleted and resuspended in appropriate cell culture media for the duration of the device use.

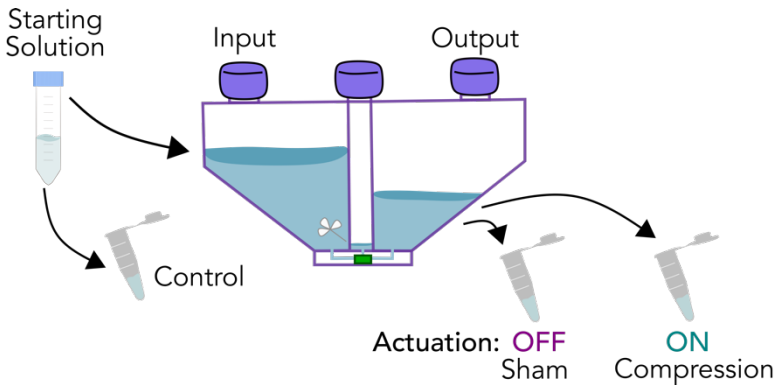

Figure 3.8 Three typical conditions compared within a μHammer experiment. Every μHammer experiment includes at least a baseline/control group, a sham group, and a compressed group. The cells for each population are from the same starting cell source, resuspended in Tyto® Running Buffer, and passed through a 20-μm sieve. The control condition is never introduced into the μHammer cartridge or chip. The input cell solution is then transferred into the input chamber of the cartridge and pressure driven through the μHammer chip where they are collected in the output chamber. To achieve the sham condition, there is no actuation of the μHammer and the cells are subjected to shear stresses alone. For a compression condition, the μHammer will actuate on each cell detected by the Tyto® software.

The second control group is the sham group. These cells are similarly processed up to the starting solution phase but are also transferred to the input chamber of the cartridge along with the future injured cell group. Both the sham and the injured cell groups are held in the input chamber and warmed to 30ºC. A small mixer driven at 800 rpm in the input chamber maintains equal distribution of the cells in the solution. The sham condition is pressure driven through the device into the output chamber. During this process, there is no actuation of the μHammer so that the sham group is only subjected to the shear stress of the microfluidic system ($\tau \sim 1500$ dyn/cm^2, Equation 3.6). The optical system is still engaged, however, so that the number of cells passing to

the output chamber can be tracked and the final population accrued can be estimated. The sham groups is collected from the output chamber, pelleted, and resuspended in media for the duration of the device use.

Equation 3.6 $$\tau = \frac{6\eta Q}{h^2 w}$$

As previously discussed, by utilizing two separate devices (4.0μm gap size and 7.5 μm gap size) and adjusting compression duration, many injury conditions are possible with the μHammer device. For each desired injury condition, their treatment is similar to the sham condition. The cells are driven through the microfluidics and tracked optically to maintain a consistent cell velocity and quantify the accrued population. Unlike the sham condition, the cells are also actuated on and compressed for a designated duration. Once released, they exit through the output via to the output chamber. Before each new experimental group can be impacted, the previous must first be removed from the output chamber.

3.3.3 Post-μHammer cell processing

Once the cells are retrieved from the output chamber of the μHammer, there are virtually no limitations on biological investigations. Typical post-μHammer cell processing can depend on the assay of interest and investigative timescale (Figure 3.9).

In order to isolate the effects of mechanical impact on the cellular response, a researcher could choose to analyze a specific function of the cells immediately upon removal from the cartridge or after a specified (delayed) length of time. For immediate investigations, the cells can remain either in the Tyto® Running Buffer or pelleted and resuspended in an assay-specific buffer. For a delayed investigation, it is necessary to pellet the cell population and reconstitute it in their specific culture media for continued incubation.

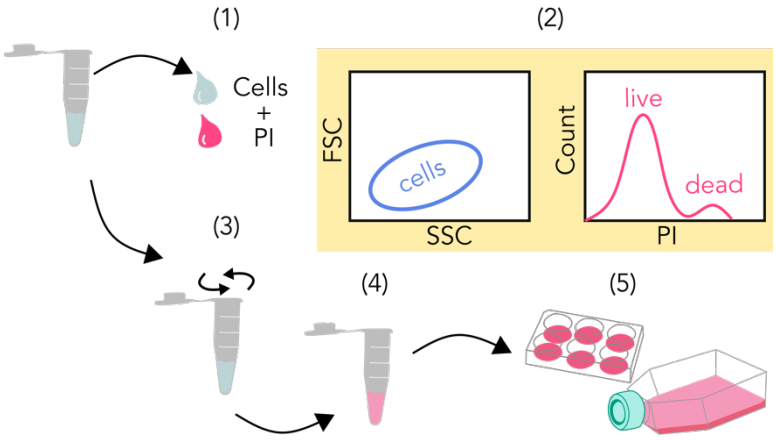

Figure 3.9 Typical processing of cells upon removal from the µHammer cartridge. For immediate investigation of cell viability, (1) an aliquot is taken from the µHammer output cell solution and combined with Propidium Iodide (PI). (2) The cell solution is analyzed by flow cytometry. Cell concentration is determined by SSC and FSC, by the percent of particles with expected size and density. This population is gated on for the parallel flow cytometry analysis of cell viability. The quantity of cells detected with PI fluorescence (488 nm laser, 645 – 730 nm filter, MACSQuant® Analyzer 10) determines the dead cell population size for the source cell solution. (3) The cell solution is pelleted at 300 g, (4) reconstituted in cell culture media, (5) and plated for continued culture enabling delayed biological investigations.

3.4 Proof of concept with K562 Leukemia Cells

3.4.1 Introduction

The human erythroleukemic K562 cell line is commonly used for flow cytometry research and was chosen for the early phases of µHammer process development. As previously described, the initial µHammer processing relied on fluorescent detection of the cells and the K562 cell line is reliably labeled with carboxyfluorescein diacetate succinimidyl ester (CFSE), with no known biological side effects. While CFSE is maximally excited at 492 nm and detected at 517 nm, it has a much broader excitation and emission spectrum. Therefore, this single fluorophore is excited by both the 405 nm and 488 nm lasers in the Tyto®, making it an ideal single fluorescent label for µHammer experiments. K562s are also a cell line that is cultured in suspension, thereby simplifying the transition from culture to device as well as sampling from the populations for various biological assays post-injury.

Limitations to using this cell line was the lack of prior knowledge of how K562 cells line respond to compressive injury. Unable to accurately predict a likely time regime of their strongest response, the proof-of-concept investigations instead attempted to capture a range. The widest time range was explored for changes in cell proliferation. As shown by previous mechanical injury studies, an injury response is capable of manifesting by altering the proliferation rate of the cells – positively[129,212–217] or negatively[172,218,219]. Tracking the number of cells over a nine-day period would identify the time at which the injured cells surpassed the control or lagged behind, possibly narrowing the time range of injury response.

The second proof-of-concept investigation focused specifically on known viability markers for early and late apoptosis. Assessed within the first few hours of compression, this assay was chosen due the prominence of the apoptotic cascade in the in TBI pathology

3.4.2 Results and Discussion

3.4.2.1 Compressed Cells Have Extended Lag Phase, Unaffected Doubling Rate

For the proof-of-concept studies with K562 cells, the mechanical injury impact was limited to only one injury condition – 46% strain magnitude for 10 μs duration. The compressed condition was compared to a sham injury condition, K562 cells passed through the μHammer device at the same velocity, as well as a control condition. The cells were resuspended in media and cultured up to 10 days, Over the course of culture, the number of cells in each group was counted such that the retained proliferation could be examined post-injury.

Despite seeding the three conditions at the same density, the compressed condition was found to have a drastically reduced number of cells over the culture time period compared to the controls (Figure 3.10A). Shear forces alone, demonstrated by the sham condition, were not found to as strongly influence cell growth. Notably, however, there was variability in the number of K562

cells across the experimental replicates – exemplified by the control condition – while retaining low variability across the sample replicates within each experiment.

Logarithmically transforming the average number of cells enabled identification of the quiescent and exponential phases for each condition. The exponential phase was determined by a linear regression with an $R^2 \geq 0.94$ and the quiescent phase was considered as all culture time prior to induction of exponential phase. The control condition had an average quiescent period lasting 28 hours $\pm$ 6 hours whereas the compressed condition did not reach exponential phase on average for 86 hours $\pm$ 25 hours (Figure 3.10B), Interestingly, once exponential phase was reached, there was no significant difference between the doubling rates across the three conditions (Figure 3.10C).

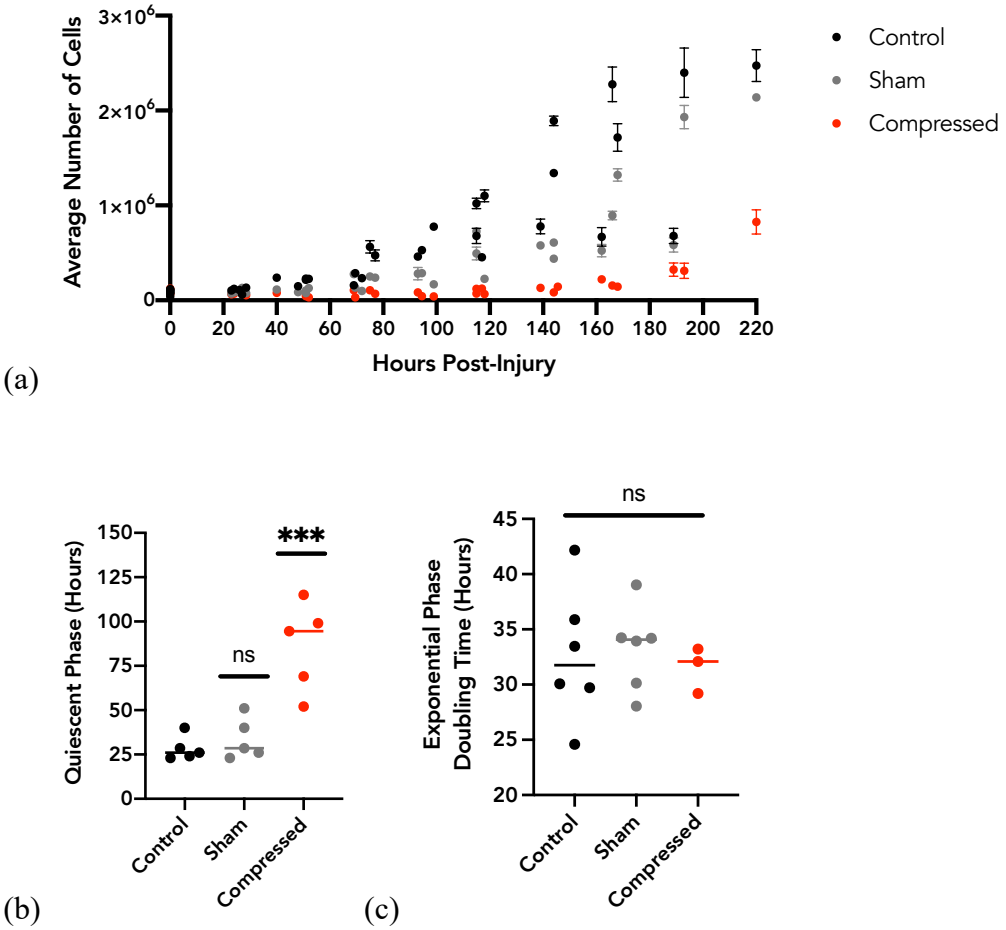

Figure 3.10 K562 cell proliferation time course post-injury. After µHammer injury, K562 cell populations were cultured up to 10 days. Over the course of culture, each cell population was quantified on average every 28 hours ± 10.5 hours. (a) Plot of experimental replicates (k = 6 replicates for control and sham, 5 replicates for compressed), showing the mean number of cells for each condition, error bars reflect the standard deviation across n = 3 wells. The 50% - 10 µs injury condition shows extremely reduced cell numbers over time compared to both the sham and control. (b) The culture time lapsed prior to each group entering exponential phase of cell growth. Point represents the culture time for each k experimental replicate, line represents the mean doubling times. Compressed cells had significantly longer quiescent phases compared to the control and sham conditions (c) The rate of cell doubling determined for k experimental replicates, represented by a point with a line depicting the mean. Control and sham groups reached exponential phase in all 6 replicates whereas the injured condition only reached exponential phase in 3. No significant difference was determined between the three conditions. Statistics performed by One-Way ANOVA, post-hoc Dunnett's compared sham and compressed conditions to the control, ns = $p > 0.05$, *** = $p < 0.001$.

3.4.2.2 Compressed Cells Retained Viability

One potential cause of an extended lag phase for the compressed K562 condition would be viability loss. To examine both necrosis and apoptosis, two viability markers were utilized: Sytox and Annexin V, respectively. One of the first distinguishing events of apoptosis (programmed death), is the translocation of the membrane-bound phospholipid, phosphatidylserine (PS), from the inner to outer leaflet of the plasma membrane. This exposed PS can be monitored by the binding of fluorescently conjugated Annexin V protein. K562 cells were measured for Annexin V-FITC binding (Annexin V^+) as well as membrane permeability ($Sytox^+$). Early apoptosis is indicated by Annexin V exposure, without membrane permeability whereas both indicate late apoptosis. Membrane permeability alone indicates necrosis.

The K562 cells were compressed with a strain magnitude of 46% for 10 μs strain duration and resuspended in culture media. Over the course of 3 hours after compressive injury, the viability of the injured condition was periodically assessed. Overall, there was an increasing trend for each viability-loss category, and by 2.5 hours post-injury the compressed cells surpassed the average control population size for each. The total population sizes, however, never surpassed 5% on average. The aggregated populations across the 3-hours were also compared to the control populations, demonstrating that there was no statistical difference between any of the viability-loss markers (Figure 3.11B).

(a)

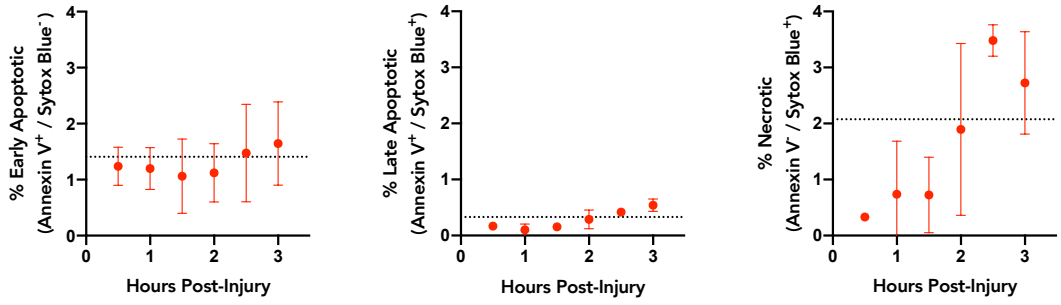

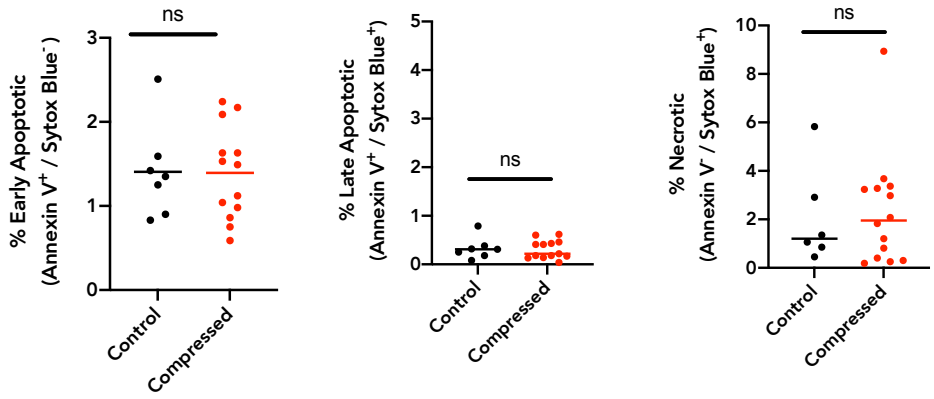

(b

Figure 3.11 K562 Viability up to 3-Hours Post-Injury. After 46% - 10 µs mechanical compression, K562 cells were cultured alongside a control population for 3 hours with k = 2 two experimental replicates. Dual staining the cells with Annexin V and Sytox Blue enabled quantification of the populations in one of 3 viability categories: early apoptosis (Annexin V^+/ $Sytox^-$), late apoptosis (Annexin V^+/ $Sytox^+$), or necrosis (Annexin V^-/ $Sytox^+$). (a) For the compressed cells, the average percent of the total population in each viability category is plotted over the 3 hour period, with error bars depicting standard deviation across the two experimental replicates. The dashed line demonstrates the control population's average percentage for each category. (b) The accumulated 3-hour population data, represented on a 1-dimensional axis, each point represents a single sample and the line depicts the mean. No significant difference was determined between the compressed populations and the control across the three viability categories. Statistics performed by unpaired t-test, post-hoc, ns = $p > 0.05$.

3.4.3 Conclusion

These results demonstrated that a the µHammer was capable of applying compressive injury to single cells where the injury itself is shown to be more complicated than induced cell death. As shown by the viability assays, the cells remained > 90% viable throughout the first few hours post-injury even after experiencing 46% compressive strain. While the strain was applied for only 10 µs, there was still a dramatic effect on the cell proliferation several days after injury, as demonstrated by the extended quiescent phase. Interestingly, the injured K562 cells still entered exponential phase and seemingly had recovered from the damage – suggested by the matched proliferation rate to the control conditions. These findings suggest that the K562 cell injury response take place throughout several days after compression

For an in vitro mechanical injury tool to be precise, it must subject each cell to the same loading conditions. For the tool to be useful, however, it must apply injury that induces a cellular response beyond necrosis. The K562 proof of concept investigations, therefore, provided a useful benchmark for future cellular response to impact.

3.4.4 Materials and Methods

3.4.4.1 K562 cell culture

The human leukemia K562 cell line (ATCC, USA) was cultured in RPMI-1640 media (Fisher Scientific, USA) supplemented with 10% FBS, 25 mM HEPES, and 0.01% penicillin streptomycin (Lonza Biologics, UK) at 37ºC and 5% CO2. Cells were seeded at 100,000 cells/mL and passaged when cell density reached 1,000,000 cells/mL, measured using the MACSQuant Flow Cytometer (Miltenyi Biotech, Germany).

3.4.4.2 CFSE cell staining

Human K562 cells (ATCC, USA) were fluorescently labeled with CellTrace CFSE (Thermo Fisher Scientific, USA). CFSE was incorporated at 0.1% v/v at 37ºC for 15 minutes then washed and resuspended in Tyto Running Buffer (Miltenyi, Germany) at a concentration of 300,000 cells / mL.

3.4.4.3 Proliferation assay

Following retrieval from the device, cells were pelleted at 300g for 5 minutes and re-suspended in culture medium at 100,000 cells/mL. The cell density of each population was measured over the course up to 10 days by assessing the cell density of an aliquot post-mixing.

The exponential phase for each condition within each experimental replicate was determined by an R^2 fit > 0.94 of a linear regression to the log-transformed average cell numbers over time. The doubling time during the exponential phase was deduced by Equation 3.7 and Equation 3.8.

The time duration prior to the data fitting the criteria for exponential phase was categorized as quiescent phase.

Equation 3.7 $$N = N_0 e^{rt}$$

Equation 3.8 $$\mathrm{t_d} = \frac{\log(2)}{\mathrm{r}}$$

3.4.4.4 Apoptosis Assay

Following retrieval from the device, cells were pelleted at 300g for 5 minutes and re-suspended in culture medium at 100,000 cells/mL. At each time point (0.5 – 3.5 hours), cells were washed in Annexin V buffer and stained with Annexin-V APC (5% v/v) and Sytox Blue (0.1% v/v) for 15 minutes at room temperature. Cells were then washed and analyzed by flow cytometry.

3.4.4.5 Statistics

Statistical comparisons between compressed, sham, and the control groups were performed using One-way ANOVA and post-hoc Dunnett's test, $\alpha = 0.05$. Differences between the compressed group and the control group were performed using t-test, $\alpha = 0.05$. All statistics were performed using GraphPad Prism v 8.0.

4 The uncoupled effects of compression magnitude and duration on the acute health of neural progenitor cells

4.1 Introduction

As previously discussed in Chapter 2, the brain comprises several different cell types, but the most commonly investigated in the context of Traumatic Brain Injury (TBI) are neurons, astrocytes, and stem cells. While each has a unique response to mechanical trauma that would be valuable to evaluate further using the μHammer, neural progenitor cells (NPCs) were chosen for the investigations in this work. This decision was due to the role of NPCs in neuro-regeneration, as

they could identify valuable signaling pathways for damage and repair[125,220–222]. The ReNcell VM human cell line (Millipore, USA) was specifically chosen because of its similarity to neural stem cells in that they have the propensity to differentiate into both neural and glial cells but has also been immortalized as well as applied as a neuronal model[211,223–226].

The electromagnetically actuated MEMS μHammer was then used to evaluate the effects of varied mechanical impact on human neural progenitor cells. In order to compare to the proof-of-concept cell type, K562s (ATCC, USA), the effect of injury on acute health was investigated first. These cells differ slightly in size, the typical NPC ($d \cong 13\ \mu m \pm 1\ \mu m$) is slightly smaller compared to the K562 ($d \cong 14\ \mu m \pm 2\ \mu m$). Therefore, when compressed by the 7.5 μm pincer μHammer the typical NPC experienced a 42% strain compared to the 46% strain for a K562 cell.

A more significant distinction between these two cells types is their culture conditions. K562 cells are cultured in suspension while the NPCs are an adherent cell line cell. Due to the differences between these two cell lines, there was little expectation for identical cell response. The magnitude of compressive injury applied by the μHammer is dependent on the initial cell size, as this sets the applied strain.

In this work we demonstrate that the μHammer can be used for applying mechanical injury to human NPCs and decouple the effects of strain magnitude and duration on acute health (Table 4.1). Two strain magnitudes (ε = 42% and 69%) and two strain durations (10 μs and 100 μs) were applied on NPCs at unprecedented high strain rates ($\dot{\varepsilon} \sim 200 \times 10^3\ s^{-1}$) and high throughput (up to 36,000 cells/min).

Table 4.1 Injury parameters compared to decouple the acute health effects of strain duration and strain magnitude on human NPCs

Parameter	Control	Flow/ Sham	Compressed			
Strain Magnitude, ε (%)	0	0	42	42	69	69
Strain Duration, t (μs)	0	0	10	100	10	100

The magnitude of applied strain was found to be significantly correlated to NPCs membrane permeability shortly after compression as well as reduced cell number over a 70-hour period. Meanwhile, the duration of strain was shown to be significantly correlated to the induction of early apoptosis within the first 24 hours after compression. Despite these effects on cell health, there was no significant difference in the doubling times of the NPCs.

4.2 Results and Discussion

4.2.1 Shear stress does not negatively affect NPC viability over the course of a typical μHammer experiment

As a naturally adherent cell, subjecting the NPCs to suspension conditions could potentially induce its own set of negative cell responses, let alone the shear stresses ($\tau \sim 1500$ dyn/cm^2) a cell experiences flowing through the μHammer microfluidic channels or the mixing (800 rpm) of the cell solution in the input chamber. To first evaluate these unavoidable experimental side effects, the NPCs were monitored for change in population viability. The viability of the NPCs exposed to the mixing alone as well as the shear forces were compared to the viability of the initial pre-μHammer exposed control NPCs (Figure 4.1). It was important to monitor the viability over the course of a few hours as this would exceed the typical maximum μHammer experiment.

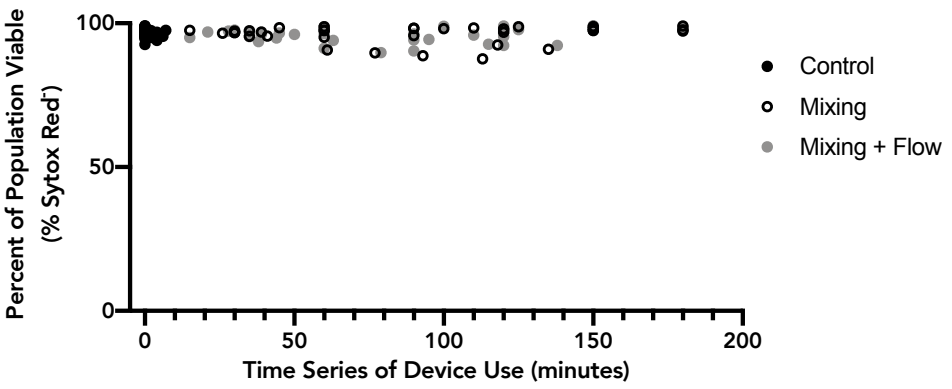

(a)

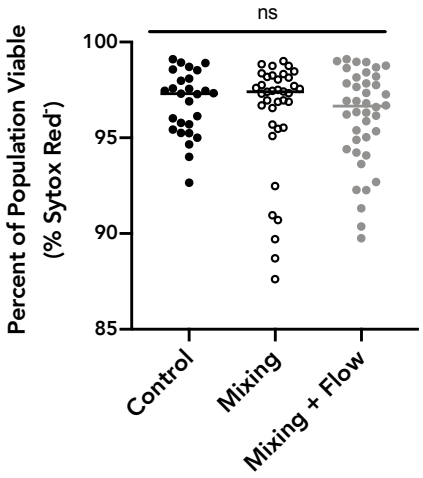

(b)

Figure 4.1 No significant viability loss occurred in NPCs due to shear forces from the propellor mixer or flow through the microfluidics during the course of experiments. (a) Viability was assessed by the % Sytox Red population in the mixed and mixed + flow (sham) populations over a 180 minute-long continuous µHammer experiment. Each point represents the average viability of an aliquot removed from either the input chamber (mixed), output chamber (mixed + flow), or the initial pre-µHammer-transferred control populations. The data represents time series across 8 separate µHammer experiments. (b) The time series is re-plotted in 1D and no significant difference in cell viability was determined between the three control conditions by One-Way ANOVA, post-hoc Tukey's HSD, ns = $p > 0.05$.

4.2.2 Compressive strain induced immediate NPC death in a magnitude-dependent manner

Impermeable to live cells, PI is only able to cross a damaged or degraded plasma membrane. Therefore, in conjunction with its natural fluorescence upon binding ribonucleases, PI is a commonly used molecule to identify damaged or necrotic (dead) cells. PI was also an ideal membrane permeability marker as the assay does not require an incubation time. An extended

incubation time could lead to further cell degradation such that the damaged cells would instead be identified as debris by flow cytometry analysis. Because the flow cytometry analysis for this investigation characterized populations of NPCs, it was crucial that mechanically injured cells (even if necrotic) remained intact in order to first be gated based on side and forward scatter. The total time from the first cell in the population being injured to the collection ($50{,}000^{+}$ cells) analyzed for PI^{+} was typically 5 minutes.

It was found that all four mechanical injuries incurred by the μHammer resulted in an significant increase in membrane permeability for NPCs within this short time frame. Each strained condition had increased population of the percentage of PI positive cells (% PI^{+}) compared to the control group (Figure 4.2A). The sham condition was also compared to rule out effects of flow-induced shear stress, and no statistical difference to the control was determined.

The specific influence of strain magnitude compared to strain duration was also assessed. The magnitude of applied strain had a significant increased effect on the % PI^{+} population, thereby demonstrating increased damage occurred as a result of the higher strain magnitude. By contrast, there was no significant difference between the % PI^{+} cells for longer strain durations (Figure 4.2B).

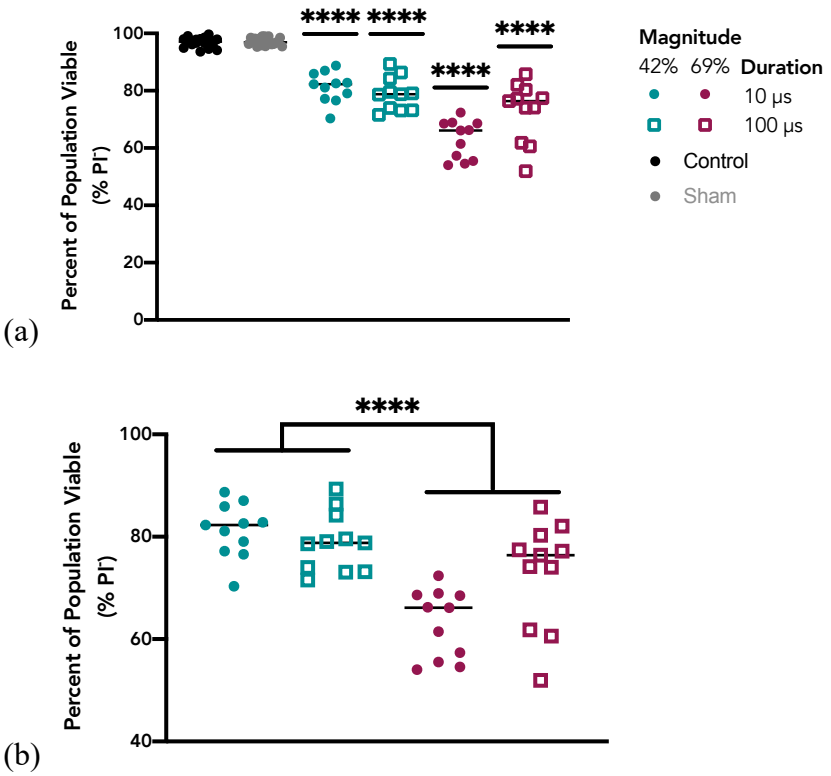

Figure 4.2 Compressive strain induced magnitude-dependent necrosis within minutes in NPCs. Propidium iodide (PI) was used to asses membrane damage and necrosis in NPCs within 5 minutes of injury. The percent of PI negative (PI^-) identified cells are shown with statistical comparison of each group to the control condition. Each point represents a sampled population of at least 5×10^4 cells. The black line depicts the mean across 3 experimental replicates for each group. (a) Statistical significance was performed as a One-Way ANOVA, post-hoc Dunette's compared each condition to the control. (b) Comparing within compressed groups the percent of PI negative (PI^-) identified cells determined the sensitivity of response was to strain magnitude, not duration. Statistical significance was performed as a Two-Way ANOVA. **** = $p < 0.001$.

Plasma membrane degradation is a typical precursor to necrosis, although prior studies have shown conflicting trends regarding effects of mechanical damage. Previous studies report sustained loss of cell viability after stretch injury[227,29]. On the other hand, membrane repair of neuronal cells has been shown to occur within 10 minutes of stretch injury[228] and impermeable dye uptake has been found to decrease over a 24-hour period after injury[181]. These low throughput studies have the benefit of imaging cells during the injury period and monitoring the same cells over time. While the µHammer enables high throughput manipulation, high quality fluorescent

imaging of the cells during compression is currently impossible. Further, the use of flow cytometry is the perfect analysis tool for quantitative characterization of large cell populations, it has its own drawbacks in that cell-specificity is lost.

To monitor whether the population of necrotic or membrane permeable cells would continue to increase over time, the injured and sham NPCs were transitioned to media and cultured in suspension for an additional hour. Over this time, aliquots of each population was assessed for percent PI^+ every 10 minutes (Figure 4.3A). This processing step also included a gentle centrifugation step to transition the cells from the buffer to culture media and there was a noticeable loss in the PI^+ population as a result. Therefore, this processing step led to the unintended removal of the necrotic cell population for all injury conditions. Over the course of the remaining hour, post-centrifugation, the three of the four injured populations were still significant more necrotic than the sham condition (Figure 4.3B).

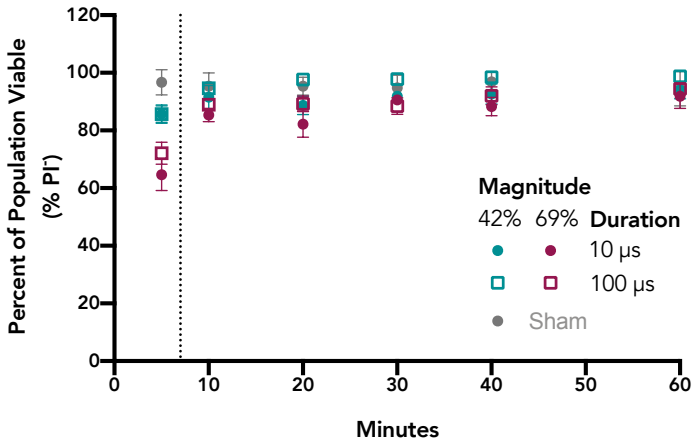

(a)

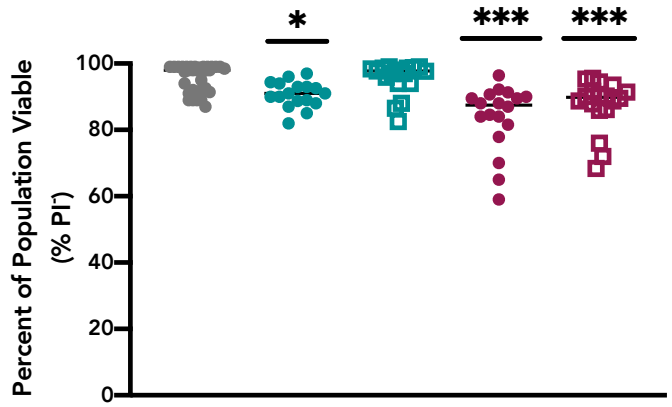

(b)

Figure 4.3 Membrane damage and necrosis was detectable in NPCs throughout first hour after injury. NPCs were collected from the µHammer, assessed for immediate viability by PI, then pelleted and resuspended in culture media. (a) Over the course of 60 minutes, the necrotic population of cells were assessed every 10 minutes. The dashed line depicts the time at which the cells were centrifuged and resuspended. Each point depicts an average of 3 experimental replicates, error bars represent the standard deviation. (b) The viability of the same cell populations over the 60 minutes are shown on a single 1D axis. In aggregate, the 42% 10 µs condition and both 69% strain magnitudes have a significantly greater PI+ population compared to the sham condition. Statistics are determined by One-Way ANOVA, post-hoc Dunette's compared each compression condition to the sham, * = $p<0.05$, *** = $p<0.01$.

Combined, these results show that cell membrane permeability significantly increased immediately after compression (within 5 minutes) and higher applied strains corresponded to a larger number of injured cells, assessed by higher % PI^+. Because membrane damage was measured within five minutes after compression, this observation suggests that primary cellular

injury, rather than a biomolecular cascade related to secondary injury, was responsible for membrane damage. These results are consistent with previous *in vitro* cell stretch studies that showed strain magnitude governs cellular uptake of impermeable dyes[29,181,227,228].

4.2.3 Compressed Cells Retain Adhesion Ability

Due to the importance of the mechanical microenvironment on cell adhesion[229] and migration[230], the maintained ability of the NPCs to adhere after μHammer compression was also investigated. Examining a single strain duration, 10 μs, and a single strain magnitude, 69%, the compressed condition was seeded alongside the control and sham NPCs, at equal seeding densities. At two time points, 1 and 4 hours, the number of cells adhered in each condition were quantified, with no statistical difference (Figure 4.4).

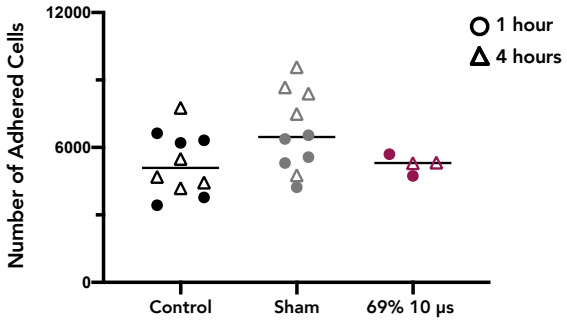

Figure 4.4 Compressed cells retain functional adherence. Control, sham-injured, and 69%-10 μs compressed NPCs were seeded at 20,000 cells/cm^2 and allowed to settle and adhere to pre-laminated wells. At 1 and 4 hours post-seed, the wells were washed and the remaining adhered cells were counted. No statistical difference was detected between the three groups. Statistics performed by One-Way ANOVA, post-hoc Dunette's compared sham and compressed conditions to the control.

4.2.4 Strain Duration Initiates Early Apoptosis

One of the first distinguishing events of apoptosis (programmed death), is the translocation of the membrane-bound phospholipid, phosphatidylserine (PS), from the inner to outer leaflet of the plasma membrane. This exposed PS can be monitored by the binding of fluorescently conjugated

Annexin V protein. Here, cells were identified as positive for Annexin V-FITC binding (Annexin V^+), but with intact plasma membranes (PI^-), a state representative of early apoptosis.

Although all compressed groups showed an increase in early-phase apoptosis after 4 hours of culture compared to 1 hour of culture, only 42% - 1ms was significantly increased (Figure 4.5A,B). After 24 hours of culture, all compression conditions showed significantly increased early apoptosis relative to the control (Figure 4.5C). Interestingly, strain duration had a significant effect on early apoptosis, while strain magnitude had no effect (Figure 4.5D). There was no significant difference between the sham and the control populations, indicating that flow-induced shear stress alone did not induce apoptosis.

As cells continue to progress through additional stages of apoptosis, the plasma membrane eventually breaks down. The stage of late apoptosis was identified as a cell positive for both Annexin V and PI. There was no significant difference in late apoptosis (Annexin V^+/PI^+) across all time points. There was also no significant difference in necrosis (Annexin V^-/PI^+), though this could be attributed to dead cells lost from the sample populations during the low-speed centrifugation step.

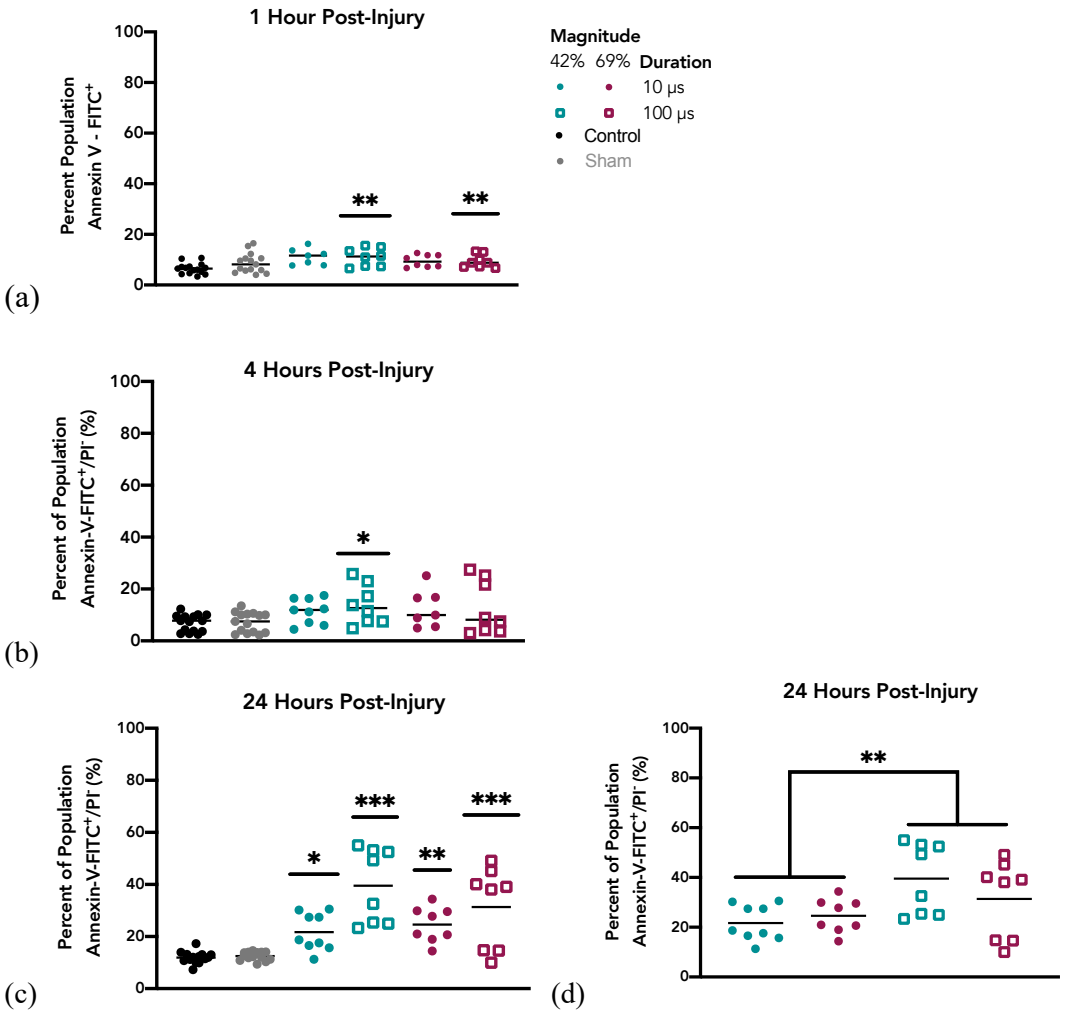

Figure 4.5: The longer duration compression increased the early apoptotic population size 24 hours after injury. (a) The percentage of cells detected as Annexin V^+/PI^- (early apoptotic) up to 24 hours after seeding, with statistical comparisons of each group to the control. Each point represents a sampled population from an individual well. The colored line depicts mean across three experimental replicates for each group. (b) 1 hour (c) 4 hours and (d) 24 hours after injury. Comparing within compressed groups at 24 hours to show the sensitivity of response to strain duration but not magnitude. N.S. = no significant difference, * = $p<0.1$, ** = $p<0.05$, *** = $p < 0.01$.

At 24 hours after injury, all compression conditions demonstrated a significant increase in early apoptosis in NPCs compared to the control group cells. This increase in apoptotic markers was significantly correlated to strain duration. For the 42% strain magnitude, increasing strain duration

from 10 μs to 100 μs resulted in a 1.8-fold increase in mean early apoptosis. For ε = 69% there was a 1.3-fold increase with increased strain duration. To our knowledge, no prior cell compression study has reported scaled cellular response to a difference in injury duration on the order of microseconds.

The apoptotic pathway varies for different cell types and stimuli [231]; therefore three timepoints were chosen over 24 hours to increase the chance of capturing the induction of apoptosis. While previous stretch injury on neuronal cells showed significantly increased early apoptosis by four hours[179], cells compressed with the μHammer were not significantly early apoptotic until the 24-hour timepoint. While late apoptosis was not detected within the first 24 hours after injury, future investigations will monitor apoptosis at later time points to determine whether injured cells recover from early apoptosis or progress into late apoptosis, and correlate these to strain magnitude or duration.

4.2.5 Strain duration reduces cell growth but injury had no effect on proliferation rate

The process of cell division is a known mechanical process[232], with several *in vitro* studies demonstrating continuous mechanical compression significantly reduces cell proliferation[233–237]. This induced quiescence was also observed in the K562 pilot study (Chapter 3), when the compressed cells remained quiescent for almost 3 times as long as the control cells. As discussed in Chapter 2, however, several *in vivo* studies have monitored the post-TBI transition of NPCs from quiescent to proliferative[128,129] supporting neurogenesis[122–126] and contradicting these *in vitro* findings.

To understand how compressive strain would affect this NPC cell line in terms of retained proliferative ability, the NPCs were subjected to a range of injury conditions, cultured for four days, and cell growth was quantified at least twice daily. Over 70 hours of culture, the sham

population most closely matched the control population in cell number (Figure 4.6A). Despite seeding at similar densities, the four injury conditions resulted in fewer cells than the control and sham at each time investigated. Each experiment had unique growth curves, even within the control condition, therefore to reduce this experimental variability, the cell number, N, for each treatment group is normalized to its respective experimental control, $N_{control}$ (Figure 4.6B). Through this analysis, there were two compressed groups with $N/N_{control}$ ratios significantly lower than the sham for two conditions. These were 42%-100 μs, 69%-100 μs. Comparing within compressed groups, there was a significant correlation between the strain duration and reduced $N/N_{control}$ but not between strain magnitude (Figure 4.6C).

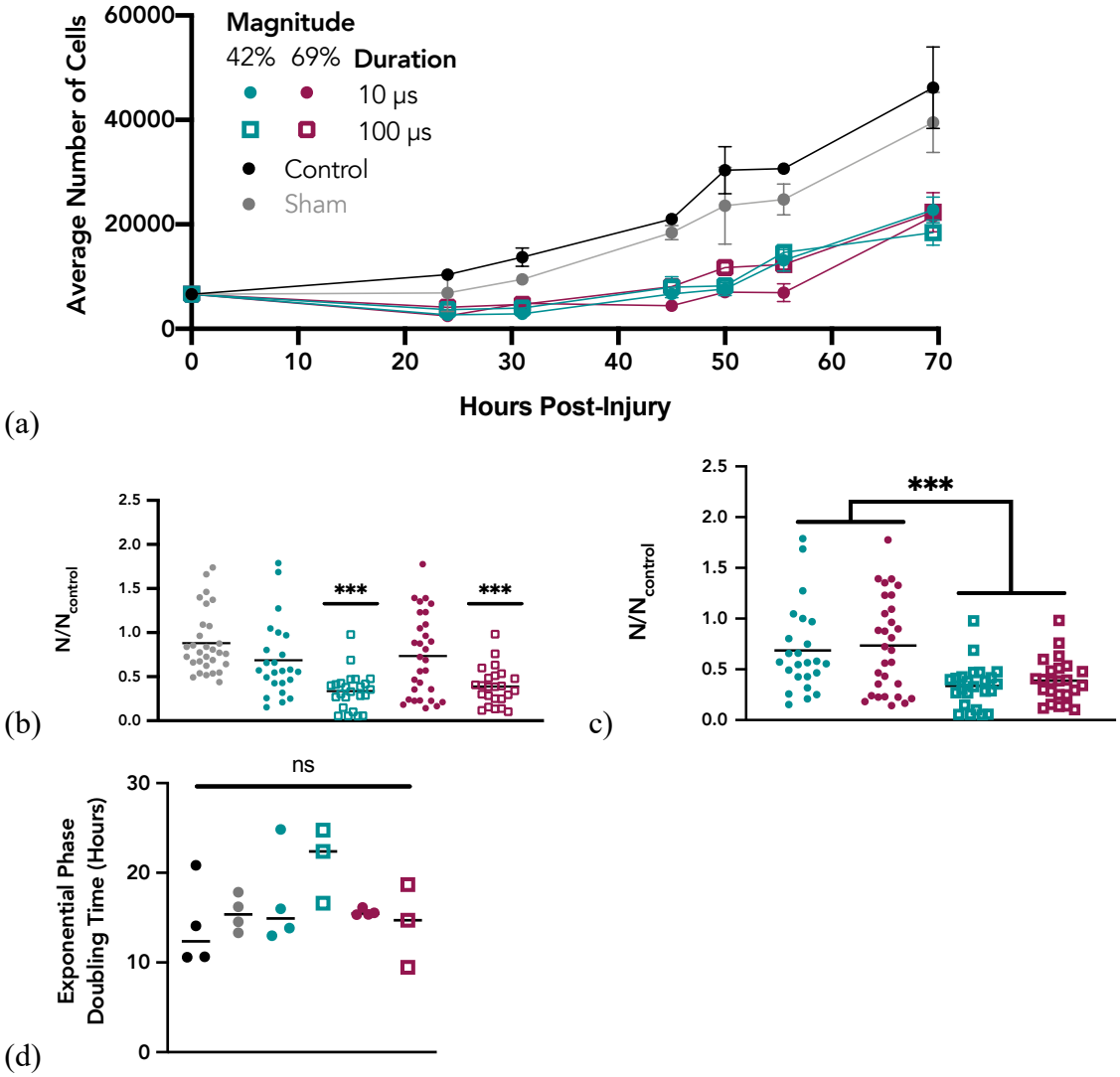

Figure 4.6: Effect of compression on NPC proliferation. (a) Plot of representative data from 1 experimental replicate, showing mean number of cells over a 70-hour period, error bars reflect standard deviation across n = 3 wells. Inset depicts the doubling times calculated from n ≥ 3 experiments, with no significant differences. Lines used to guide the eye. (b) Ratio of mean cell number for each treatment condition to control, with each point representing ratio for single time point, colored line depicts mean of N ≥ 24 time points, across n ≥ 3 experimental replicates. Cells compressed for 100 µs have significantly lower normalized cell numbers compared to cells subjected to the sham condition. (c) Comparing within compressed groups, significantly lower normalized cell growth is correlated to strain duration. (d) N.S. = no significant difference, *** = $p < 0.01$.

Upon examination of the exponential phases alone, no significant difference was found in doubling times between any compression group and the control. Across the four experiments, the

control group doubling times range from 15 hours to 25 hours. This experimental variability could potentially obscure significant inter-group differences in proliferation rate.

While there was a correlation between the applied μHammer strain duration and reduced NPC number over time, the doubling times of compressed cells were not found to be significantly different when compared to the control. The unaffected proliferation rate despite fewer cells in the population suggests that the mitotic capability of the non-necrotic cells was maintained after injury.

It is possible that the reduced cell number is due to necrosis that occurred after seeding, rather than impaired mitosis. While necrosis was investigated in the separate viability assays, necrotic cell populations were undetected in the early apoptosis assay, potentially due to removal of dead cells from the measured population during the additional processing step of the low-speed centrifugal wash – a step excluded from the proliferation assay.

4.3 Conclusions

Understanding the relationship between mechanical strain and cellular response of NPCs will ultimately lead to improved diagnostics and treatment of high strain rate mechanical injury conditions such as Traumatic Brain Injury. The μHammer MEMS device was used to investigate the effects of mechanical strain on human NPCs by applying strains of magnitude $\varepsilon = 42\%$ or $\varepsilon = 69\%$ for static periods of 10 μs or 100 μs. The high throughput, single-cell nature of the μHammer MEMS device enabled measurement of the robust population statistics necessary for thorough investigation of cellular response to compressive injury. Applying consistent injury impact parameters allowed for detection of changes in NPC membrane permeability, early apoptosis, and proliferation. Strain magnitude was significantly correlated to increased membrane permeability within five minutes of cell compression, while strain duration was significantly correlated to longer timescale effects: early apoptosis at 24 hours after compression and cell number over four days of

culture. Future work will continue to explore the transient mechanisms of cellular injury to improve our understanding of cellular damage and recovery.

4.4 Methods

4.4.1 NPC culture

The immortalized human Neural Progenitor Cell line, ReNcell VM (Millipore, USA) was cultured in ReNcell NSC Maintenance Media (Millipore, USA) supplemented with 20 ng/mL basic Fibroblast Growth Factor (bFGF, Millipore, USA) and 20 ng/mL Epidermal Growth Factor (EGF, Millipore, USA). Flasks were pre-treated with 20 µg/mL laminin (Millipore, USA) in DMEM/F12 without HEPES, with L-Glutamine (Corning, USA). Cells were seeded at 20,000 cm^2 on pre-treated tissue culture plates and incubated at 37ºC with 5% CO_2. For continued culture, cells were passaged every 2-3 days.

4.4.2 NPC preparation and µHammer device use

The NPCs are prepared first by enzymatic lifting by Accutase at 37ºC for 3 minutes. After the reaction is quenched with warm ReNcell Maintenance Media (Millipore, USA), the cells are pelleted at 300 g for 5 minutes and resuspended in Tyto Running Buffer™ (Miltenyi, Germany), filtered to remove particles greater than 20 µm diameter, and loaded into the sterile µHammer cartridge. Once the cartridge is housed within the MACSQuant® Tyto® Cell Sorter (Miltenyi, Germany) where it is maintained at 37ºC, low pressure (< 1kPa) is applied and cells pass from the loading chamber through the µHammer chip to the collection chamber of the cartridge. Within the chip, the cell solution fluid flows at an approximate rate of 8 mL per hour. The compressed cells experienced either a moderate strain of 42.2% ± 7.4% or a high strain of 69.2 ± 12.1% for durations of 10 µs or 100 µs. In all compression conditions, cells experienced similar applied strain rates of $\dot{\varepsilon} \sim 200\times10^3\ s^{-1} \pm 36\times10^3\ s^{-1}$.

4.4.3 NPC viability assay using Sytox Red

Both the input cell population and the sham control population were evaluated on viability by Sytox™ Red Dead Cell Stain (Thermo Fisher Scientific, USA). Over the course of the experiment, the propeller-mixer in the input chamber of the cartridge was magnetically rotated at 800 rpm. The Input cell population was retrieved from the input chamber in 200 μL aliquots at various time points throughout the experiment. The Sham cell population was similarly retrieved from the output chamber. After retrieval, cells were pelleted at 300g for 5 minutes and re-suspended in PBS with Sytox™ Red (0.1% v/v) for 15 minutes at room temperature. Cells were then washed and analyzed by flow cytometry.

4.4.4 NPC viability assay using Propidium Iodide

To investigate the immediate loss of membrane integrity due to mechanical injury, the membrane impermeable fluorescent marker Propidium Iodide (PI, Sigma-Aldrich, USA) (5% v/v) was added to each group upon retrieval from the output chamber. Flow cytometry was used to detect fluorescence due to PI intake by cells in each sampled population (populations ≥ 50,000 cells/sample), where higher PI fluorescence would indicate increased plasma membrane damage. To assess membrane damage immediately after cell impact, treatment groups were investigated within five minutes of removal from the output chamber. For each condition, three population replicates were analyzed per experiment, with the experiment repeated in triplicate

4.4.5 Early Apoptosis assay

To investigate early apoptosis, cells from all groups were seeded in 48-well plates and cultured for 1 hour, 4 hours, or 24 hours. At each assessment time point, cells were enzymatically lifted by a brief incubation in diluted 1:10 Accumax (eBioscience, USA); after 3 minutes, the reaction was quenched by addition of media. Cells were centrifuged at 300g and washed with Annexin V Buffer

(Invitrogen, USA). Cells were stained with Annexin V-FITC (Miltenyi Biotech, Germany) (10% v/v) in Annexin V Buffer for 15 minutes at 21ºC. The stained cells were diluted 1:5 with Annexin V Buffer and PI was added (5% v/v). Flow cytometry was used to detect fluorescence signals of both Annexin V-FITC and PI in each population. For each experiment, $n \geq 2$ wells for each time point and group were analyzed, with the experiment repeated in triplicate.

4.4.6 Proliferation Assay

To track the growth of cells after impact, all groups were seeded in 96-well plates at 6,600 viable (PI^-) cells/well and cultured for 4 days. At least twice daily, the cell number was quantified to track proliferation. For each time point, cells from 3 wells per condition were enzymatically lifted (1:10 Accumax, digestion for 3 minutes at 37ºC, followed by media quench). Cell density was measured using flow cytometry by quantifying the average cell number harvested from each well. Up to four experimental replicates were conducted.

Equation 4.1 was used to normalize the quantified cell populations. For each time point, *i*, the ratio of the mean cell number, *N*, for each treatment group, *j*, to the mean cell number of the corresponding experiment control, $N_{j'}$, was calculated as follows.

Equation 4.1 $$N/N_{\text{Control}} = N_{j,i}/N_{j',i}$$

Equation 4.2 and Equation 4.3 were used to compare the proliferation rate of each condition. The doubling time, t_{double}, of each condition, *j*, was estimated by the exponential growth rate, r_j, determined using a linear regression of the natural log transformed exponential phase. The exponential phases typically initiate at $t_1 \simeq 24$ hours and end at $t_{\text{final}} \simeq 75$ hours after seeding this cell line.

Equation 4.2 $$t_{\text{double,j}} = \ln(2)/r_{\text{j}}$$

Equation 4.3 $\ln(N_{j,t}) = \ln(N_{j,t_1}) + r_j t$

4.4.7 Statistics

Statistical comparisons between compressed, sham, and the control groups were performed using One-way ANOVA and post-hoc Dunnett's test, $\alpha = 0.05$. Differences within compressed groups were also statistically evaluated to decouple the effect of strain magnitude and strain duration, performed using Two-way ANOVA, $\alpha = 0.05$. All statistics were performed using GraphPad Prism v 8.0.

5 Transcriptome analysis of mechanical strain

5.1 Introduction

As described in chapter 2, several injury models have been developed to mimic the primary injury of TBI. These models enable researchers to focus their investigations on the downstream cellular and molecular changes as a result of injury. Spanning both *in vivo* and *in vitro* systems, these models have illuminated several neurodegenerative as well as neuroprotective events that occur post-injury. Understanding these events will guide the development of therapeutics for injuries like TBI.

Primary TBI affects a complex community of tissues and cells in the brain – vascular, neural, and immune. The molecular cascade within each injured cell is similar, as it is multifaceted, complicated, and not well characterized. Far from the simple, defined 'lock-and-key' model of ligand-receptor binding, the effects of mechanical strain on a single cell is less specific, not independent of other signaling pathways[53].

Desiring an exhaustive investigation of possible changes in molecular signaling, the human Clariom S probe-based assay (Thermo Fisher, USA) was chosen for analyzing the transcriptome of neural progenitor cells (NPCs). The probe-based array used in this work provided relative

expression of 21,488 specific genes and the fold change in expression between each injury condition and the baseline condition were determined. The resulting comprehensive transcriptome profile was then used to identify several molecular signaling pathways affected by the strain injury applied by the μHammer.

Guided by the acute cellular response of strain on neural progenitor cells (NPCs), 24 hours after injury was chosen as appropriate time point for capturing molecular signaling. To fully explore the range of injury parameters attainable by the μHammer device, the strain duration of 1 millisecond was compared to 10 μs and the strain magnitude of 42% was compared to 69%. Table 5.1 outlines the experimental conditions compared.

Table 5.1 Experimental conditions compared for transcriptome analysis

Parameter	Baseline	Sham	Compressed			
Strain Magnitude, ε (%)	0	0	42	42	69	69
Strain Duration, t (μs)	0	0	10	1000	10	1000
Number of samples	5	6	3	3	3	3

In this work, we demonstrate that there is a subtle, yet global transcriptome response in the NPCs 24 hours after compressive injury. The extent of this global response is explored by random gene selection, by determining the probability that a minimum number of genes will achieve expected injury condition clustering. This sample clustering is compared against publicly available gene expression data sets, indicating that global gene profile from the μHammer is somewhat atypical. The differentially expressed genes resulting from the μHammer were also compared to several publicly available data sets, specifically those from TBI and mechanical injury studies.

These findings demonstrate there is commonality between the gene expression resulting from the μHammer and prior mechanical injury studies, as well as the relatively low commonality across any mechanical injury study.

Finally, bioinformatics were used to correlate the μHammer gene expression to canonical biological pathways and Gene Ontology gene sets. Combined, there was predicted affected regulation for interferon signaling and neuroinflammation signaling. Three transcription factors: TP53, SMARCA4, and LPS as well as two bio processes: extracellular matrix organization and RNA processing were also predicted to have affected regulation.

5.2 Results and Discussion

5.2.1 Global gene expression change is detected 24 hours after mechanical strain injury

Principle component analysis (PCA) is a commonly used, unbiased tool to visualize whole-genome similarities between samples[238 239] and will capture the fundamental essence of a large data set within a few principle components. The maximum variance across the 23 cell samples is captured in PC-1, then the residual variance is captured in PC-2, and so on for PC-3. The primary source of variance captures 16.6% of the total variance with clear separation between both 42% strain magnitude conditions and the 69% 1 ms condition from the baseline control (Figure 1A). The 42% strain magnitude conditions are separate by duration when viewed along PC-2. By PC-3, the 69% 10 μs condition is separated completely from the baseline condition as well as from the 69% 1ms condition (Figure 1B). The sham condition is not discernible from the baseline condition across the first three PC's, indicating low genetic variance as a result of shear forces and sample handling alone. The first three principle components make up 31% of the total variability in the data and further biological relevance can be discerned up to the fifth component with cumulative variability of 47.7% (Figure 5.1C).

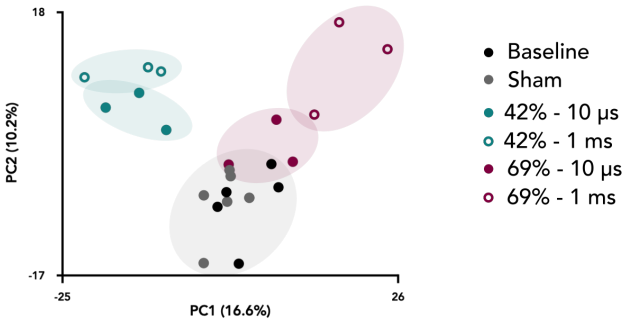

(a)

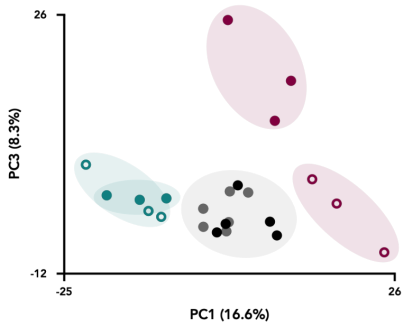

(b)

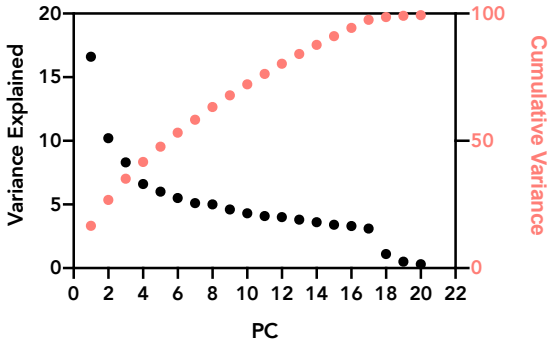

(c)

Figure 5.1 Separation between injured cells and controls and condition-based clustering demonstrated by Principle Component Analysis. (a) Principle component analysis showing separation between injured cells and the two control groups: sham and baseline 24 hours after compression. The injury condition 69% 10µs is not as easily separated along PCA-1 or -2 but is along (b) PCA-3. (c) Over 35% of total variance is accumulated within the first 3 PCA dimensions and almost 50% is accumulated within the first 5 components. Conditions can be separated with biological relevance up through PCA-5.

5.2.2 Few genes are significantly up or down regulated compared to baseline

When analyzing probe-based array data, the large data set is typically first filtered to the genes with expression values that are the most different between the treatment conditions and the

untreated, baseline condition[240]. A differentially expressed gene (DEG) for a given condition is identified by its fold change (FC) in expression to baseline as well as the statistical significance of that difference. The linear fold change of each gene is calculated using Equation 5.1, where *E* is the average expression (log2 transformed) of that gene for a specific condition or baseline. While somewhat arbitrary and with low statistical control[241] [242], the gold standard method of distinguishing DEGs is filtering by absolute fold change ($|FC| \geq 2.0$ and statistical significance of a False Discovery Rate (FDR) adjusted p-value ≤ 0.05.

Equation 5.1 $$\boldsymbol{Fold\ Change = 2^{(E_{condition} - E_{baseline})}}$$

Using this approach, 0 genes of the μHammer 21,488 gene data set were identified as a DEG for any condition examined. Prior assays performed at the 24-hour time point, however, demonstrated altered cellular processes as a result in injury and suggests corresponding expression change could have occurred. Therefore, a more liberal approach was employed to identify DEGs. The purpose of DEG identification, though, is to make biological predictions and guide the next steps of the investigation. While a generous filter criteria would inherently result in a larger set of DEGs, this approach would also be likely to introduce false positive DEGs, result in false predictions, and misguide follow-up investigations.

To reduce the downstream effect of errant false positives, the expression values from the probe-based array were first filtered into differentially expressed genes (DEGs) using a more lenient criteria, then further filtered into a subset of Focus Genes. As discussed in later sections of this chapter, predicted bioinformatic processes or pathways were only considered if the prediction was first based on a threshold number of Focus Genes. This second round of screening, thereby, provides a stricter criteria for a prediction to be considered, reducing false positives in the end result and focusing follow-up investigations.

Using the more lenient filtering method ($|FC| \geq 1.7$, p-value ≤ 0.05), 122 DEGs and 24 FGs were identified as a result of the μHammer device implementation identified, with only 4 of the 122 unique DEGs identified as a result of shear stress alone. There was no observable trend of predominantly up- or down-regulation across the four injury conditions (Figure 5.2A). The 42%-10μs shows a higher portion of down-regulated DEGs whereas 69%-1 ms shows a higher portion of increased expression DEGs. Injury conditions 42% - 1 ms and 69% - 10 μs display a relative balance between increased and decreased expression for corresponding DEGs. The most DEGs resulted from the 42% - 1 ms compressive strain group (54) and the fewest came from 69% -10 μs (11), as shown in volcano plots (Figure 5.2B).

Within the subset of 122 DEGs, 24 Focus Genes were identified by meeting one additional criteria of DEG: (1) common between at least 2 injury conditions, (2) $|FC| \geq 2$, (3) FDR p-value $\leq$ 0.05 (Figure 5.2C). Of these 24 Focus Genes, 14 had an absolute Fold Change of at least 2.0, 1 had an adjusted FDR p-value less than 0.05, and 14 were differentially expressed in more than one injury group. The majority of co-expressed genes are shared by 42% - 10 μs and 42% - 1 ms (Figure 5.2D). No genes are co-expressed between a compressive injury condition and the sham condition.

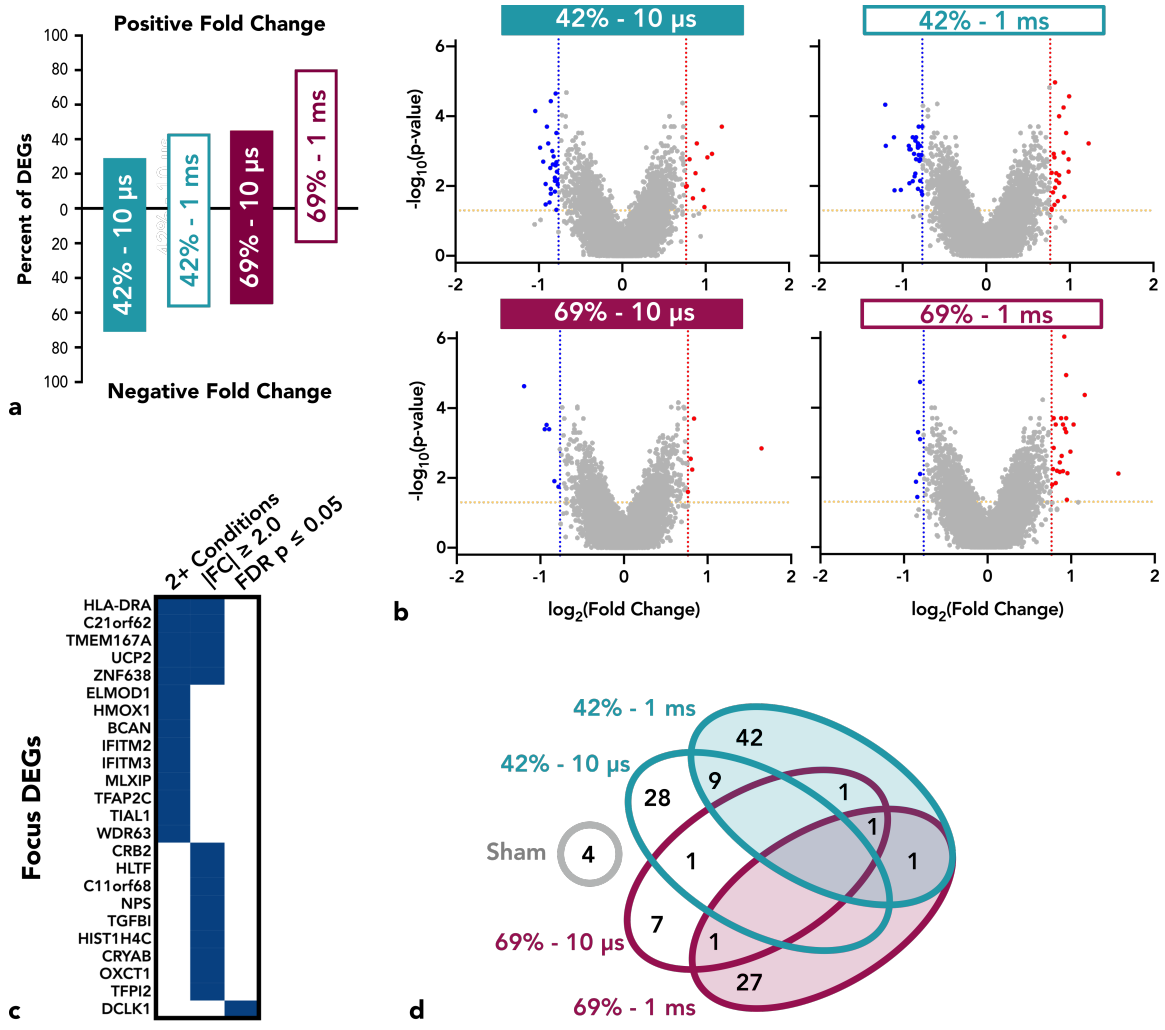

Figure 5.2 Differential gene expression analysis comparing compressive injury transcriptome to baseline expression. (a) The percent of differentially expressed genes in each injury condition up- and down-regulated. (b) Volcano plots displaying differential regulation of four compressive strain injuries compared to baseline. Blue dots indicate downregulation and red dots indicate upregulation, compared to baseline control. Yellow line depicts statistical significance cut-off at $p = 0.05$ ($\log_{10} = 1.3$). Red and blue lines depict significance cut-off at (+/-) 1.7-fold change, respectively. (c) Venn diagram of strain injury DEGs for each condition. (d) Focus genes identified by additional differential expression criteria: DEG common to at least 2 injury conditions (2+ Conditions), (+/-) 2.0-fold change (FC), or False Discover Rate (FDR) adjusted p-value < 0.05.

5.2.3 Bioinformatics

Two common bioinformatics tools were used to analyze the µHammer probe-based array gene expression (Figure 5.3). Ingenuity Pathway Analysis (IPA, Qiagen) was used to correlate the most

significant molecules (DEGs) to canonical pathways and molecular relationships previously published in literature. The significantly affected canonical pathways and molecular relationships identified by IPA were further filtered by those containing at least 2 focus genes (FCs) in order to reduce the likelihood of false positives.

Gene Set Enrichment Analysis (GSEA, Broad Institute) was in part established to interpret genome expression when there are only modest biological differences between two experimental conditions. Unlike IPA, which makes biological predictions based on only the most extremely affected (and arbitrarily determined) genes, GSEA is sensitive to the coordinated expression change of many genes in a known biological system, such as those curated through KEGG and Gene Ontology.

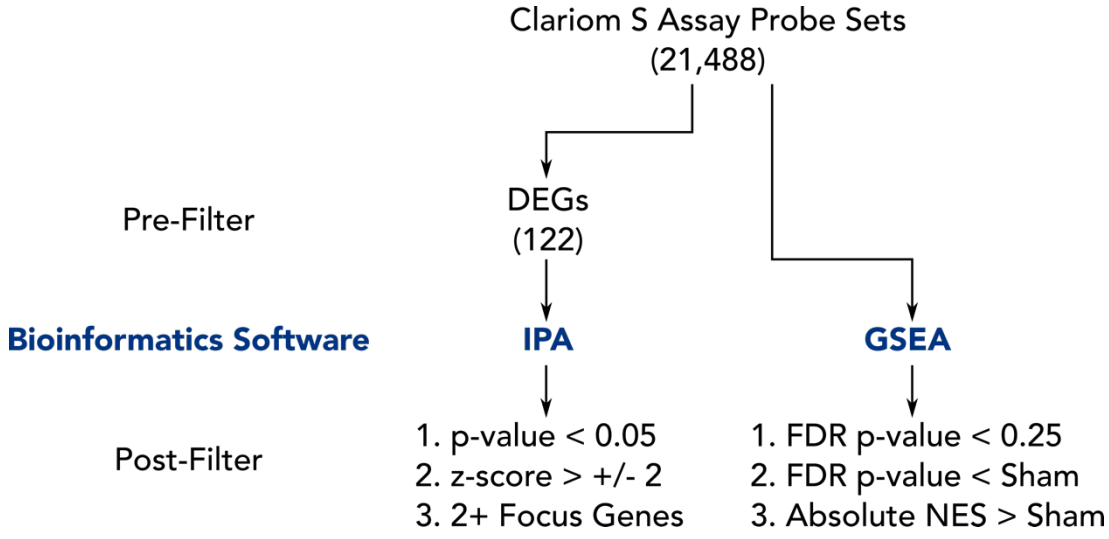

Figure 5.3 Two bioinformatics tools utilized for the probe-based array analysis. Both IPA and GSEA were used to investigate significantly affected molecular relationships after compressive strain. The 21,488 genes were filtered to only DEGs before input to IPA. The IPA results were further filtered for statistical significance and pathways resulting from 2 or more Focus Genes. All gene expression data was analyzed by GSEA and statistical significance was determined by both an FDR p-value < 0.25 as well as an FDR p-value less than the most significant sham condition analysis output. Similarly, significance was determined by an absolute Normalized Enrichment Score (NES) greater than the most enriched sham condition.

5.2.3.1 GSEA

Unlike IPA, GSEA utilizes the entire probe-based array gene expression. It orders the entire data set from high-to-low expression for a samples in a given experimental condition and low-to-high for the baseline samples. The extent to which genes within a particular gene set of interest are found at the top or bottom of the data set determines the correlation between the experimental conditions and the gene set. The statistical significance of one condition being more or less enriched in a gene set is calculated relative to a permuted distribution of the same samples[243 244].

GSEA was used to analyze the sets of genes within Gene Ontology (GO) categories as well as the Kyoto Encyclopedia of Genes and Genomes (KEGG), comparing each injury condition and sham to baseline. Combinations of injury conditions were also compared, such as total strained, 42% strain magnitude, 69% strain magnitude, 10 μs strain duration, and 1 ms strain duration – all compared to the baseline condition.

Within the GO gene sets, there was no significant enrichment for the 69% strain phenotype or 69% 10 μs, but there were several significantly enriched gene sets as a result of total compression, 42% strained, 42% - 10μs, 42% - 1ms, and 69% - 1ms (Figure 5.4A). The GO terms consisted predominantly of RNA processing terms and negatively enriched compared to baseline. For the KEGG gene sets, there was significant positive enrichment identified across all injury conditions examined, except for 69% - 1 ms (Figure 5.4B).

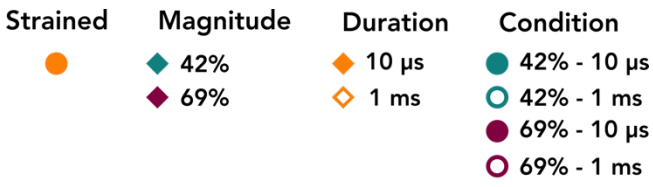
Strained
Magnitude
42%
69%
Duration
10 µs
1 ms
Condition
42% - 10 µs
42% - 1 ms
69% - 10 µs
69% - 1 ms

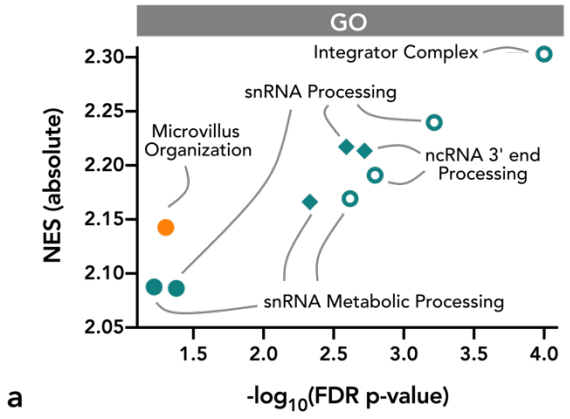
GO
Integrator Complex
snRNA Processing
Microvillus Organization
ncRNA 3' end Processing
snRNA Metabolic Processing
NES (absolute)
2.30
2.25
2.20
2.15
2.10
2.05
1.5
2.0
2.5
3.0
3.5
4.0
-log10(FDR p-value)

a

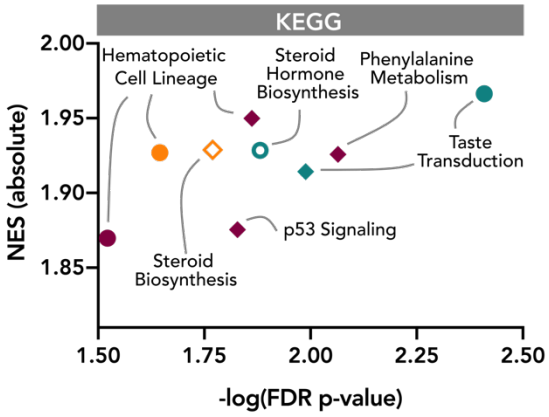
KEGG
Hematopoietic Cell Lineage
Steroid Hormone Biosynthesis
Phenylalanine Metabolism
Taste Transduction
p53 Signaling
Steroid Biosynthesis
NES (absolute)
2.00
1.95
1.90
1.85
1.50
1.75
2.00
2.25
2.50
-log(FDR p-value)

b

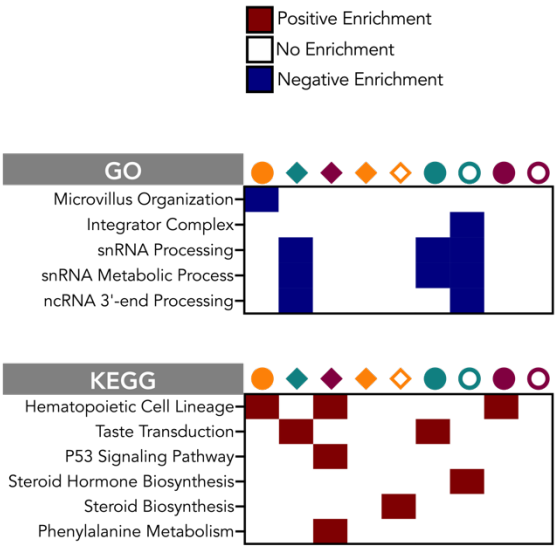
Positive Enrichment
No Enrichment
Negative Enrichment
GO
Microvillus Organization
Integrator Complex
snRNA Processing
snRNA Metabolic Process
ncRNA 3'-end Processing
KEGG
Hematopoietic Cell Lineage
Taste Transduction
P53 Signaling Pathway
Steroid Hormone Biosynthesis
Steroid Biosynthesis
Phenylalanine Metabolism

c

Figure 5.4 Gene Set Enrichment Analysis identified enrichments across GO and KEGG biological processes and functions is unique to compression parameter. Total average Log2 transformed gene expression data from the probe-based array was uploaded into GSEA. Samples were grouped based on the four compression parameters on the top key and nine conditions, in addition to sham, were compared to baseline. Statistically significant enrichments for the sham condition were identified by an FDR p-value ≤ 0.25. The highest significantly enriched sham result was used as the cutoff for the compression conditions. (a) Significantly enriched GO gene sets were identified by an FDR p-value ≤ 0.07 and absolute Normalized Enrichment Scores (NES) > 2.07 . (b) Significantly enriched KEGG gene sets were identified by an FDR p-value ≤ 0.03 and absolute Normalized Enrichment Scores (NES) > 1.82. (c) Heatmaps displaying 5 GO terms and 7 KEGG gene sets found to be significantly enriched across compression parameters with the direction of enrichment shown for positive (red) or negative (blue).

5.2.3.2 IPA

IPA identified statistically significant pathways and molecule relationships out of the 122 DEGs. Of these 122 DEGs, only 57 were utilized for the IPA predictions . While IPA predicted several affected upstream regulators and canonical pathways, an additional filter method was employed in order to reduce false positive correlations, due to the more lenient method of DEG identification described in Section 5.2.2. This second filter step reduced the IPA results to only those based on at least two molecules of interest from the Focus Genes list. Using this more stringent filtering, two canonical pathways and 3 upstream regulators were identified (Figure 5.5A).

Significant canonical pathways were predicted only for the 42% strain magnitude condition: Interferon Signaling and Neuroinflammation Signaling (Figure 5.5B). Significant upstream regulators were predicted across both the 42% strain magnitudes as well as the 1 ms strain duration: TP53, Lipopolysaccharide (LPS), and SMARCA4 (Figure 5.5C). Prior to applying the second filter, no significant pathways or regulators were identified for either the sham condition or the 69%-10 μs injury condition.

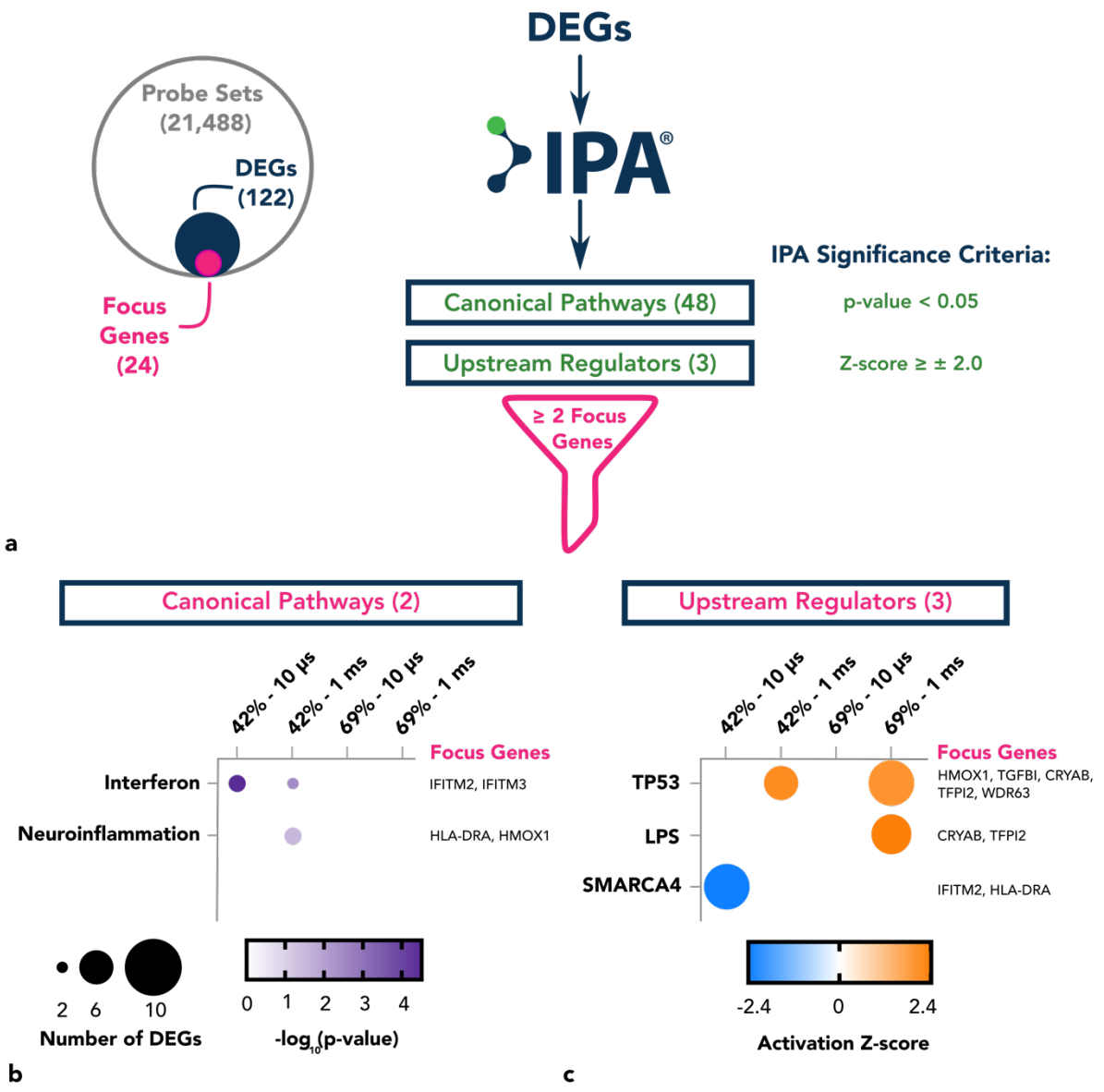

Figure 5.5 Ingenuity Pathway Analysis identified statistically significant canonical pathways and predicted upstream regulators. (a) The 122 DEGs were imported into IPA and significant correlations to canonical pathways and upstream regulators were determined by Fisher's Exact Test p-value ≤ 0.05 and $|\text{Z-score}| \geq 2.0$. The resulting canonical pathways (48) and upstream regulators (3) were further filtered to those comprising ≥ 2 Focus Genes. (b) Two canonical signaling pathways were identified: Interferon and Neuroinflammation. A circle plot color depicts the significance p-value and the size depicts the number of DEGs the pathway comprises, specific to each compression condition. (c) Three upstream regulators were identified: TP53, LPS, and SMARCA4. A circle plot color depicts the activation z-score and the size depicts the number of DEGs the regulator affects, specific to each compression condition.

5.2.4 Probe-based array validation by qPCR

The probe-based array enabled an exhaustive investigation of gene expression change as a result of compressive injury, but is limited in its statistical likelihood of false positives. Especially when utilizing a more lenient cutoff for differential expression, the legitimacy of each DEG is questionable. To validate these predictions, real-time PCR was used to quantify RNA expression to the specific copy number. This method is a more focused investigation, as it is unique for each gene of interest and provides sample-specific, quantified data, rather than relative differences.

Thus far, seven of the Focus Genes have been investigated, with four demonstrating statistically significant expression change between an injury group and the baseline (Figure 5.6A). The 42% - 1 ms injury condition is the most steadily differentially expressed across the examined genes, consistent with its stronger gene expression profile throughout the several probe-based array analyses.

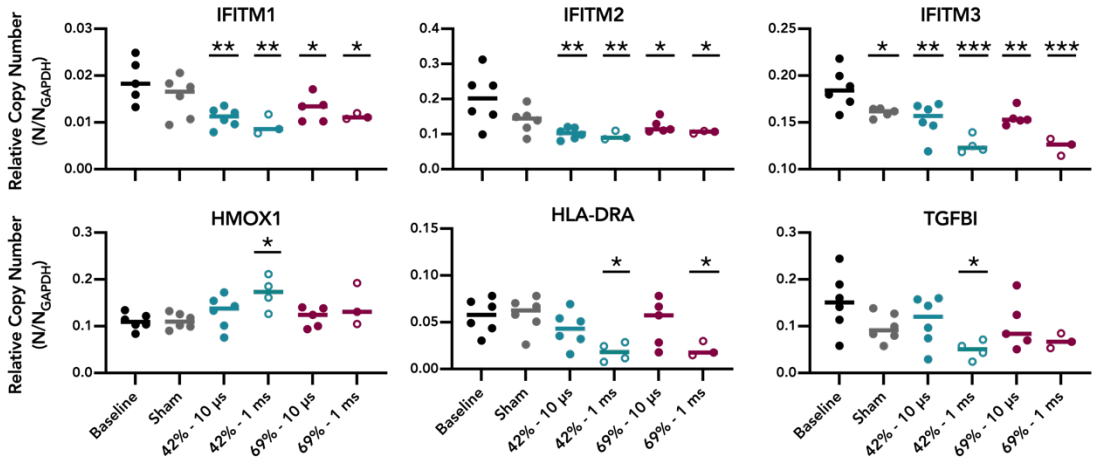

Figure 5.6 Quantitative Real-Time PCR expression of several genes of interest. Quantitative PCR for the validation of predicted enrichment or de-enrichment of key genes by probe-based array. Normalized copy number for genes of interest (GOI) to the housekeeping gene GAPDH which had no statistical difference in copy number between conditions. Statistics performed by One-Way ANOVA, post-hoc Dunnett's comparison of conditions to baseline, * = p-value ≤ 0.05, ** = p-value ≤ 0.01, *** = p-value ≤ 0.001.

As several genes of interest are validated by qPCR, the predicted pathways by IPA can be further established. The IPA predictions, statistically significant as well as predicted based on molecular interactions, and qPCR validated expressions are depicted in Figure 5.7A. The encoded protein localization for key molecules are illustrated in Figure 5.7B.

One pathway with qPCR validated genes is the Interferon Signaling Pathway. Classically, the interferon signaling is the result of ligand binding[245,246], when interferon proteins (IFNs) bind to the IFN receptors on the surface of a cell[114]. Composed of 2 subunits, the IFN Receptor is associated with Janus activated kinases (JAKs). Activated JAK phosphorylates signal transducer and activator of transcription 1 and 2 (STAT1 and STAT2). The STAT1-STAT2 (or STAT1-STAT1) complex moves to the nucleus where it binds to DNA, initiating gene transcription. There are many genes expressed through this pathway, each with unique biological effects. One set of expressed genes include the interferon-induced transmembrane (IFITM) proteins that contribute to cellular resistance[245–248], germ cell specification[249,250], and immune function[251].

Consisting of 3 primary proteins, IFITM1, 2, and 3, their expression has been shown to be invaluable in a cells protection against several viruses. While other IFN stimulated genes are responsible for preventing retroviral replication, the IFITM proteins also restrict viral entry into the cell. This first line of defense is achieved by increasing membrane rigidity and preventing its curvature, thereby blocking viral membrane fusion and pore formation[248].

Despite identifying both IFITM1 and IFITM2 as DEGS across several of the GEO data sets assessed, the correlation between the IFITM proteins and mechanical injury is minimal. There are a few tangentially related investigations, such as by Sebastian (2018) where mice with knee injuries were compared on their propensity to developing arthritis. It was shown that the group of ‘super healing’ mice had reduced IFITM1 and IFITM3 expression compared to the arthritic group

of mice, suggesting the involvement of this pathway in cell recovery[252]. Ibdi (2013) examined neurodevelopmental and cognitive abnormalities in mice and found these to be correlated with increased IFITM3 expression in astrocytes[253].

IFITM1, specifically, is found to be located on the plasma membrane of cells, with caveolae (CAV-1) it has been shown to inhibit ERK activity and positively regulate p53[254]. Astrocytes with CAV-1^{KO} strained to 155% magnitude by substrate stretch were also found to have increased pERK[255]. IFITM2 was found to act as the critical receptor for BCL2 binding on macrophages[256]. BCL2, a cell death regulator, is associated with several neurodegenerative diseases as well as TBI[81,257,85].

The HLA class II histocompatibility, DR alpha chain (HLA-DRA) is correlated to interferon signaling. Within a few hours of treating cells with IFN protein, HLA-DRA will be upregulated[258]. The validated reduced expression of all three IFITM genes as well as HLA-DRA after μHammer applied mechanical injury further indicate the repressed interferon signaling pathway at 24 hours post-injury.

IPA also predicted the upregulation of the SMARCA4 transcription factor, largely due to its relationship with Interferon Signaling as a co-activator[259]. The TP53 transcription factor was also predicted to be affected, but with increased expression. One downstream molecule repressed by the TP53 transcription factor is the Transforming Growth Factor Beta Induced (TGFBI) molecule. TGFBI is a secreted extracellular matrix protein, specifically after cellular treatment of TGFβ[260] and is largely associated with extracellular collagen. While not previously explored in regards to its relationship with mechanical injury, TGFβ has been identified as a cytokine that contributes to the secondary injury cascade in TBI[113,114]. IFITM3 is also associated in the cytoskeleton, specifically bound among many proteins comprising focal adhesions[261].

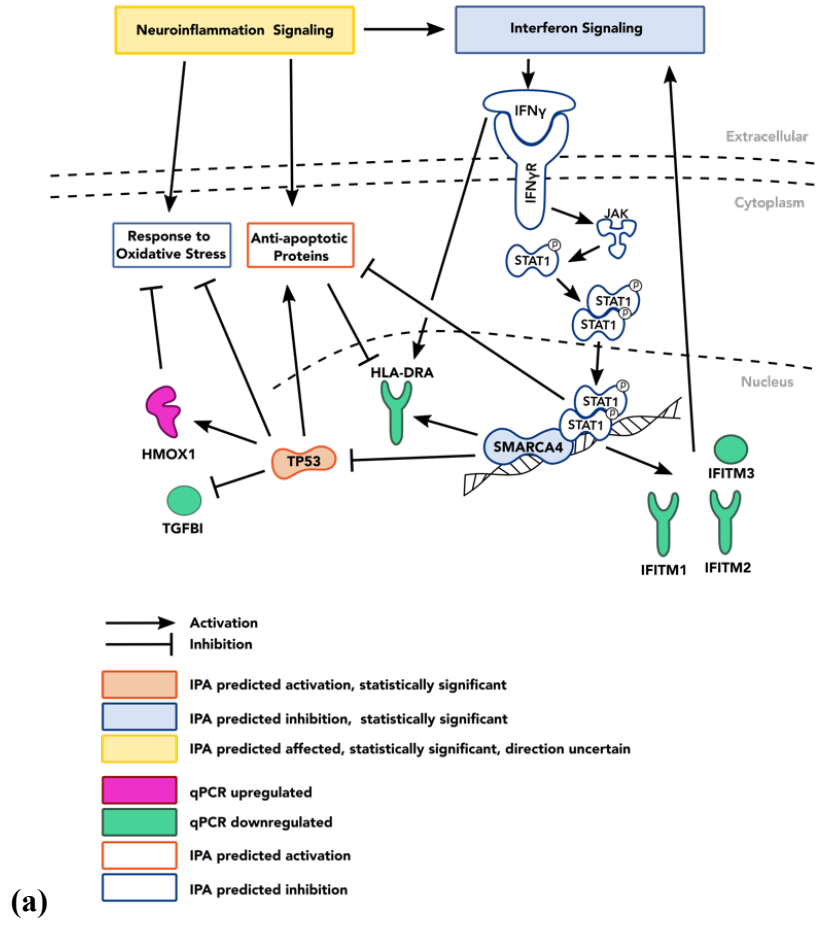
Neuroinflammation Signaling
Interferon Signaling
IFNγ
IFNγR
Extracellular
Cytoplasm
JAK
STAT1
STAT1
STAT1
Response to Oxidative Stress
Anti-apoptotic Proteins
HLA-DRA
Nucleus
STAT1
STAT1
HMOX1
TP53
SMARCA4
IFITM3
TGFBI
IFITM1
IFITM2
Activation
Inhibition
IPA predicted activation, statistically significant
IPA predicted inhibition, statistically significant
IPA predicted affected, statistically significant, direction uncertain
qPCR upregulated
qPCR downregulated
IPA predicted activation
IPA predicted inhibition

(a)

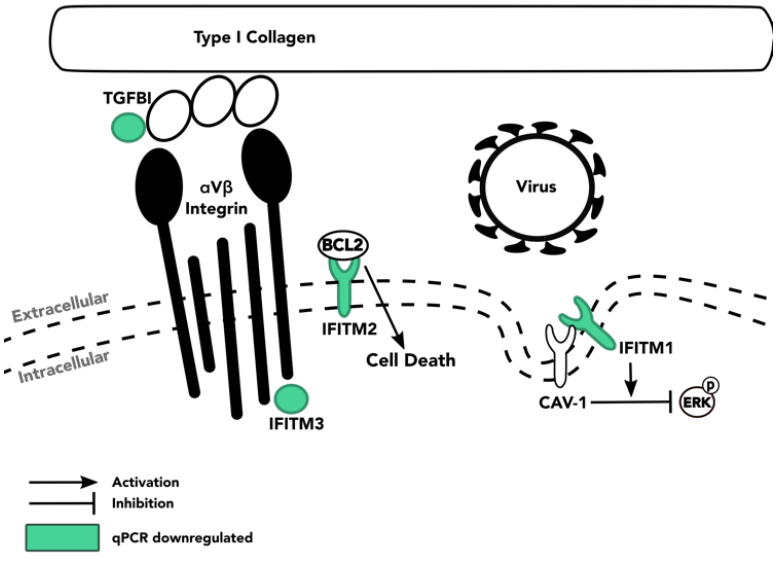
Type I Collagen
TGFBI
αVβ Integrin
Virus
BCL2
Extracellular
Intracellular
IFITM2
Cell Death
IFITM1
CAV-1
ERK
IFITM3
Activation
Inhibition
qPCR downregulated

(b)

Figure 5.7 Depiction of predicted IPA pathways and upstream regulators with validated molecules. (a) Simplified molecular interactions and cellular locations are shown between validated genes and their link to the IPA predictions. The predominant pathway validated thus far is the Interferon Signaling Pathway. While two molecules of the neuroinflammation pathway are also validated, the directionality of this pathway is still undetermined. The predicted up regulation of TP53 and down regulation of the SMARCA4 are also predicted by IPA.(b) Down regulated qPCR validated gene expressions translate proteins found to be localized to the plasma membrane. The three IFITM-family proteins with down-regulated gene expression are found to localize throughout the cell, including the plasma membrane. One function of the IFITM-family proteins is affecting the stiffness of the plasma membrane, shown to have anti-viral properties. IFITM2 and IFITM3 are depicted as transmembrane proteins. IFITM1 associates with Caveolin-1 and its inhibition of ERK while IFITM2 acts as a receptor for BCL2. IFITM3 has been found to be localized to focal adhesions while TGFBI is associated both with Integrin proteins and Collagen.

5.2.5 Samples predictably cluster based on few random genes

Euclidean distance is a commonly used metric in gene expression analysis, typically used to cluster similarly expressed genes in order to detect co-regulation[240]. The samples themselves can also be hierarchically clustered based on their paired Euclidean distances, offering an alternative avenue for exploration. Prior work has compared Euclidean distance to alternative methods of gene expression divergence, demonstrating its accuracy for comparing gene expression of homologous samples of differing source species[262,263].

Hierarchical clustering of the 23 samples of the probe-based array positioned them along a one dimensional axis. The position of each sample was based on Euclidean distance, such that nearest neighbors are most similar and farthest neighbors are most different. As shown in Figure 5.8, the ordering of the samples results in clear clustering of each injury condition. The sample ordering also demonstrates the three samples within each injury condition are more similar to each other than to other conditions. This ordering recapitulates the sample distribution in the PCA plots.

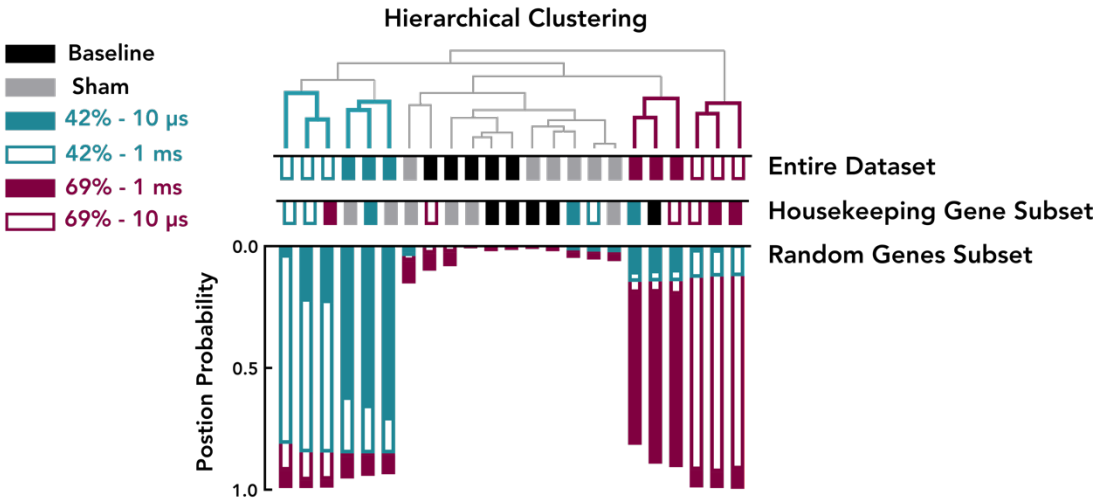

Figure 5.8 Hierarchical clustering of samples based on subset of probe-based array. The Euclidean distances between all pairs of the 23 samples is determined by their gene expression values. The samples are then ordered along 23 positions such that their farthest neighbor is the pair with the greatest average Euclidean distance. The full probe-based array gene expression data set (21,488 genes) orders the samples such that the 42% magnitude samples are the farthest from the 69% magnitude samples, with the 1 ms duration samples are the most different between the two magnitudes. Removing the 122 DEGs from the data set results in the same ordering of the samples, or with a matched pattern. An example ordering of 1000 random genes also matches the ordering and an example ordering of 500 random genes.

When the 122 DEGs are removed from the expression matrix, with 21,326 genes remaining, the samples continue to order in the same clustering pattern (not shown). Despite the DEGs inherently capturing the most differential expression, the sustained clustering of samples reveals that there was a lingering signature in the remaining low-differential gene set. This is further demonstrated when 500 random genes are selected out of the DEG-reduced data set and the samples still order and cluster with high probability as they had with the entire probe-based array data set.

To evaluate the strength, or fidelity, of the expression signature for compression parameters, the probability of matching the sample ordering of the full probe-based array with a reduced number of random genes was evaluated. Three compression parameters were compared: strain magnitude, strain duration, and specific conditions (Figure 5.9). The specific condition-matching

considered the positioning of the three samples within each injury condition. The three samples needed to be assembled next to each other, in the same order as with the full-probe set. The magnitude-matched considered the 6 samples within each magnitude condition as a group, where all 6 samples needed to position next to each other and the 2 magnitude groups needed to bookend the baseline and sham samples. Finally, the duration-matched again considered the 6 samples within each duration condition as a group, with the 1 ms samples positioned on the outermost ends and the 10 µs samples just within.

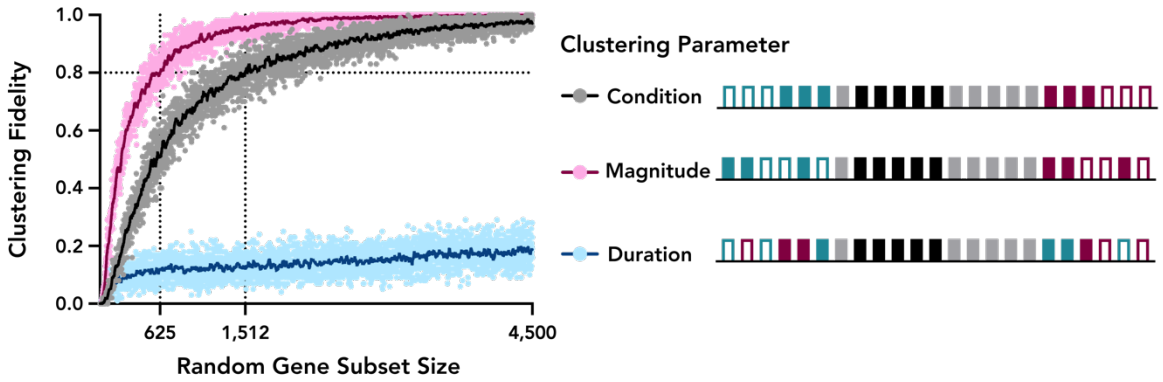

Figure 5.9 The probability of hierarchical clustering by clustering parameter and number of random genes. Probability of achieving the condition-, magnitude-, or duration-clustering dendrogram sample positioning of the entire data set by number of randomly selected genes (iterated 100 times). An example of sample ordering for each parameter is shown on the right. Points represent probability of clustering, line is the result of smoothing, to guide the eye and identify the gene subsite size of crossing 0.8 fidelity. Duration clustering does not reach 0.8 fidelity until the random gene subset size reaches 19,399 genes (not shown).

The probability of the samples clustering by each of the three method increased with mounting number of randomly selected genes. Across 100 iterations for each gene subset size, the samples clustered with 0.8 probability with the fewest number of genes by the magnitude clustering parameter. More than twice as many genes were necessary to cluster the samples with the same 0.8 fidelity in condition-specific clustering. While not shown, the Duration clustering method did

not reach 0.8 fidelity until 19,399 random genes. This demonstrates the stronger correlation between strain magnitude in the gene expression response than the strain duration.

To compare across each injury condition, the µHammer probe-based array data sets were reduced to the 11 control samples and the 3 samples for each specific injury condition. The Euclidean distance based clustering method was employed to determine the fewest number of genes required for the 3 injury samples to diverge from the control samples (Figure 10). Fewer than 1% of the total number of genes were necessary for each of the injury conditions to successfully diverge from the controls, with 95% probability.

The 42% - 1 ms injury condition diverged from the control samples to 0.7 fidelity with the fewest number of random genes (0.19% of total set, or 56 genes) whereas the 69% - 10 µs diverged at the most (0.33% of total set, or 71 genes). This difference in expression signature is consistent with the PCA, where the 69% - 10 µs was not regionally separated from the controls in PC1 or PC2 with the other injury conditions, but not until PC3.

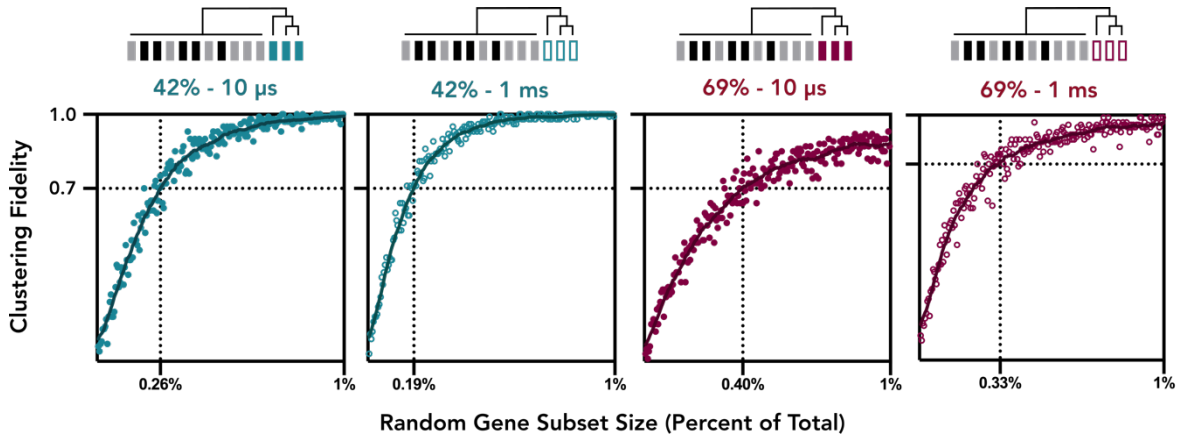

Figure 5.10: The divergence of injury conditions from controls with increasing number of random genes. Considering solely the samples within each injury condition to the baseline and sham samples, with DEGs removed, the probability of divergence of the injury samples from controls is shown across the number of random genes selected. The 42% - 1 ms condition diverges from the controls with the fewest number of random genes and the 69% - 10 µs condition diverges with the most number of random genes.

5.2.6 Comparing the μHammer transcriptome to published TBI and mechanical injury data sets

The mechanical parameters applied by the μHammer device to individual cells have largely been unexplored with prior methods, preventing direct comparisons between published gene expression and the μHammer probe-based array results. Previously published *in vivo* and *in vitro* transcriptome studies themselves also vary greatly across experimental conditions such as mechanical model, species, tissue, and post-injury time point of assessment, further obstructing direct comparison . Nevertheless, utilizing the NCBI Gene Expression Omnibus (GEO), a public repository for transcriptomic datasets, several *in vivo* TBI and *in vitro* bio-mechanical publications were selected for comparison .

Across 35 *in vivo* publications, the TBI models consisted of CCI, FPI, WDI, and bTBI. While the species were limited to rat, mouse, or human, the injury tissue examined consisted of 7 different types and the time points explored ranged from 30 minutes to 3 months (Figure 5.11).

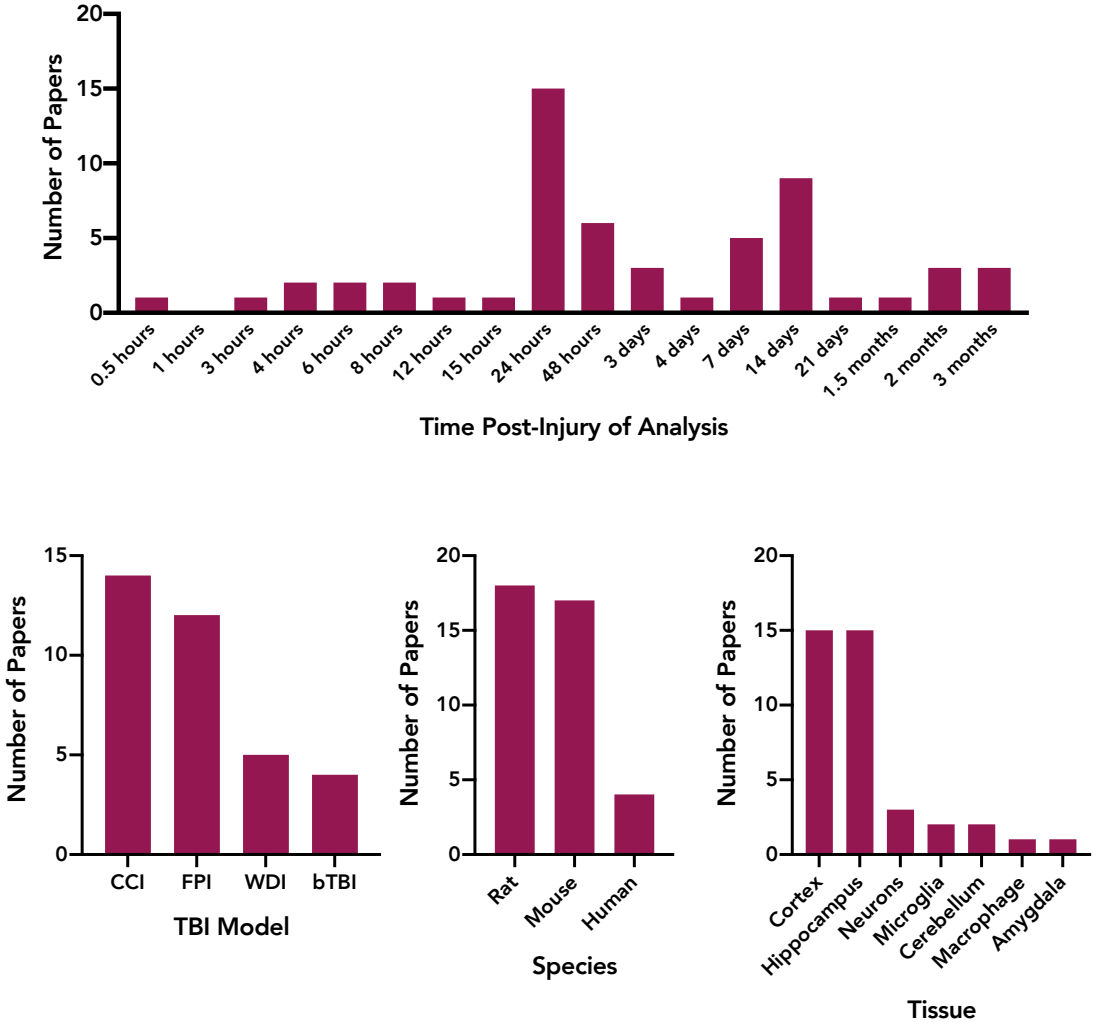

Figure 5.11: Summary of selected *in vivo* TBI studies, identified by availability of GEO Accession Data. The NCBI GEO repository was filtered to *in vivo* TBI studies and characterized by model and species used as well as tissue and time points analyzed. Depending on the publication, multiple models, species, tissues, and time points may have been investigated. [73,80,86,87,264–294]

Of the 21 *in vitro* publications, the species also ranged between rat, mouse, and human but there was a much wider range of cell types investigated (Figure 5.12). With higher control over mechanical parameters, the strain applied to the cells could also be compared across the published data. The vast majority of the studies applied tension to the cells, predominantly with a cyclic strain that never exceeded 20% magnitude.

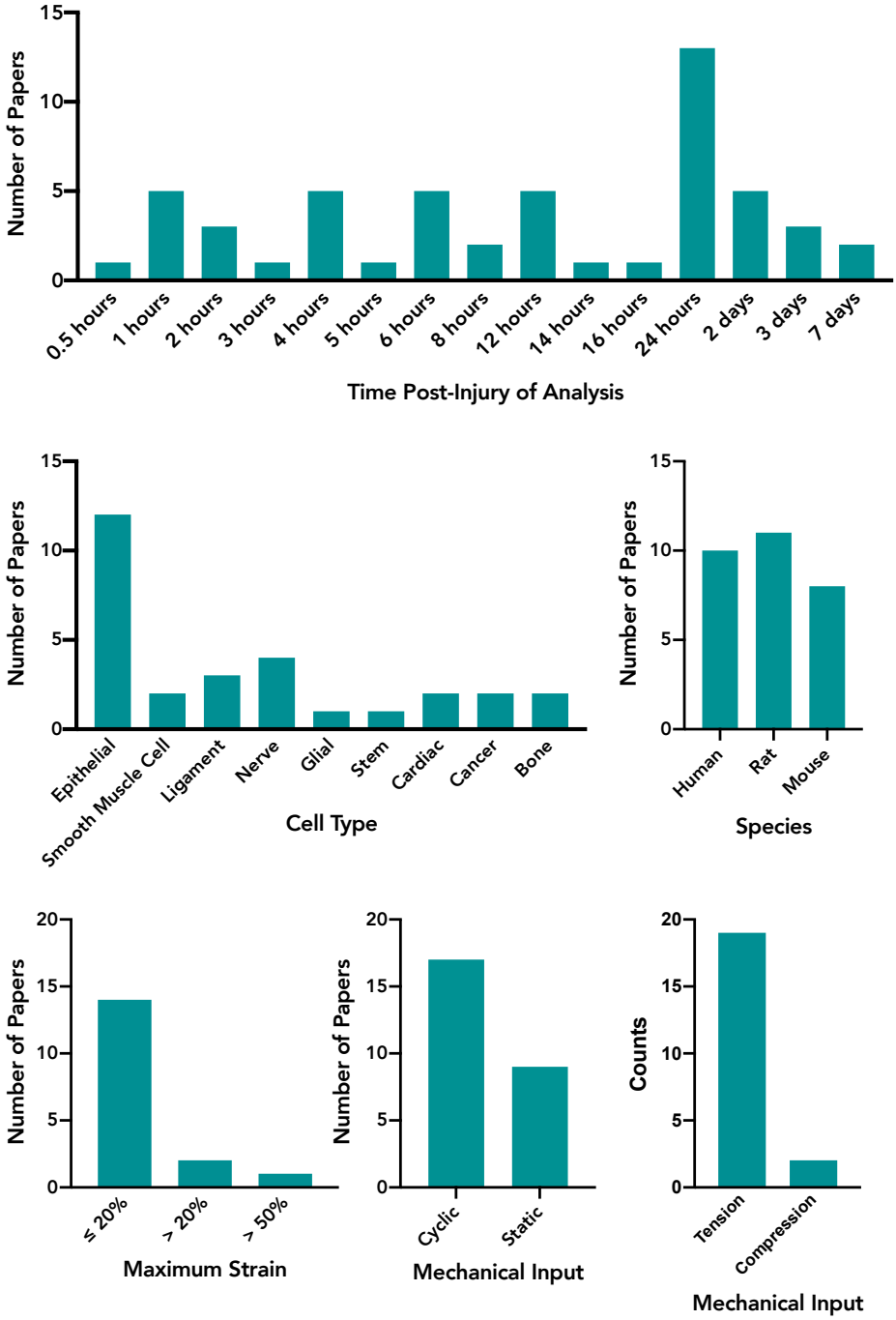

Figure 5.12: Summary of selected *in vitro* mechanical injury publications, identified by availability GEO Data Accession. The NCBI GEO repository was filtered to *in vitro* mechanical strain and compression studies. The available data sets were characterized by mechanical input parameters as well as cell type and source species as well as time points analyzed [188,295,304–313,296–303]

Despite the identified differences across the published studies, 7 gene expression data sets were selected for direct comparison to the μHammer. Criteria for selected included the data set containing a time point assessment of 24 hours post-injury and the tissue or cell type of interest having neural association – a distinction more influential across the *in vitro* studies. The DEGs of each of the 7 data sets and the μHammer DEGs were cross-checked to identify the extent to which they shared common DEGs (Figure 5.13). 3 of the data sets shared less than 50% of DEGs despite sharing several experimental conditions in common. While few DEGs were identified after μHammer compressive injury and practically no μHammer experimental characteristics matched the other experiments, the μHammer had over 1/3rd of its DEGs in common with the other 7 data sets.

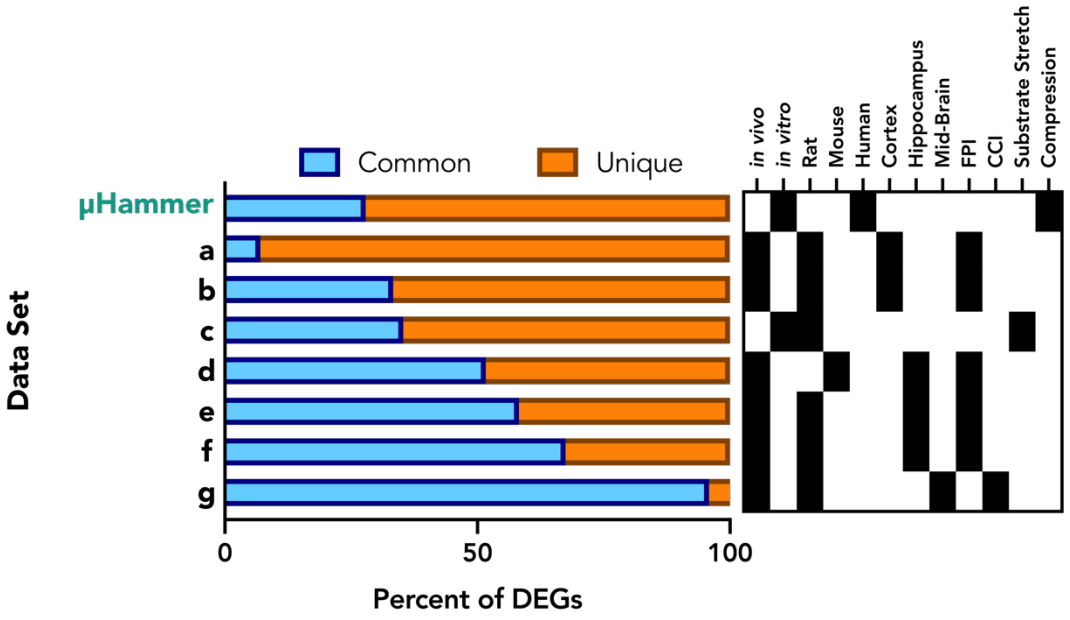

Figure 5.13: Comparison of DEGs identified by µHammer probe-based array and other TBI transcriptome studies. The NCBI Gene Expression Omnibus (GEO) was used to collect published TBI transcriptome data sets. 7 GSE data sets were selected based on samples collected at the 24-hour time point post-injury and compatibility with NCBI GEO2R, the tool used to perform fold change and statistical analysis. For each GSE data set, DEGs were identified by $|FC| \geq 1.7$ and p-value ≤ 0.05. (a) Heat map to visualize characterization of the GSE data sets used in the analysis. Bar chart shows the number of DEGs that are common across any two data sets. Data sets compared: a) Boone, D.R., PLoS One, 2019[i]. b) Natale, J.E., J. Neurotrauma, 2003. c) Wang, X., PLoS One, 2013 d) Rojo, D.R., PLoS One, 2011. e) Snell, S.L., PLoS One, 2019. f) Boone, D.R., PLoS One, 2019[ii]. g) White, T.E., BMC Genomics, 2013.

The GEO data sets were then assessed for a global gene signature by evaluating the extent to which the injured samples of these GEO data sets would continue to be successfully clustered. To determine whether each set contained a lingering gene signature, the samples within each set were ordered by hierarchical Euclidean distance. The number of genes required for the clustering of the injured or mechanically stimulated samples from the control samples was used to assess the strength of the gene signature of the conditions.

Of the 7 GEO data sets, 2 did not have injury samples that clustered from the control samples, despite data sets containing DEGs (|Fold Change > 2, FDR p-value < 0.05). For the

remaining, 3 data sets had 0.7 probability of clustering within 300 random genes (Figure 5.14). While this is a higher percent of genes than was necessary for clustering the µHammer samples, it still suggests a lingering global gene signature for this single data set. The strength of the global gene signature of the µHammer compression is potentially due to the high repeatability of the device and single-cell specificity of injury. Combined, resulting in homogenous expression change despite low magnitude of differential expression.

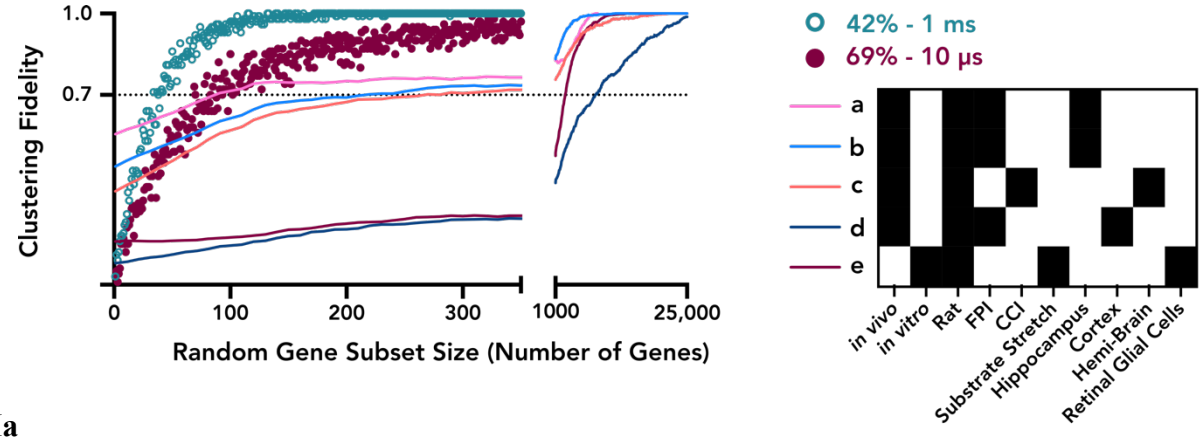

Ha

Figure 5.14: Probability of hierarchical clustering of injury conditions for several TBI and mechanical injury GEO data sets. The fidelity of gene expression hierarchical clustering was lower across the GEO data sets than the two µHammer compression conditions, 42% - 1 ms and 69% - 10 µs, representing the upper and lower bounds of µHammer clustering fidelity. Horizontal black dashed line guides the eye of 0.7 fidelity, determined by 100 iterations of random gene selection. Right heatmap depicts several characteristics of the GEO datasets compared: (a) Natale, J., J. Neurotrauma, 2003, (b) Rojo, D.R., PLoS One, 2011, (c) Boone, D.R., PLoS One, 2019, (d) Wang, X., PLoS One, 2013, (e) White, T.E., BMC Genomics, 2013.

5.3 Conclusions

In this study, 4 mechanical strains were applied to NPCs across 2 strain magnitudes and 2 strain durations. The transcriptome of the injured cells was analyzed 24 hours after injury by probe-based array, demonstrating unique gene expression for each compression condition. The magnitude of the gene expression change as a result of compression was not substantial, but further analysis

revealed a gene signature among the injured samples, unique from the baseline and sham samples that was retained even across < 1% of the total probe-based array data set.

Comparing the most differentially expressed genes as a result of the μHammer injury to prior TBI and mechanical injury data sets revealed that despite few DEGs from the μHammer injury, the percent of overlapping DEGs between experiments remained standard. Exploring the gene signature of these prior, published studies also further demonstrated the unique nature of the μHammer injury gene signature.

Bioinformatics tools were also used to correlate the μHammer injury gene expression to canonical signaling pathways and curated bio process gene sets. Molecules in the predicted down regulated Interferon Signaling pathway were then validated by qPCR alongside molecules associated with the predicted altered regulation Neuroinflammation Signaling Pathway and the TP53 transcription factor. Through this study, the mechanical injury applied by the μHammer device has enabled the exploration of new parameter spaces, such that novel mechanically sensitive pathways can be identified

5.4 Materials and Methods

5.4.1 Culture of ReNcell VM

The immortalized human Neural Progenitor Cell line, ReNcell VM (Millipore, USA) was cultured in ReNcell NSC Maintenance Media (Millipore, USA) supplemented with 20 ng/mL basic Fibroblast Growth Factor (bFGF, Millipore, USA) and 20 ng/mL Epidermal Growth Factor (EGF, Millipore, USA). Flasks were pre-treated with 20 μg/mL laminin (Millipore, USA) in DMEM/F12 without HEPES, with L-Glutamine (Corning, USA). Cells were seeded at 20,000 cm^2 on pre-treated tissue culture plates and incubated at 37ºC with 5% CO_2. For continued culture, cells were passaged every 2-3 days and up to 15 passages.

5.4.2 Injury using μHammer MEMS device

The NPCs are prepared first by enzymatic lifting by Accutase at 37ºC for 3 minutes. After the reaction is quenched with warm ReNcell Maintenance Media, the cells are pelleted at 300 g for 5 minutes and resuspended in Tyto Running Buffer™ (Miltenyi, Germany), filtered to remove particles greater than 20 μm diameter, and loaded into the sterile μHammer cartridge. Once the cartridge is housed within the MACSQuant® Tyto® Cell Sorter (Miltenyi, Germany) where it is maintained at 37ºC, low pressure (< 1kPa) is applied and cells pass from the loading chamber through the μHammer chip to the collection chamber of the cartridge.

Within the chip, the cell solution fluid flows at an approximate rate of 8 mL per hour. The compressed cells experienced either a moderate strain of 42.2% ± 7.4% or a high strain of 69.2 ± 12.1% for durations of 10 μs or 1000 μs. In all compression conditions, cells experienced similar applied strain rates of $\dot{\varepsilon} \sim 200 \times 10^3\ s^{-1} \pm 36 \times 10^3\ s^{-1}$. Two control populations were also analyzed for each experiment. In the sham condition, cells were flowed through the μHammer device without electromagnetic actuation of the μHammer impact face and subsequent cell compression. In the baseline condition, cells were never injected into the μHammer cartridge, but were instead cultured alongside the sham and compressed conditions.

5.4.3 Flow cytometric analysis

Sham and injured samples were removed from the output chamber of the μHammer cartridge. Samples were pelleted at 300 g for 5 minutes and resuspended in NSC Media. An aliquot was removed from each sample to which propidium iodide (PI, 5% v/v) was added. The aliquot's viability and cell concentration was determined by MACSQuant Flow Cytometer. Viable cells (PI^-) were seeded at 20,000 viable cells/cm on pre-laminated flasks for continued culture.

5.4.4 RNA isolation

Total RNA was isolated using RNeasy micro kit (Qiagen), following the manufacturers' protocol and RNA was stored in RNAse free water at -80ºC for downstream applications. Purity of RNA was assessed using NanoDrop One, followed by precipitation to improve purity as needed.

5.4.5 Probe-based array Processing

RNA was isolated after 24 hours of culture. RNA integrity was verified using a 2200 TapeStation (Agilent Technologies, USA) and only samples with RINe > 9 were chosen for probe-based array. In total, 24 samples (Baseline and Sham, n = 6 ; Compressed, n = 3) across 3 experimental replicates were adjusted to a concentration of 50 ng/μL and sent to Thermo Fisher Laboratories (USA) where RNA analysis was undertaken. The samples underwent hybridization to the human Affymetrix Clariom S assay. Quality control performed by Thermo Fisher Laboratories recommended the removal of one Baseline sample from further analysis, resulting in a total of 23 acceptable samples for further analysis.

Transcriptome Analysis Console (TAC v 4.0) software (Thermo Fisher) was used to normalize the expression for each gene probe set, generated using the SST-RMA algorithm. In short, signal values for probe expression were first background-adjusted and the average of the probes within a probe set were computed using One-Step Tukey's Bi-weight Algorithm, then scaled by removing the values of the highest and lowest 2% of observations. Variability due to experimental replicate was removed using Batch Effect. Differential expression analysis for 21,488 probe sets was performed across all experimental conditions by comparing to the baseline condition. Significantly expressed genes were identified by a threshold of $p \leq 0.05$, determined by empirical Bayesian One-Way ANOVA, with absolute fold change to baseline ($|FC|$) ≥ 1.7. In total, 122 differentially expressed genes (DEGs) were identified. Of these DEGs, 23 were identified for greater focus

(Focus Genes). These were DEGs that were identified across more than one injury condition, had a $|FC| \geq 2.0$, or had a corrected p-value ≤ 0.05. Focus Genes are listed in Table X.

5.4.6 qPCR

Reverse transcription of RNA into cDNA was performed using Superscript II (Invitrogen, X). The specific primers were designed using NCBI primer blast and supplied through Eurofins Genomics (USA). Sequences are provided in Supplementary Table X. All thermocycling was performed using QuantStudio 5 (Thermo Fisher, USA). cDNA was amplified using NEBNext® High Fidelity 2X PCR Master Mix (New England Bio, USA) for 35 cycles at 98ºC/10 sec, 69ºC/30 s, and 72ºC/10 sec. Amplified products were resolved in 1.8% agarose gel followed by QIAquick Gel Extraction Kit (Qiagen, USA).

RT-qPCR was carried out using SYBR-green-based master mix (Thermo Fisher Scientific, USA). GAPDH was used as reference housekeeping gene and all samples and standards were carried out in duplicate for each RT-qPCR assay. The primers used are listed in Table 5.4.6. Both relative quantification and absolute quantification were performed, using the mean cycle threshold (Ct) value for each sample. Relative expression was determined as the fold-change to baseline using the $\Delta\Delta$Ct method ($2^{-\Delta\Delta Ct}$). Absolute fold-change was determined as the ratio of each gene of interest copy number to the GAPDH copy number.

Table 5.2 List of primers used

Gene	Forward	Reverse
TGFB1	TACCTGAACCCGTGTTGCTCTC	GTTGCTGAGGTATCGCCAGGAA
IFITM(1,2,3)	CTGGGCTTCATAGCATTCGCCT	AGATGTTCAGGCACTTGGCGGT
IFITM3	GCCTACTCCGTGAAGTCTAGGG	CCATAGGCCTGGAAGATCAGCA
HMOX1	CCAGGCAGAGAATGCTGAGTTC	AAGACTGGGCTCTCCTTGTTGC
TFPI2	TACTGGCTGTGGAGGGAATGAC	CGGATTCTACTGGCAAAGCGAAG
HLA-DRA	AGCTGTGGACAAAGCCAACCTG	CTCTCAGTTCCACAGGGCTGTT
GAPDH	GTCTCCTCTGACTTCAACAGCG	ACCACCCTGTTGCTGTAGCCAA
DCLK1	ACCGATGCCATCAAGCTGGACT	TCCTGGTAACGGAACTTCTCCG
C11orf68	TCTCGGGCAAGTGGCTTATG	CCGTGAAGTCGTCCGTGTAA
NES	CTGGCGCACCTCAAGATGTC	CTCCAGCTTGGGGTCCTGAAA

5.4.7 Probe-based array Distance Measures and Hierarchical Clustering

An *m* x *n* matrix of the gene expression profiles was used to determine similarity between each of the 23 experimental samples. The gene expression matrix contained 23 sample-specific columns and *m* gene-specific rows, where each row contained the logarithmic (base 2) transformed expression for a specific gene. The Euclidean distances between samples for each gene were calculated using Equation 5.2.

Equation 5.2: $$d_{A,B} = \sqrt{\sum_{i=1}^{N}(e_{Ai} - e_{Bi})^2}$$

The effect of total number of genes selected ($1 \leq N \leq 21{,}488$) and comprised genes on the average Euclidean distances between samples were then visualized through hierarchical binary clustering, where the ordering of the 23 samples maximized similarities between adjacent samples.

The number of randomly selected genes ranged from 1 gene to the full data set. The resulting hierarchical clustering for each was compared to the sample ordering of the full data set by three methods. The first method, condition-match, accepted the pattern if the sample of a given injury condition was positioned in one of the three positions taken by the same condition in the full data set. The second method, magnitude-match, accepted the pattern as matching if each sample was clustered with samples of its same injury magnitude. Similarly, the third method, duration-match, accepted the pattern if each sample clustered with samples of its same duration. As there is no information retained in the directionality of the pattern, the each iteration's ordering was also matched to the reverse ordering of the full dataset. By iterating the process 100 times, the probability of each match for a given number of random genes was determined.

In order to isolate the gene expression divergence of each individual injury condition to the controls, the full dataset was first reduced to the only 14 samples: baseline (5), sham (6), and the injury condition of interest (3). The DEGs specific for each condition were then removed for the corresponding dataset. Essentially, the condition-matching method was employed and the probability of the condition clustering was determined with increasing number of random genes, again by iterating 100 times for each random gene number selection.

5.4.8 Gene Expression Omnibus Data Comparison

The NCBI Gene Expression Omnibus (GEO) was used to collect gene expression data sets focused on TBI or mechanical injury. Data sets of interest were identified by availability of expression values, specifically those that accommodate GEO2R capability. Data sets also required connection to a published journal article as well as control or sham samples in addition to the TBI or mechanical injury samples.

In vivo TBI data sets were selected for DEG identification based on the time point of expression analysis post-injury, specifically 24-hours. In total, 6 data sets matched this requirement. Two of the 6 data sets have the same GEO Accession number (GSE11452) and have been additionally labeled for distinction. *In vitro* mechanical injury data sets were similarly selected for DEG identification based on 24-hour post-injury analysis but also were limited to those with samples from a neural cell type. In total, 1 data set matched this requirement. DEG identification for GEO data sets were all performed using GEO2R, filtered to $|FC| \geq 1.7$ and $p \leq 0.05$.

These same GEO data sets were used for hierarchical sample clustering. Each of the GEO data sets were first hierarchically ordered based on average Euclidean distance between paired samples. Of the 7 data sets, only those with successful injury sample clustering were selected - such that the injury samples were distinct from control samples. The probability of sample clustering with increasing number of randomly selected genes by condition-matching method was determined.

5.4.9 Ingenuity Pathway Analysis

The probe-based array DEGs were imported into Ingenuity Pathway Analysis Software (IPA, Ingenuity Systems, USA) along with for each experimental condition the corresponding average logarithmic (base 2) transformed expression, average fold change to baseline, and average p-value for statistical significance of difference to baseline. IPA then generated semantic associations of the DEGs to canonical pathways, upstream regulator predictions, and interaction networks. Significance of the canonical pathways and interaction networks were determined by a right-tailed Fisher's Exact Test p-value ≤ 0.05 and significance of predicted upstream regulators were determined by an absolute z-score ≥ 2, where a z-score ≤ -2 predicts down regulation and a z-score ≥ 2 predicts upregulation. Significant canonical pathways and upstream regulators were further filtered to those with predictions based on at least 2 molecules from the 24 Focus Genes. Relevant

interaction networks were filtered to those with at least 6 common molecules shared between compression conditions.

5.4.10 Gene Set Enrichment Analysis

Gene Set Enrichment Analysis (GSEA) was performed using the normalized, log 2 transformed probe-based array gene expression for each sample. Individual injury conditions (n = 3), sham (n = 6), total strained (n=12), 42% strained (n = 6), and 69% strained (n = 6) were compared to baseline (n=5) to determine phenotype enrichment across curated gene sets from Gene Ontology and KEGG. Statistical significance of results were determined by permuting the gene sets 1,000 times to establish null enrichment. Significantly enriched gene sets were conservatively identified by an FDR p-value ≤ 0.25. These gene sets were further filtered to those more significant than set identified by the sham samples, with an FDR p-value ≤ 0.07 and FDR p-value ≤ 0.03 for Gene Ontology and KEGG, respectively.

5.4.11 Statistical Analysis

Unless otherwise specified, statistical comparisons between compressed, sham, and the control groups were performed using One-way ANOVA and post-hoc Dunnett's test, $\alpha = 0.05$. All statistics were performed using GraphPad Prism v 8.0.

6 Future Directions and Conclusions

6.1 μHammer Future Applications

In this dissertation, my collaborators and I have investigated the neural progenitor cell (NPC) response to compressive strain, applied to single cells by the μHammer with unprecedented strain rate. The effects on the NPCs were then compared across several published Traumatic Brain Injury (TBI) and mechanical stimulation models, across *in vivo* and *in vitro*. As discussed

in Chapters 2 and 5, these publications span many species and cell types, let alone magnitude and duration of applied mechanical stimulus.

Therefore, an area of interest for the future μHammer work would be to compare the effect of this unique injury spectrum to more cell types. The process flow for the μHammer has already been shown to accommodate the K562 leukemia cell line and the human NPC line but the vast majority of biomechanical investigations utilize other cell types, such as osteocytes[314]. Bone cells have well characterized responses to strain and can be used as a benchmark for better understanding the effect of the unprecedented strain rate applied by the μHammer.

The μhammer could also be used to investigate more cellular components of TBI. For example, resident microglial cells in the brain respond to TBI by activating and inducing detectable inflammatory responses within hours of injury. As described in Chapter 2, inflammation can persist for months to years, aiding neurodegeneration as well as potentially triggering the dysregulation that leads to immunosuppression[315]. Microglial cells will be isolated from tissue and compressed using the μHammer, across a range of strain magnitudes and strain durations. The effect of strain on microglial function and transcriptome could be used to detect potential immunosuppression signaling related to injury severity.

6.2 Global Gene Expression Signature

The unique signature of the μHammer compressed cells displayed a potentially over-looked method for discerning gene expression changes. Despite a low magnitude of differential gene expression, the μHammer compressed cells had non-random clustering based on a handful of genes. This concept of a global gene expression signature is not well explored and it would be worthwhile to determine its limits for practical application.

Continuing to cluster publicly available data sets would provide ample opportunity to compare across different cell types and input perturbations. For example, the effect shown by the μHammer could be unique to NPCs or to all stem and progenitor cell types. It could also be unique to mechanical perturbation only, due to the non-specific nature of the input.

6.3 Conclusions

In this dissertation, my collaborators and I have developed the μHammer device for applying single cell compression with unprecedent high strain rate. Due to the high throughput nature and the single-cell, repeatable compression profile of the μHammer device, statistically relevant biological comparisons can be made.

Using the ReNcell VM NPC line (Millipore), I have decoupled the effects of strain magnitude and strain duration on the viability loss as a result of compression. There was a correlation between strain magnitude and immediate viability loss whereas there was a correlation between strain duration and early apoptosis.

I have also investigated the effect of both strain parameters on NPC transcription 24 hours after injury. These gene expression changes demonstrated down-regulation of the neuroinflammation signaling pathway. Further, TP53, SMARCA4, and the IFITM-family were predicted as novel mechanically sensitive and regulatory molecules in this pathway. Additionally, the gene expression data demonstrates a unique injury signature across the compressed samples, despite low magnitude differential gene expression. This finding demonstrates another beneficial aspect of the high repeatability and single-cell nature of the μHammer compressive injury.

While there are several existing methods to apply mechanical stimulus to cells *in vitro* as well as in several *in vivo* TBI models, no previous method has been able to achieve the low strain duration in conjunction with high strain magnitude capable by the μHammer. More so, no previous

method applies large strain in conjunction with high strain rate. The defined, single-cell impacts applied by the μHammer make this device exceptionally suited for studying cellular response to mechanical injury. Through a better understanding of how cells respond to injury, there can be advances in the development of effective cell-targeted therapies for mechanically induced, degenerative diseases like TBI.

References

1. Dewan, M. C. *et al.* Estimating the global incidence of traumatic brain injury. *J. Neurosurg.* **130**, 1080–1097 (2019).
2. Galgano, M. *et al.* Traumatic Brain Injury: Current Treatment Strategies and Future Endeavors. *Cell Transplant.* **26**, 1118–1130 (2017).
3. Ramos-Cejudo, J. *et al.* Traumatic Brain Injury and Alzheimer's Disease: The Cerebrovascular Link. *EBioMedicine* **28**, 21–30 (2018).
4. Morganti-Kossmann, M. C., Semple, B. D., Hellewell, S. C., Bye, N. & Ziebell, J. M. The complexity of neuroinflammation consequent to traumatic brain injury: from research evidence to potential treatments. *Acta Neuropathologica* **137**, 731–755 (2019).
5. Xie, C. *et al.* The effect of simvastatin treatment on proliferation and differentiation of neural stem cells after traumatic brain injury. *Brain Res.* **1602**, 1–8 (2015).
6. Yu, T. S., Zhang, G., Liebl, D. J. & Kernie, S. G. Traumatic brain injury-induced hippocampal neurogenesis requires activation of early nestin-expressing progenitors. *J. Neurosci.* **28**, 12901–12912 (2008).
7. Ng, S. Y. & Wah, L. A. Y. Traumatic Brain Injuries: Pathophysiology and Potential Therapeutic Targets. *Front. Cell. Neurosci.* **13**, (2019).
8. McKinnon, K. M. Flow cytometry: an overview. *Curr Protoc Immunol.* **120**, (2019).
9. Böhmer, R. M., Bandala-Sanchez, E. & Harrison, L. C. Forward light scatter is a simple measure of T-cell activation and proliferation but is not universally suited for doublet discrimination. *Cytom. Part A* **79 A**, 646–652 (2011).
10. Ramirez, J. M. *et al.* Side scatter intensity is highly heterogeneous in undifferentiated pluripotent stem cells and predicts clonogenic self-renewal. *Stem Cells Dev.* **22**, 1851–1860 (2013).
11. Yuan, S. H. *et al.* Cell-surface marker signatures for the Isolation of neural stem cells, glia and neurons derived from human pluripotent stem cells. *PLoS One* **6**, (2011).
12. Herzenberg, L. A. *et al.* The history and future of the Fluorescence Activated Cell Sorter and flow cytometry: A view from Stanford. *Clin. Chem.* **48**, 1819–1827 (2002).
13. Richardson, G. M., Lannigan, J. & Macara, I. G. Does FACS perturb gene expression? *Cytom. Part A* **87**, 166–175 (2015).
14. Box, A. *et al.* Evaluating the effects of cell sorting on gene expression. *J. Biomol. Tech.* **31**, 100–111 (2020).

15. Yumoto, M. *et al.* Evaluation of the effects of cell-dispensing using an inkjet-based bioprinter on cell integrity by RNA-seq analysis. *Sci. Rep.* **10**, 3–4 (2020).
16. Llufrio, E. M., Wang, L., Naser, F. J. & Patti, G. J. Sorting cells alters their redox state and cellular metabolome. *Redox Biol.* **16**, 381–387 (2018).
17. Huber, D., Oskooei, A., Casadevall Solvas, X., Andrew Demello & Kaigala, G. V. Hydrodynamics in Cell Studies. *Chem. Rev.* **118**, 2042–2079 (2018).
18. Varma, S. & Voldman, J. A cell-based sensor of fluid shear stress for microfluidics. *Lab Chip* **15**, 1563–1573 (2015).
19. Foster, John, S., Grummit, Daryl, W., Harley, John, C., Spong, Jaquelin, K. & Turner, K. L. MEMS particle sorting actuator and method of manufacture. **2**, (2013).
20. Russo, G., Zegar, C. & Giordano, A. Advantages and limitations of microarray technology in human cancer. *Oncogene* **22**, 6497–6507 (2003).
21. Kumar, S. Cellular mechanotransduction: Stiffness does matter. *Nature Materials* **13**, 918–920 (2014).
22. Hochmuth, R. M. Micropipette aspiration of living cells. *J. Biomech.* **33**, 15–22 (2000).
23. Yeh, Y. T. *et al.* Three-dimensional forces exerted by leukocytes and vascular endothelial cells dynamically facilitate diapedesis. *Proc. Natl. Acad. Sci. U. S. A.* **115**, 133–138 (2018).
24. Bastounis, E. E., Yeh, Y. T. & Theriot, J. A. Subendothelial stiffness alters endothelial cell traction force generation while exerting a minimal effect on the transcriptome. *Sci. Rep.* **9**, 1–16 (2019).
25. Campàs, O. *et al.* Quantifying cell-generated mechanical forces within living embryonic tissues. *Nat. Methods* **11**, 183–189 (2014).
26. Ayad, N. M. E., Kaushik, S. & Weaver, V. M. Tissue mechanics, an important regulator of development and disease. *Philos. Trans. R. Soc. B Biol. Sci.* **374**, (2019).
27. MacManus, D. B., Pierrat, B., Murphy, J. G. & Gilchrist, M. D. A viscoelastic analysis of the P56 mouse brain under large-deformation dynamic indentation. *Acta Biomater.* **48**, 309–318 (2017).
28. Pervin, F. & Chen, W. W. Dynamic mechanical response of bovine gray matter and white matter brain tissues under compression. *J. Biomech.* **42**, 731–735 (2009).
29. Cullen, D. K. & LaPlaca, M. C. Neuronal response to high rate shear deformation depends on heterogeneity of the local strain field. *J. Neurotrauma* **23**, 1304–1319 (2006).
30. Caporizzo, M. A. *et al.* Strain-Rate Dependence of Elastic Modulus Reveals Silver Nanoparticle Induced Cytotoxicity. *Nanobiomedicine* **2**, (2015).
31. Rigato, A., Miyagi, A., Scheuring, S. & Rico, F. High-frequency microrheology reveals cytoskeleton dynamics in living cells. *Nat. Phys.* **13**, 771–775 (2017).
32. Lulevich, V., Zink, T., Chen, H. Y., Liu, F. T. & Liu, G. Y. Cell mechanics using atomic force microscopy-based single-cell compression. *Langmuir* **22**, 8151–8155 (2006).
33. Raj, A., Dixit, M., Doble, M. & Sen, A. K. A combined experimental and theoretical approach towards mechanophenotyping of biological cells using a constricted microchannel. *Lab Chip* **17**, 3704–3716 (2017).
34. Lin, J. *et al.* High-throughput physical pxhenotyping of cell differentiation. *Microsystems Nanoeng.* **3**, 17013 (2017).
35. Dudani, J. S., Gossett, D. R., Tse, H. T. K. & Di Carlo, D. Pinched-flow hydrodynamic stretching of single-cells. *Lab Chip* **13**, 3728–3734 (2013).
36. Urbanska, M. *et al.* A comparison of microfluidic methods for high-throughput cell

deformability measurements. *Nat. Methods* **17**, (2020).
37. Darling, E. M. & Di Carlo, D. High-Throughput Assessment of Cellular Mechanical Properties. *Annu. Rev. Biomed. Eng.* **17**, 35–62 (2015).
38. Guillou, L. *et al.* Measuring Cell Viscoelastic Properties Using a Microfluidic Extensional Flow Device. *Biophys. J.* **111**, 2039–2050 (2016).
39. Gossett, D. R. *et al.* Hydrodynamic stretching of single cells for large population mechanical phenotyping. *Proc. Natl. Acad. Sci.* **109**, 7630–7635 (2012).
40. Nyberg, K. D. *et al.* Quantitative Deformability Cytometry: Rapid, Calibrated Measurements of Cell Mechanical Properties. *Biophys. J.* **113**, 1574–1584 (2017).
41. Hoffman, B. D. & Crocker, J. C. Cell Mechanics: Dissecting the Physical Responses of Cells to Force. *Annu. Rev. Biomed. Eng.* **11**, 259–288 (2009).
42. Gillespie, P. G. & Walker, R. G. Molecular basis of mechanosensory transduction. *Nature* **413**, 194–202 (2001).
43. Cox, C. D. *et al.* Removal of the mechanoprotective influence of the cytoskeleton reveals PIEZO1 is gated by bilayer tension. *Nat. Commun.* **7**, 1–13 (2016).
44. Wang, Y. & Xiao, B. The mechanosensitive Piezo1 channel: structural features and molecular bases underlying its ion permeation and mechanotransduction. *J. Physiol.* **596**, 969–978 (2018).
45. Coste, B. *et al.* Piezo1 and Piezo2 are essential components of distinct mechanically activated cation channels. *Science (80-.).* **330**, 55–60 (2010).
46. Bratengeier, C., Liszka, A., Hoffman, J., Bakker, A. D. & Fahlgren, A. High shear stress amplitude in combination with prolonged stimulus duration determine induction of osteoclast formation by hematopoietic progenitor cells. *FASEB J.* **34**, 3755–3772 (2020).
47. Maingret, F., Patel, A. J., Lesage, F., Lazdunski, M. & Honoré, E. Lysophospholipids open the two-pore domain mechano-gated K+ channels TREK-1 and TRAAK. *J. Biol. Chem.* **275**, 10128–10133 (2000).
48. Poole, K., Moroni, M. & Lewin, G. R. Sensory mechanotransduction at membrane-matrix interfaces. *Pflugers Arch. Eur. J. Physiol.* **467**, 121–132 (2014).
49. Lim, C. G., Jang, J. & Kim, C. Cellular machinery for sensing mechanical force. *BMB Rep.* **51**, 623–629 (2018).
50. Maurer, M. & Lammerding, J. The Driving Force: Nuclear Mechanotransduction in Cellular Function, Fate, and Disease. *Physiol. Behav.* **21**, 443–468 (2019).
51. Ricci, A. J., Kennedy, H. J., Crawford, A. C. & Fettiplace, R. The transduction channel filter in auditory hair cells. *J. Neurosci.* **25**, 7831–7839 (2005).
52. Qiu, X. & Müller, U. Mechanically gated ion channels in mammalian hair cells. *Front. Cell. Neurosci.* **12**, 1–10 (2018).
53. Alenghat, F. J. & Ingber, D. E. Mechanotransduction: All Signals Point to Cytoskeleton, Matrix, and Integrins. *Sci. Signal.* **2002**, pe6–pe6 (2002).
54. Kuehlmann, B., Bonham, C. A., Zucal, I., Prantl, L. & Gurtner, G. C. Mechanotransduction in Wound Healing and Fibrosis. *J. Clin. Med.* **9**, 1423 (2020).
55. Duscher, D. *et al.* Mechanotransduction and fibrosis. *J. Biomech.* **47**, 1997–2005 (2014).
56. Maurer, M. & Lammerding, J. The Driving Force: Nuclear Mechanotransduction in Cellular Function, Fate, and Disease. *Annu. Rev. Biomed. Eng.* **21**, 443–468 (2019).
57. Wang, N. *et al.* Mechanical behavior in living cells consistent with the tensegrity model. *Proc. Natl. Acad. Sci. U. S. A.* **98**, 7765–7770 (2001).
58. Kirby, T. J. & Lammerding, J. Emerging views of the nucleus as a cellular

mechanosensor. *Nat. Cell Biol.* **20**, 373–381 (2018).
59. Uhler, C. & Shivashankar, G. V. Regulation of genome organization and gene expression by nuclear mechanotransduction. *Nat. Rev. Mol. Cell Biol.* **18**, 717–727 (2017).
60. Vining, K. H. & Mooney, D. J. Mechanical forces direct stem cell behaviour in development and regeneration. *Nature Reviews Molecular Cell Biology* **18**, 728–742 (2017).
61. Pajerowski, J. D., Dahl, K. N., Zhong, F. L., Sammak, P. J. & Discher, D. E. Physical plasticity of the nucleus in stem cell differentiation. *Proc. Natl. Acad. Sci. U. S. A.* **104**, 15619–15624 (2007).
62. Stephens, A. D., Banigan, E. J., Adam, S. A., Goldman, R. D. & Marko, J. F. Chromatin and lamin a determine two different mechanical response regimes of the cell nucleus. *Mol. Biol. Cell* **28**, 1984–1996 (2017).
63. Miroshnikova, Y. A., Nava, M. M. & Wickström, S. A. Emerging roles of mechanical forces in chromatin regulation. *J. Cell Sci.* **130**, 2243–2250 (2017).
64. Clause, K. C., Liu, L. J. & Tobita, K. Directed stem cell differentiation: The role of physical forces. *Cell Communication and Adhesion* **17**, 48–54 (2010).
65. Makhija, E. *et al.* Mechanical strain alters cellular and nuclear dynamics at early stages of oligodendrocyte differentiation. *Front. Cell. Neurosci.* **12**, 59 (2018).
66. Rhim, J. H. *et al.* A High-content screen identifies compounds promoting the neuronal differentiation and the midbrain dopamine neuron specification of human neural progenitor cells. *Sci. Rep.* **5**, 1–14 (2015).
67. Nierode, G. J. *et al.* High-throughput identification of factors promoting neuronal differentiation of human neural progenitor cells in microscale 3D cell culture. *Biotechnol. Bioeng.* **116**, 168–180 (2019).
68. Stolberg, S. & McCloskey, K. E. Can shear stress direct stem cell fate? *Biotechnol. Prog.* **25**, 10–19 (2009).
69. Hecht, P. M., Ballesteros-Yanez, I., Grepo, N., Knowles, J. A. & Campbell, D. B. Noncoding RNA in the transcriptional landscape of human neural progenitor cell differentiation. *Front. Neurosci.* **9**, 1–11 (2015).
70. Keating, C. E. & Cullen, D. K. Mechanosensation in traumatic brain injury. *Neurobiol. Dis.* **148**, 105210 (2020).
71. Davis, J. E. *et al.* Methodological considerations regarding single-cell gene expression profiling for brain injury. *Neurochemical Research* **29**, 1113–1121 (2004).
72. Samal, B. B. *et al.* Acute Response of the Hippocampal Transcriptome Following Mild Traumatic Brain Injury After Controlled Cortical Impact in the Rat. *J. Mol. Neurosci.* **57**, 282–303 (2015).
73. Meng, Q. *et al.* Traumatic Brain Injury Induces Genome-Wide Transcriptomic, Methylomic, and Network Perturbations in Brain and Blood Predicting Neurological Disorders. *EBioMedicine* **16**, 184–194 (2017).
74. Rojo, D. R. *et al.* Influence of stochastic gene expression on the cell survival rheostat after traumatic brain injury. *PLoS One* **6**, (2011).
75. Lamprecht, M. R. *et al.* Strong correlation of genome-wide expression after traumatic brain injury in vitro and in vivo implicates a role for SORLA. *J. Neurotrauma* **34**, 97–108 (2017).
76. Wu, J. C. C. *et al.* Location and level of Etk expression in neurons are associated with varied severity of traumatic brain injury. *PLoS One* **7**, (2012).

77. Zhang, X. Y. *et al.* Analysis of key genes and modules during the courses of traumatic brain injury with microarray technology. *Genet. Mol. Res.* **13**, 9220–9228 (2014).
78. Michael, D. B., Byers, D. M. & Irwin, L. N. Gene expression following traumatic brain injury in humans: Analysis by microarray. *J. Clin. Neurosci.* **12**, 284–290 (2005).
79. Chandran, R. *et al.* Differential expression of microRNAs in the brains of mice subjected to increasing grade of mild traumatic brain injury. *Brain Inj.* **31**, 106–119 (2017).
80. von Gertten, C., Morales, A. F., Holmin, S., Mathiesen, T. & Nordqvist, A. C. S. Genomic responses in rat cerebral cortex after traumatic brain injury. *BMC Neurosci.* **6**, 1–11 (2005).
81. Wong, Y. H. *et al.* Temporal genetic modifications after controlled cortical impact—understanding traumatic brain injury through a systematic network approach. *Int. J. Mol. Sci.* **17**, 216 (2016).
82. Boone, D. R. *et al.* Traumatic brain injury induces long-lasting changes in immune and regenerative signaling. *PLoS One* **14**, (2019).
83. Anderson, G. D. *et al.* The effect of progesterone dose on gene expression after traumatic brain injury. *J. Neurotrauma* **28**, 1827–1843 (2011).
84. Zhang, J. *et al.* Transcriptional profiling in rat hair follicles following simulated blast insult: A new diagnostic tool for traumatic brain injury. *PLoS One* **9**, (2014).
85. White, T. E. *et al.* Bilateral gene interaction hierarchy analysis of the cell death gene response emphasizes the significance of cell cycle genes following unilateral traumatic brain injury. *BMC Genomics* **17**, (2016).
86. Natale, J. E., Ahmed, F., Cernak, I., Stoica, B. & Faden, A. I. Gene Expression Profile Changes Are Commonly Modulated across Models and Species after Traumatic Brain Injury. *J. Neurotrauma* **20**, 907–927 (2003).
87. Lipponen, A. *et al.* Transcription factors Tp73, Cebpd, Pax6, and Spi1 rather than DNA methylation regulate chronic transcriptomics changes after experimental traumatic brain injury. *Acta Neuropathol. Commun.* **6**, 17 (2018).
88. Michael J. Kane. Altered Gene Expression in Cultured Microglia in Response to Simulated Blast Overpressure: Possible Role of Pulse Duration Michael. *Neurosci. Lett.* **522**, 47–51 (2012).
89. Zhou, J. *et al.* Temporal changes in cortical and hippocampal expression of genes important for brain glucose metabolism following controlled cortical impact injury in mice. *Front. Endocrinol. (Lausanne).* **8**, (2017).
90. Lipponen, A., Paananen, J., Puhakka, N. & Pitkanen, A. Analysis of Post-Traumatic Brain Injury Gene Expression Signature Reveals Tubulins, Nfe2l2, Nfkb, Cd44, and S100a4 as Treatment Targets. *Sci. Rep.* **6**, (2016).
91. Yazdani, A. Effect of Blast Exposure on Gene-Gene Interactions. *arXiv Genomics* doi:arXiv:1809.05095v2
92. Whiteneck, G. G., Cuthbert, J. P., Corrigan, J. D. & Bogner, J. A. Prevalence of self-reported lifetime history of traumatic brain injury and associated disability: A statewide population-based survey. *J. Head Trauma Rehabil.* **31**, E55–E62 (2016).
93. Alghnam, S., AlSayyari, A., Albabtain, I., Aldebasi, B. & Alkelya, M. Long-term disabilities after traumatic head injury (THI): a retrospective analysis from a large level-I trauma center in Saudi Arabia. *Inj. Epidemiol.* **4**, (2017).
94. Ruet, A. *et al.* A detailed overview of long-term outcomes in severe traumatic brain injury eight years post-injury. *Front. Neurol.* **10**, 1–13 (2019).

95. Liu, S., Yin, F., Zhang, J. & Qian, Y. The role of calpains in traumatic brain injury. *Brain Injury* **28**, 133–137 (2014).
96. Jarrahi, A. *et al.* Revisiting traumatic brain injury: From molecular mechanisms to therapeutic interventions. *Biomedicines* **8**, 1–42 (2020).
97. *Report to Congress on Mild Traumatic Brain Injury in the United States: Steps to Prevent a Serious Public Health Problem*. *National Center for Injury Prevention and Control, Center for Disease Control and Prevention* (2003).
98. Hernandez, F. *et al.* Lateral impacts correlate with falx cerebri displacement and corpus callosum trauma in sports-related concussions. *Biomech. Model. Mechanobiol.* **18**, 631–649 (2019).
99. Hernandez, F. *et al.* Six Degree of Freedom Measurements of Human Mild Traumatic Brain Injury. *Ann Biomed Eng* **43**, 1918–1934 (2015).
100. Xiong, Y., Mahmood, A. & Chopp, M. Animal models of traumatic brain injury. *Nat. Rev. Neurosci.* **14**, 128–142 (2013).
101. Bar-Kochba, E., Scimone, M. T., Estrada, J. B. & Franck, C. Strain and rate-dependent neuronal injury in a 3D in vitro compression model of traumatic brain injury. *Sci. Rep.* **6**, (2016).
102. Sherman, S. A. *et al.* Stretch Injury of Human Induced Pluripotent Stem Cell Derived Neurons in a 96 Well Format. *Sci. Rep.* **6**, (2016).
103. Morganti-Kossmann, M. C., Satgunaseelan, L., Bye, N. & Kossmann, T. Modulation of immune response by head injury. *Injury* **38**, 1392–1400 (2007).
104. Yang, Q. *et al.* Will Sirtuins Be Promising Therapeutic Targets for TBI and Associated Neurodegenerative Diseases? *Front. Neurosci.* **14**, 1–15 (2020).
105. Chan, D. D. *et al.* Mechanostasis in apoptosis and medicine. *Progress in Biophysics and Molecular Biology* **106**, 517–524 (2011).
106. Hu, S., Chen, J., Butler, J. P. & Wang, N. Prestress mediates force propagation into the nucleus. *Biochem. Biophys. Res. Commun.* **329**, 423–428 (2005).
107. Boldogh, I. R. *et al.* Maintaining the SA Protein Complex Containing Mdm10p, Mdm12p, and Mmm1p Links Mitochondrial Membranes and DNA to the Cytoskeleton-based Segregation Machineryhape of Nerve Cells. *Mol. Biol. Cell* **14**, 4618–4627 (2003).
108. Knight, M. M. *et al.* Chondrocyte deformation induces mitochondrial distortion and heterogeneous intracellular strain fields. *Biomech. Model. Mechanobiol.* **5**, 180–191 (2006).
109. Normoyle, K. P. *et al.* The emerging neuroprotective role of mitochondrial uncoupling protein-2 in traumatic brain injury. *Transl. Neurosci.* **6**, 179–186 (2015).
110. Brand, M. D. & Esteves, T. C. Physiological functions of the mitochondrial uncoupling proteins UCP2 and UCP3. *Cell Metab.* **2**, 85–93 (2005).
111. Bechmann, I. *et al.* Brain mitochondrial uncoupling protein 2 (UCP2): A protective stress signal in neuronal injury. *Biochem. Pharmacol.* **64**, 363–367 (2002).
112. Puntambekar, S. S., Saber, M., Lamb, B. T. & Kokiko-Cochran, O. N. Cellular players that shape evolving pathology and neurodegeneration following traumatic brain injury. *Brain, Behavior, and Immunity* **71**, 9–17 (2018).
113. Almad, A., Sahinkaya, F. R. & McTigue, D. M. Oligodendrocyte Fate after Spinal Cord Injury. *Neurotherapeutics* **8**, 262–273 (2011).
114. Benveniste, E. N. Cytokine Actions in the Central Nervous System. *Cytokine + Growth Factor Rev.* **8**, 3–148 (1998).

115. Fujikawa, D. G. The Role of Excitotoxic Programmed Necrosis in Acute Brain Injury. *Computational and Structural Biotechnology Journal* **13**, 212–221 (2015).
116. Tehse, J. & Taghibiglou, C. The overlooked aspect of excitotoxicity: Glutamate-independent excitotoxicity in traumatic brain injuries. *Eur. J. Neurosci.* **49**, 1157–1170 (2019).
117. McKee, C. A. & Lukens, J. R. Emerging roles for the immune system in traumatic brain injury. *Front. Immunol.* **7**, 1–17 (2016).
118. Loane, D. J. & Kumar, A. Microglia in the TBI brain: The good, the bad, and the dysregulated. *Experimental Neurology* **275**, 316–327 (2016).
119. Jassam, Y. N., Izzy, S., Whalen, M., McGavern, D. B. & El Khoury, J. Neuroimmunology of Traumatic Brain Injury: Time for a Paradigm Shift. *Neuron* **95**, 1246–1265 (2017).
120. Chodobski, A., Zink, B. J. & Szmydynger-Chodobska, J. Blood-Brain Barrier Pathophysiology in Traumatic Brain Injury. *Translational Stroke Research* **2**, 492–516 (2011).
121. Pogoda, K. & Janmey, P. A. Glial tissue mechanics and mechanosensing by glial cells. *Frontiers in Cellular Neuroscience* **12**, 25 (2018).
122. Llorens-Bobadilla, E. & Martin-Villalba, A. Adult NSC diversity and plasticity: the role of the niche. *Curr. Opin. Neurobiol.* **42**, 68–74 (2017).
123. Nemirovich-Danchenko, N. M. & Khodanovich, M. Y. New neurons in the post-ischemic and injured brain: Migrating or resident? *Front. Neurosci.* **13**, (2019).
124. Bauer, S., Kerr, B. J. & Patterson, P. H. The neuropoietic cytokine family in development, plasticity, disease and injury. *Nature Reviews Neuroscience* **8**, 221–232 (2007).
125. Drago, D. *et al.* The stem cell secretome and its role in brain repair. *Biochimie* **95**, 2271–2285 (2013).
126. Lu, J. *et al.* Histone deacetylase inhibitors are neuroprotective and preserve NGF-mediated cell survival following traumatic brain injury. *Proc. Natl. Acad. Sci. U. S. A.* **110**, 10747–10752 (2013).
127. Chang, E. H. *et al.* Traumatic brain injury activation of the adult subventricular zone neurogenic niche. *Front. Neurosci.* **10**, (2016).
128. Theus, M. H., Ricard, J., Bethea, J. R. & Liebl, D. J. EphB3 Inhibits the expansion of Neural Progenitor Cells in the SVZ by Regulating During Homeostasis and Following Traumatic Brain Injury. *Stem Cells* **28**, 1231–1242 (2011).
129. Ramaswamy, S., Goings, G. E., Soderstrom, K. E., Szele, F. G. & Kozlowski, D. A. Cellular proliferation and migration following a controlled cortical impact in the mouse. *Brain Res.* **1053**, 38–53 (2005).
130. Petrik, D. *et al.* Epithelial Sodium Channel Regulates Adult Neural Stem Cell Proliferation in a Flow-Dependent Manner. *Cell Stem Cell* **22**, 865-878.e8 (2018).
131. Gennarelli, T. A. Animate Models of Human Head Injury. *J. Neurotrauma* **11**, 357–368 (1994).
132. Dai, J. X., Ma, Y. Bin, Le, N. Y., Cao, J. & Wang, Y. Large animal models of traumatic brain injury. *International Journal of Neuroscience* **128**, 243–254 (2013).
133. Wojnarowicz, M. W., Fisher, A. M., Minaeva, O. & Goldstein, L. E. Considerations for experimental animal models of concussion, traumatic brain injury, and chronic traumatic encephalopathy-these matters matter. *Front. Neurol.* **8**, 1 (2017).
134. Albert-Weissenberger, C. & Sirén, A. L. Experimental traumatic brain injury. *Experimental and Translational Stroke Medicine* **2**, (2010).

135. Thompson, H. J. *et al.* Lateral fluid percussion brain injury: A 15-year review and evaluation. *J. Neurotrauma* **22**, 42–75 (2005).
136. Lyeth, B. G. Historical review of the fluid-percussion TBI model. *Front. Neurol.* **7**, 1–7 (2016).
137. Hicks, R., Soares, H., Smith, D. & McIntosh, T. Temporal and spatial characterization of neuronal injury following lateral fluid-percussion brain injury in the rat. *Acta Neuropathol.* **91**, 236–246 (1996).
138. Bramlett, H. M. & Dietrich, W. D. Quantitative structural changes in white and gray matter 1 year following traumatic brain injury in rats. *Acta Neuropathol.* **103**, 607–614 (2002).
139. Kabadi, S. V., Hilton, G. D., Stoica, B. A., Zapple, D. N. & Faden, A. I. Fluid-percussion-induced traumatic brain injury model in rats. *Nat. Protoc.* **5**, 1552–1563 (2010).
140. Flygt, J. *et al.* Neutralization of Interleukin-1β following Diffuse Traumatic Brain Injury in the Mouse Attenuates the Loss of Mature Oligodendrocytes. *J. Neurotrauma* **35**, 2837–2849 (2018).
141. Abdul-Muneer, P. M., Long, M., Conte, A. A., Santhakumar, V. & Pfister, B. J. High Ca2+ Influx During Traumatic Brain Injury Leads to Caspase-1-Dependent Neuroinflammation and Cell Death. *Mol. Neurobiol.* **54**, 3964–3975 (2017).
142. Arneson, D. *et al.* Single cell molecular alterations reveal target cells and pathways of concussive brain injury. in *Nature Communications* **9**, (2018).
143. Osier, N. D. & Dixon, C. E. The controlled cortical impact model: Applications, considerations for researchers, and future directions. *Front. Neurol.* **7**, 1–14 (2016).
144. Osier, N. D., Korpon, J. R. & Dixon, C. E. Controlled Cortical Impact Model. in *Brain Neurotrauma: Molecular, Neuropsychological, and Rehabilitation Aspects* (CRC Press/Taylor & Francis, 2015).
145. Osier, N. & Dixon, C. E. Mini review of controlled cortical impact: A well-suited device for concussion research. *Brain Sci.* **7**, (2017).
146. Mary K. Tripp, PhD, M. The Controlled Cortical Impact Model of Experimental Brain Trauma: Overview, Research Applications, and Protocol. *Methods Mol Biol.* **1462**, 177–192 (2016).
147. Wang, Y. *et al.* Protection against TBI-Induced Neuronal Death with Post-Treatment with a Selective Calpain-2 Inhibitor in Mice. *J. Neurotrauma* **35**, 105–117 (2017).
148. Manley, G. T. *et al.* Controlled cortical impact in swine: Pathophysiology and biomechanics. *J. Neurotrauma* **23**, 128–139 (2006).
149. Zhang, L. *et al.* Inhibition of Epac2 attenuates neural cell apoptosis and improves neurological deficits in a rat model of traumatic brain injury. *Front. Neurosci.* **12**, 1–10 (2018).
150. Gennarelli, T. A. *et al.* Diffuse axonal injury and traumatic coma in the primate. *Ann. Neurol.* **12**, 564–574 (1982).
151. Gutierrez, E. *et al.* A new model for diffuse brain injury by rotational acceleration: I model, gross appearance, and astrocytosis. *J. Neurotrauma* **18**, 247–257 (2001).
152. Laksari, K., Sadeghipour, K. & Darvish, K. Mechanical response of brain tissue under blast loading. *J. Mech. Behav. Biomed. Mater.* **32**, 132–144 (2014).
153. Säljdö, A., Bao, F., Haglid, K. G. & Hansson, H. A. Blast exposure causes redistribution of phosphorylated neurofilament subunits in neurons of the adult rat brain. *J. Neurotrauma* **17**, 719–726 (2000).

154. Cernak, I. Animal models of head trauma. *NeuroRx* **2**, 410–422 (2005).
155. Statler, K. D., Jenkins, L. W. & Dixon, C. E. Experimental Traumatic Brain Injury Research to the Bedside. *J. Neurotrauma* **18**, 1195–1206 (2001).
156. Vickers, S. P., Jackson, H. C. & Cheetham, S. C. Animal modelling of traumatic brain injury in preclinical drug development: where do we go from here? *Br. J. Pharmacol.* **164**, 1207 (2011).
157. Cenci, M. A., Whishaw, I. Q. & Schallert, T. Animal models of neurological deficits: How relevant is the rat? *Nat. Rev. Neurosci.* **3**, 574–579 (2002).
158. Floyd, C. L., Golden, K. M., Black, R. T., Hamm, R. J. & Lyeth, B. G. Craniectomy position affects morris water maze performance and hippocampal cell loss after parasagittal fluid percussion. *J. Neurotrauma* **19**, 303–316 (2002).
159. Albert-Weissenberger, C. & Sirén, A. L. Experimental traumatic brain injury. *Exp. Transl. Stroke Med.* **2**, 1–8 (2010).
160. Kim, Y., Fu, A. H., Tucker, L. B., Liu, J. & McCabe, J. T. Characterization of controlled cortical impact devices by high-speed image analysis. *J. Neurosci. Res.* **96**, 501–511 (2018).
161. Franze, K., Janmey, P. A. & Guck, J. Mechanics in neuronal development and repair. *Annu. Rev. Biomed. Eng.* **15**, 227–251 (2013).
162. Bilston, L. E. Brain Tissue Mechanical Properties. in *Biomechanics of the Brain* (ed. Miller, K.) 69–89 (Springer US, 2011). doi:10.1007/978-1-4419-9997-9_4
163. Buddaya, S. *et al.* Mechanical properties of gray and white matter brain tissue by indentation. in *Physiology & behavior* **46**, 318–330 (2015).
164. Jin, X., Zhu, F., Mao, H., Shen, M. & Yang, K. H. A comprehensive experimental study on material properties of human brain tissue. *J. Biomech.* **46**, 2795–2801 (2013).
165. Bodnar, C. N., Roberts, K. N., Higgins, E. K. & Bachstetter, A. D. A Systematic Review of Closed Head Injury Models of Mild Traumatic Brain Injury in Mice and Rats. *J. Neurotrauma* **36**, 1683–1706 (2019).
166. Morrison, B., Saatman, K. E., Meaney, D. F. & McIntosh, T. K. In vitro central nervous system models of mechanically induced trauma: A review. *J. Neurotrauma* **15**, 911–928 (1998).
167. Krieg, M. *et al.* Atomic force microscopy-based mechanobiology. *Nat. Rev. Phys.* **1**, 41–57 (2019).
168. Haase, K. & Pelling, A. E. Investigating cell mechanics with atomic force microscopy. *J. R. Soc. Interface* **12**, (2015).
169. Cattin, C. J. *et al.* Mechanical control of mitotic progression in single animal cells. *Proc. Natl. Acad. Sci. U. S. A.* **112**, 11258–11263 (2015).
170. Magdesian, M. H. *et al.* Atomic force microscopy reveals important differences in axonal resistance to injury. *Biophys. J.* **103**, 405–414 (2012).
171. Shrirao, A. B. *et al.* Microfluidic platforms for the study of neuronal injury in vitro. *Biotechnology and Bioengineering* **115**, 815–830 (2018).
172. Feng, C. *et al.* Cyclic mechanical tension reinforces DNA damage and activates the p53-p21-Rb pathway to induce premature senescence of nucleus pulposus cells. *Int. J. Mol. Med.* **41**, 3316–3326 (2018).
173. Skotak, M., Wang, F. & Chandra, N. An in vitro injury model for SH-SY5Y neuroblastoma cells: Effect of strain and strain rate. *J. Neurosci. Methods* **205**, 159–168 (2012).

174. Zhu, G., Qian, Y., Wu, W. & Li, R. Negative effects of high mechanical tensile strain stimulation on chondrocyte injury in vitro. *Biochem. Biophys. Res. Commun.* **510**, 48–52 (2019).
175. Dollé, J.-P., Morrison, B., Schloss, R. S. & Yarmush, M. L. Brain-on-a-chip microsystem for investigating traumatic brain injury: Axon diameter and mitochondrial membrane changes play a significant role in axonal response to strain injuries. *TECHNOLOGY* **02**, 106–117 (2014).
176. Di Pietro, V. *et al.* S100B and Glial Fibrillary Acidic Protein as Indexes to Monitor Damage Severity in an In Vitro Model of Traumatic Brain Injury. *Neurochem. Res.* **40**, 991–999 (2015).
177. Liu, W. *et al.* Ablation of caspase-1 protects against TBI-induced pyroptosis in vitro and in vivo. *J. Neuroinflammation* **15**, (2018).
178. Xu, Z. *et al.* Sesamin protects SH-SY5Y cells against mechanical stretch injury and promoting cell survival. *BMC Neurosci.* **18**, 1–10 (2017).
179. Jing, Y. *et al.* Neuroprotective Effects of Serpina3k in Traumatic Brain Injury. *Front. Neurol.* **10**, 1–11 (2019).
180. López-García, I. *et al.* Development of a stretch-induced neurotrauma model for medium-throughput screening in vitro: identification of rifampicin as a neuroprotectant. *Br. J. Pharmacol.* **175**, 284–300 (2018).
181. McKinney, J. S., Willoughby, K. A., Liang, S. & Ellis, E. F. Stretch-induced injury of cultured neuronal, glial, and endothelial cells: Effect of polyethylene glycol-conjugated superoxide dismutase. *Stroke* **27**, 934–940 (1996).
182. Chierto, E. *et al.* Mechanical Stretch of High Magnitude Provokes Axonal Injury, Elongation of Paranodal Junctions, and Signaling Alterations in Oligodendrocytes. *Mol. Neurobiol.* **56**, 4231–4248 (2019).
183. Ergir, E., Bachmann, B., Redl, H., Forte, G. & Ertl, P. Small force, big impact: Next generation organ-on-a-chip systems incorporating biomechanical cues. *Front. Physiol.* **9**, 1–8 (2018).
184. Tovar-Lopez, F. *et al.* A microfluidic system for studying the effects of disturbed flow on endothelial cells. *Front. Bioeng. Biotechnol.* **7**, 1–7 (2019).
185. Lu, H. *et al.* Microfluidic shear devices for quantitative analysis of cell adhesion. *Anal. Chem.* **76**, 5257–5264 (2004).
186. Shemesh, J. *et al.* Flow-induced stress on adherent cells in microfluidic devices. *Lab Chip* **15**, 4114–4127 (2015).
187. Zhang, X., Huk, D. J., Wang, Q., Lincoln, J. & Zhao, Y. A microfluidic shear device that accommodates parallel high and low stress zones within the same culturing chamber. *Biomicrofluidics* **8**, 054106 (2014).
188. Gladilin, E. *et al.* TGFβ-induced cytoskeletal remodeling mediates elevation of cell stiffness and invasiveness in NSCLC. *Sci. Rep.* **9**, 1–12 (2019).
189. Armistead, F. J., Gala De Pablo, J., Gadêlha, H., Peyman, S. A. & Evans, S. D. Cells Under Stress: An Inertial-Shear Microfluidic Determination of Cell Behavior. *Biophys. J.* **116**, 1127–1135 (2019).
190. Kohles, S. S., Nève, N., Zimmerman, J. D. & Tretheway, D. C. Mechanical stress analysis of microfluidic environments designed for isolated biological cell investigations. *J. Biomech. Eng.* **131**, (2009).
191. Lanotte, L. *et al.* Red cells' dynamic morphologies govern blood shear thinning under

microcirculatory flow conditions. *Proc. Natl. Acad. Sci. U. S. A.* **113**, 13289–13294 (2016).
192. Guck, J. *et al.* Optical deformability as an inherent cell marker for testing malignant transformation and metastatic competence. *Biophys. J.* **88**, 3689–3698 (2005).
193. Yap, Y. C., Dickson, T. C., King, A. E., Breadmore, M. C. & Guijt, R. M. Microfluidic culture platform for studying neuronal response to mild to very mild axonal stretch injury. *Biomicrofluidics* **8**, (2014).
194. Sticker, D., Lechner, S., Jungreuthmayer, C., Zanghellini, J. & Ertl, P. Microfluidic Migration and Wound Healing Assay Based on Mechanically Induced Injuries of Defined and Highly Reproducible Areas. *Anal. Chem.* **89**, 2326–2333 (2017).
195. Siddique, R. & Thakor, N. Investigation of nerve injury through microfluidic devices. *J. R. Soc. Interface* **11**, (2014).
196. Chen, Y. C., Smith, D. H. & Meaney, D. F. In-vitro approaches for studying blast-induced traumatic brain injury. *Journal of Neurotrauma* **26**, 861–876 (2009).
197. VandeVord, P. J. *et al.* Up-regulation of reactivity and survival genes in astrocytes after exposure to short duration overpressure. *Neurosci. Lett.* **434**, 247–252 (2008).
198. Effgen, G. B. *et al.* A multiscale approach to blast neurotrauma modeling: Part II: Methodology for inducing blast injury to in vitro models. *Front. Neurol.* **FEB**, 1–10 (2012).
199. Arun, P. *et al.* Studies on blast traumatic brain injury using in-vitro model with shock tube. *Neuroreport* **22**, 379–384 (2011).
200. Logan, N. J., Arora, H. & Higgins, C. A. Evaluating primary blast effects in vitro. *J. Vis. Exp.* **2017**, 1–7 (2017).
201. Panzer, M. B. *et al.* A multiscale approach to blast neurotrauma modeling: Part I - development of novel test devices for in vivo and in vitro blast injury models. *Front. Neurol.* **MAR**, 1–11 (2012).
202. Estrada, J. B., Barajas, C., Henann, D. L., Johnsen, E. & Franck, C. High strain-rate soft material characterization via inertial cavitation. *J. Mech. Phys. Solids* **112**, 291–317 (2018).
203. Wu, Y. T. & Adnan, A. Effect of Shock-Induced Cavitation Bubble Collapse on the damage in the Simulated Perineuronal Net of the Brain. *Sci. Rep.* **7**, (2017).
204. Li, D. *et al.* Response of Single Cells to Shock Waves and Numerically Optimized Waveforms for Cancer Therapy. *Biophys. J.* **114**, 1433–1439 (2018).
205. Vogel, E. W. *et al.* Direct Observation of Low Strain, High Rate Deformation of Cultured Brain Tissue During Primary Blast. *Ann. Biomed. Eng.* **48**, 1196–1206 (2020).
206. Patterson, L. H. C. *et al.* Inertial flow focusing: a case study in optimizing cellular trajectory through a microfluidic MEMS device for timing-critical applications. *Biomed. Microdevices* **22**, 1–12 (2020).
207. Patterson, L. H. C. *et al.* Investigating Cellular Response to Impact with a Microfluidic MEMS Device. *J. Microelectromechanical Syst.* **29**, 14–24 (2020).
208. Walker, J. L. *et al.* Controlled Single-Cell Compression With a High-Throuhgput MEMS Actuator. *J. Microelectromechanical Syst.* 1–7 (2020). doi:10.1109/JMEMS.2020.3005514
209. Lanzicher, T. *et al.* The cardiomyopathy lamin A/C D192G mutation disrupts whole-cell biomechanics in cardiomyocytes as measured by atomic force microscopy loading-unloading curve analysis. *Sci. Rep.* **5**, (2015).

210. Wang, G. *et al.* Stiffness Dependent Separation of Cells in a Microfluidic Device. *PLoS One* **8**, (2013).
211. Mahajan, G., Lee, M. Y. & Kothapalli, C. Biophysical and biomechanical properties of neural progenitor cells as indicators of developmental neurotoxicity. *Arch. Toxicol.* **93**, 2979–2992 (2019).
212. Itoh, T. *et al.* Exercise increases neural stem cell proliferation surrounding the area of damage following rat traumatic brain injury. *J. Neural Transm.* **118**, 193–202 (2011).
213. Chirumamilla, S., Sun, D., Bullock, M. R. & Colello, R. J. Traumatic brain injury induced cell proliferation in the adult mammalian central nervous system. *J. Neurotrauma* **19**, 693–703 (2002).
214. Gao, X., Enikolopov, G. & Chen, J. Moderate traumatic brain injury promotes proliferation of quiescent neural progenitors in the adult hippocampus. *Exp. Neurol.* **219**, 516–523 (2009).
215. Wang, X., Seekaew, P., Gao, X. & Chen, J. Traumatic Brain Injury Stimulates Neural Stem Cell Proliferation via Mammalian Target of Rapamycin Signaling Pathway Activation. *eNeuro* **3**, ENEURO.0162-16.2016 (2016).
216. Gao, X. & Chen, J. Moderate traumatic brain injury promotes neural precursor proliferation without increasing neurogenesis in the adult hippocampus. *Exp. Neurol.* **239**, 38–48 (2013).
217. Saha, S., Ji, L., De Pablo, J. J. & Palecek, S. P. Inhibition of human embryonic stem cell differentiation by mechanical strain. *J. Cell. Physiol.* **206**, 126–137 (2006).
218. Streichan, S. J., Hoerner, C. R., Schneidt, T., Holzer, D. & Hufnagel, L. Spatial constraints control cell proliferation in tissues. *Proc. Natl. Acad. Sci.* **111**, 5586–5591 (2014).
219. Li, P. *et al.* High-magnitude compression accelerates the premature senescence of nucleus pulposus cells via the p38 MAPK-ROS pathway. *Arthritis Res. Ther.* **19**, 1–14 (2017).
220. Marlier, Q., Verteneuil, S., Vandenbosch, R. & Malgrange, B. Mechanisms and functional significance of stroke-induced neurogenesis. *Frontiers in Neuroscience* **9**, 1–16 (2015).
221. Rhee, Y. H. *et al.* Neural stem cells secrete factors facilitating brain regeneration upon constitutive Raf-Erk activation. *Sci. Rep.* **6**, 1–16 (2016).
222. Lindvall, O. & Kokaia, Z. Neurogenesis following stroke affecting the adult brain. *Cold Spring Harb. Perspect. Biol.* **7**, 1–20 (2015).
223. Gnanasegaran, N., Govindasamy, V., Kathirvaloo, P., Musa, S. & Abu Kasim, N. H. Effects of cell cycle phases on the induction of dental pulp stem cells toward dopaminergic-like cells. *J. Tissue Eng. Regen. Med.* **12**, e881–e893 (2018).
224. Collins, A. L. *et al.* Transcriptional targets of the schizophrenia risk gene MIR137. *Transl. Psychiatry* **4**, (2014).
225. Park, J. *et al.* A 3D human triculture system modeling neurodegeneration and neuroinflammation in Alzheimer's disease. *Nat. Neurosci.* **21**, 941–951 (2018).
226. Joshi, P. *et al.* 3D-cultured neural stem cell microarrays on a micropillar chip for high-throughput developmental neurotoxicology. *Exp. Cell Res.* **370**, 680–691 (2018).
227. Bar-Kochba, E., Scimone, M. T., Estrada, J. B. & Franck, C. Strain and rate-dependent neuronal injury in a 3D in vitro compression model of traumatic brain injury. *Sci. Rep.* **6**, 1–11 (2016).
228. Geddes, D. M., Cargill, R. S. & Laplaca, M. C. Mechanical Stretch to Neurons Results in a Strain Rate and Magnitude-Dependent Increase in Plasma Membrane Permeability. *J.*

Neurotrauma **20**, 1039–1049 (2003).
229. Gkretsi, V. & Stylianopoulos, T. Cell adhesion and matrix stiffness: Coordinating cancer cell invasion and metastasis. *Front. Oncol.* **8**, (2018).
230. Tse, J. M. *et al.* Mechanical compression drives cancer cells toward invasive phenotype. *Proc. Natl. Acad. Sci. U. S. A.* **109**, 911–916 (2012).
231. Wong, J., Hoe, N. W., Zhiwei, F. & Ng, I. Apoptosis and Traumatic Brain Injury. *Neurocrit. Care* **3**, 177–182 (2005).
232. Aureille, J. *et al.* Nuclear envelope deformation controls cell cycle progression in response to mechanical force. *EMBO Rep.* **20**, 1–11 (2019).
233. Nam, S. *et al.* Cell cycle progression in confining microenvironments is regulated by a growth-responsive TRPV4-PI3K/Akt-p27Kip1 signaling axis. *Sci. Adv.* **5**, (2019).
234. Cheng, G., Tse, J., Jain, R. K. & Munn, L. L. Micro-environmental mechanical stress controls tumor spheroid size and morphology by suppressing proliferation and inducing apoptosis in cancer cells. *PLoS One* **4**, (2009).
235. Delarue, M. *et al.* Compressive stress inhibits proliferation in tumor spheroids through a volume limitation. *Biophys. J.* **107**, 1821–1828 (2014).
236. Desmaison, A., Frongia, C., Grenier, K., Ducommun, B. & Lobjois, V. Mechanical stress impairs mitosis progression in multi-cellular tumor spheroids. *PLoS One* **8**, 4–13 (2013).
237. Cho, S. *et al.* Mechanosensing by the Lamina Protects against Nuclear Rupture, DNA Damage, and Cell-Cycle Arrest. *Dev. Cell* **49**, 920-935.e5 (2019).
238. Lenz, M., Muller, F. J., Zenke, M. & Schuppert, A. Principal components analysis and the reported low intrinsic dimensionality of gene expression microarray data. *Sci. Rep.* **6**, 1–11 (2016).
239. Bushati, N., Smith, J., Briscoe, J. & Watkins, C. An intuitive graphical visualization technique for the interrogation of transcriptome data. *Nucleic Acids Res.* **39**, 7380–7389 (2011).
240. Claverie, J. M. Computational methods for the identification of differential and coordinated gene expression. *Hum. Mol. Genet.* **8**, 1821–1832 (1999).
241. Mutch, D. M., Berger, A., Mansourian, R., Rytz, A. & Roberts, M. A. The limit fold change model: A practical approach for selecting differentially expressed genes from microarray data. *BMC Bioinformatics* **3**, 1–11 (2002).
242. Ao, L. *et al.* Identification of reproducible drug-resistance-related dysregulated genes in small-scale cancer cell line experiments. *Sci. Rep.* **5**, 1–12 (2015).
243. Subramanian, A. *et al.* Gene set enrichment analysis: A knowledge-based approach for interpreting genome-wide expression profiles. *Proc. Natl. Acad. Sci. U. S. A.* **102**, 15545–15550 (2005).
244. Daly, M. J. *et al.* PGC-1α-responsive genes involved in oxidative phosphorylation are coordinately downregulated in human diabetes. *Nat. Genet.* **34**, 267–273 (2003).
245. Malterer, M. B., Glass, S. J. & Newman, J. P. Interferon-stimulated genes: A complex web of host defenses. *Annu. Rev. Immunol.* **44**, 735–745 (2014).
246. Bailey, C. C., Zhong, G., Huang, I. C. & Farzan, M. IFITM-family proteins: The cell's first line of antiviral defense. *Annu. Rev. Virol.* **1**, 261–283 (2014).
247. Diamond, M. S. & Farzan, M. The broad-spectrum antiviral functions of IFIT and IFITM proteins. *Nat. Rev. Immunol.* **13**, 46–57 (2013).
248. Li, K. *et al.* IFITM Proteins Restrict Viral Membrane Hemifusion. *PLoS Pathog.* **9**, (2013).

249. Tanaka, S. S., Yamaguchi, Y. L., Tsoi, B., Lickert, H. & Tam, P. P. L. IFITM/mil/fragilis family proteins IFITM1 and IFITM3 play distinct roles in mouse primordial germ cell homing and repulsion. *Dev. Cell* **9**, 745–756 (2005).
250. Lange, U. C. *et al.* Normal Germ Line Establishment in Mice Carrying a Deletion of the Ifitm/Fragilis Gene Family Cluster. *Mol. Cell. Biol.* **28**, 4688–4696 (2008).
251. Yánez, D. C., Ross, S. & Crompton, T. The IFITM protein family in adaptive immunity. *Immunology* **159**, 365–372 (2020).
252. Sebastian, A. *et al.* Comparative transcriptomics identifies novel genes and pathways involved in post-traumatic osteoarthritis development and progression. *Int. J. Mol. Sci.* **19**, 1–16 (2018).
253. Ibi, D. *et al.* Astroglial IFITM3 mediates neuronal impairments following neonatal immune challenge in mice. *Glia* **61**, 679–693 (2013).
254. Xu, Y., Yang, G. & Hu, G. Binding of IFITM1 enhances the inhibiting effect of caveolin-1 on ERK activation. *Acta Biochim. Biophys. Sin. (Shanghai).* **41**, 488–494 (2009).
255. Martínez, M., Martínez, N. A., Miranda, J. D., Maldonado, H. M. & Ortiz, W. I. S. Caveolin-1 regulates P2Y2 receptor signaling during mechanical injury in human 1321N1 astrocytoma. *Biomolecules* **9**, (2019).
256. Rosati, A. *et al.* BAG3 promotes pancreatic ductal adenocarcinoma growth by activating stromal macrophages. *Nat. Commun.* **6**, 1–11 (2015).
257. Lipponen, A., Paananen, J., Puhakka, N. & Pitkanen, A. Analysis of Post-Traumatic Brain Injury Gene Expression Signature Reveals Tubulins, Nfe2l2, Nfkb, Cd44, and S100a4 as Treatment Targets. *Sci. Rep.* **6**, (2016).
258. Spilianakis, C. *et al.* CIITA regulates transcription onset via Ser5-phosphorylation of RNA Pol II. *EMBO J.* **22**, 5125–5136 (2003).
259. Platanias, L. C. Mechanisms of type-I- and type-II-interferon-mediated signalling. *Nat. Rev. Immunol.* **5**, 375–386 (2005).
260. Ween, M. P., Oehler, M. K. & Ricciardelli, C. Transforming growth factor-beta-induced protein (TGFBI)/(βig-H3): A matrix protein with dual functions in ovarian cancer. *Int. J. Mol. Sci.* **13**, 10461–10477 (2012).
261. Schoenherr, C. *et al.* Ambra1 spatially regulates Src activity and Src/FAK-mediated cancer cell invasion via trafficking networks. *Elife* **6**, 1–22 (2017).
262. Glazko, G. & Mushegian, A. Measuring gene expression divergence: The distance to keep. *Biol. Direct* **5**, (2010).
263. Pereira, V., Waxman, D. & Eyre-Walker, A. A problem with the correlation coefficient as a measure of gene expression divergence. *Genetics* **183**, 1597–1600 (2009).
264. Kim, C. C., Nakamura, M. C. & Hsieh, C. L. Brain trauma elicits non-canonical macrophage activation states. *J. Neuroinflammation* **13**, 1–12 (2016).
265. Boone, D. R. *et al.* Traumatic brain injury induces long-lasting changes in immune and regenerative signaling. *PLoS One* **14**, (2019).
266. Sell, S. L. *et al.* MicroRNA profiling identifies a novel compound with antidepressant properties. *PLoS One* **14**, 1–19 (2019).
267. Shojo, H., Borlongan, C. V. & Mabuchi, T. Genetic and histological alterations reveal key role of prostaglandin synthase and cyclooxygenase 1 and 2 in traumatic brain injury–induced neuroinflammation in the cerebral cortex of rats exposed to moderate fluid percussion injury. *Cell Transplant.* **26**, 1301–1313 (2017).
268. Witcher, K. G. *et al.* Traumatic brain injury-induced neuronal damage in the

somatosensory cortex causes formation of rod-shaped microglia that promote astrogliosis and persistent neuroinflammation. *Glia* **66**, 2719–2736 (2018).
269. Puhakka, N. *et al.* Chronically dysregulated NOTCH1 interactome in the dentate gyrus after traumatic brain injury. *PLoS One* **12**, 1–24 (2017).
270. Boone, D. K. *et al.* Evidence linking microRNA suppression of essential prosurvival genes with hippocampal cell death after traumatic brain injury. *Sci. Rep.* **7**, 1–11 (2017).
271. Chakraborty, N. *et al.* TBI weight-drop model with variable impact heights differentially perturbs hippocampus-cerebellum specific transcriptomic profile. *Exp. Neurol.* **335**, 113516 (2021).
272. Tweedie, D. *et al.* Cognitive impairments induced by concussive mild traumatic brain injury in mouse are ameliorated by treatment with phenserine via multiple non-cholinergic and cholinergic mechanisms. *PLoS One* **11**, 1–26 (2016).
273. Blaze, J. *et al.* Blast-Related Mild TBI Alters Anxiety-Like Behavior and Transcriptional Signatures in the Rat Amygdala. *Front. Behav. Neurosci.* **14**, 1–14 (2020).
274. Zhang, J. *et al.* Hair follicle miRNAs: a novel biomarker for primary blast Induced-Mild traumatic brain injury. *Biomarkers* **24**, 166–179 (2019).
275. Harper, M. M. *et al.* Blast preconditioning protects retinal ganglion cells and reveals targets for prevention of neurodegeneration following blast-mediated traumatic Brian injury. *Investig. Ophthalmol. Vis. Sci.* **60**, 4159–4170 (2019).
276. Ng, J. M. J. *et al.* Transcriptional insights on the regenerative mechanics of axotomized neurons in vitro. *J. Cell. Mol. Med.* **16**, 789–811 (2012).
277. Brophy, R. H., Rothermich, M. A., Tycksen, E. D., Cai, L. & Rai, M. F. Presence of meniscus tear alters gene expression profile of anterior cruciate ligament tears. *J. Orthop. Res.* **36**, 2612–2621 (2018).
278. Weisz, H. A. *et al.* MicroRNA sequencing of rat hippocampus and human biofluids identifies acute, chronic, focal and diffuse traumatic brain injuries. *Sci. Rep.* **10**, 1–10 (2020).
279. LaRocca, D. *et al. Comparison of serum and saliva miRNAs for identification and characterization of mTBI in adult mixed martial arts fighters*. *PLoS ONE* **14**, (2019).
280. Bolte, A. C. *et al.* Meningeal lymphatic dysfunction exacerbates traumatic brain injury pathogenesis. *Nat. Commun.* **11**, 1–18 (2020).
281. Enam, S. F. *et al.* Evaluation of M2-like macrophage enrichment after diffuse traumatic brain injury through transient interleukin-4 expression from engineered mesenchymal stromal cells. *bioRxiv* 1–24 (2020). doi:10.1101/2020.01.28.918441
282. Vaickus, M. *et al.* Mild Traumatic Brain Injury in Mice Beneficially Alters Lung NK1R and Structural Protein Expression to Enhance Survival after Pseudomonas aeruginosa Infection. *Am. J. Pathol.* **189**, 295–307 (2019).
283. Zhong, J. *et al.* Altered expression of long non-coding RNA and mRNA in mouse cortex after traumatic brain injury. *Brain Res.* **1646**, 589–600 (2016).
284. Chen, C. *et al.* Astrocyte-Specific Deletion of Sox2 Promotes Functional Recovery after Traumatic Brain Injury. *Cereb. Cortex* **29**, 54–69 (2019).
285. Castranio, E. L. *et al.* Gene co-expression networks identify Trem2 and Tyrobp as major hubs in human APOE expressing mice following traumatic brain injury. *Neurobiol. Dis.* **105**, 1–14 (2017).
286. Tweedie, D. *et al.* Mild traumatic brain injury-induced hippocampal gene expressions: The identification of target cellular processes for drug development. *J. Neurosci. Methods*

272, 4–18 (2016).
287. Hsieh, C. L. *et al.* Traumatic brain injury induces macrophage subsets in the brain. *Eur J Immunol* **43**, 2010–2022 (2013).
288. Boone, D. R. *et al.* Effects of AAV-mediated knockdown of nNOS and GPx-1 gene expression in rat hippocampus after traumatic brain injury. *PLoS One* **12**, 1–22 (2017).
289. Ge, X. *et al.* Increased Microglial Exosomal miR-124-3p Alleviates Neurodegeneration and Improves Cognitive Outcome after rmTBI. *Mol. Ther.* **28**, 503–522 (2020).
290. Izzy, S. *et al.* Time-Dependent Changes in Microglia Transcriptional Networks Following Traumatic Brain Injury. *Front. Cell. Neurosci.* **13**, 1–16 (2019).
291. Anderson, G. D. *et al.* Effect of Traumatic Brain Injury, Erythropoietin, and Anakinra on Hepatic Metabolizing Enzymes and Transporters in an Experimental Rat Model. *AAPS J.* **17**, 1255–1267 (2015).
292. White, T. E. *et al.* Gene expression patterns following unilateral traumatic brain injury reveals a local pro-inflammatory and remote anti-inflammatory response. *BMC Genomics* **14**, 1 (2013).
293. Castranio, E. L. *et al.* ABCA1 haplodeficiency affects the brain transcriptome following traumatic brain injury in mice expressing human APOE isoforms. *Acta Neuropathol. Commun.* **6**, 69 (2018).
294. Israelsson, C., Kylberg, A., Bengtsson, H., Hillered, L. & Ebendal, T. Interacting chemokine signals regulate dendritic cells in acute brain injury. *PLoS One* **9**, 1–12 (2014).
295. Geng, Y. *et al.* Overexpression of mechanical sensitive miR-337-3p alleviates ectopic ossification in rat tendinopathy model via targeting IRS1 and Nox4 of tendon-derived stem cells. *J. Mol. Cell Biol.* **12**, 305–317 (2020).
296. Wang, Y. *et al.* DNA microarray reveals novel genes induced by mechanical forces in fetal lung type II epithelial cells. *Pediatr. Res.* **60**, 118–124 (2006).
297. Adam, R. M. *et al.* Mechanical stretch is a highly selective regulator of gene expression in human bladder smooth muscle cells. *Physiol. Genomics* **20**, 36–44 (2005).
298. Najrana, T. *et al.* Mechanical stretch regulates the expression of specific miRNA in extracellular vesicles released from lung epithelial cells. *J. Cell. Physiol.* **235**, 8210–8223 (2020).
299. Uchida, K. *et al.* Microarray analysis of expression of cell death-associated genes in spinal cord cells with cyclic tensile strain. *Neuroprotection Regen. Spinal Cord* **9784431545**, 119–127 (2014).
300. Blumenthal, A. *et al.* Mechanical stress enhances CD9 expression in cultured podocytes. *Am. J. Physiol. - Ren. Physiol.* **308**, F602–F613 (2015).
301. Goto, K. T. *et al.* Hyperocclusion stimulates osteoclastogenesis via CCL2 expression. *J. Dent. Res.* **90**, 793–798 (2011).
302. Reichenbach, M., Reimann, K. & Reuter, H. Gene expression in response to cyclic mechanical stretch in primary human dermal fibroblasts. *Genomics Data* **2**, 335–339 (2014).
303. Weyer, A. D., O'Hara, C. L. & Stucky, C. L. Amplified mechanically gated currents in distinct subsets of myelinated sensory neurons following In Vivo inflammation of skin and muscle. *J. Neurosci.* **35**, 9456–9462 (2015).
304. Rysä, J., Tokola, H. & Ruskoaho, H. Mechanical stretch induced transcriptomic profiles in cardiac myocytes. *Sci. Rep.* **8**, 1–14 (2018).
305. McKenzie, J. A., Bixby, E. C. & Silva, M. J. Differential gene expression from microarray

analysis distinguishes woven and lamellar bone formation in the rat ulna following mechanical loading. *PLoS One* **6**, (2011).
306. Wong, V. W. *et al.* Focal adhesion kinase links mechanical force to skin fibrosis via inflammatory signaling. *Nat. Med.* **18**, 148–152 (2015).
307. Luna, C., Li, G., Liton, P. B., Epstein, D. L. & Gonzalez, P. Alterations in gene expression induced by cyclic mechanical stress in trabecular meshwork cells. *Mol. Vis.* **15**, 534–544 (2009).
308. Mackley, J. R., Ando, J., Herzyk, P. & Winder, S. J. Phenotypic responses to mechanical stress in fibroblasts from tendon, cornea and skin. *Biochem. J.* **396**, 307–316 (2006).
309. Boerma, M. *et al.* Microarray analysis of gene expression profiles of cardiac myocytes and fibroblasts after mechanical stress, ionising or ultraviolet radiation. *BMC Genomics* **6**, 1–10 (2005).
310. Wang, X., Fan, J., Zhang, M., Sun, Z. & Xu, G. Gene Expression Changes under Cyclic Mechanical Stretching in Rat Retinal Glial (Müller) Cells. *PLoS One* **8**, 1–10 (2013).
311. Loverde, J. R., Tolentino, R. E., Soteropoulos, P. & Pfister, B. J. Biomechanical Forces Regulate Gene Transcription During Stretch-Mediated Growth of Mammalian Neurons. *Front. Neurosci.* **14**, 1–15 (2020).
312. Xie, B. *et al.* Chemokine expression in the early response to injury in human airway epithelial cells. *PLoS One* **13**, 1–22 (2018).
313. Aragona, M. *et al. Mechanisms of stretch-mediated skin expansion at single-cell resolution*. *Nature* **584**, (Springer US, 2020).
314. Qin, L., Liu, W., Cao, H. & Xiao, G. Molecular mechanosensors in osteocytes. *Bone Res.* **8**, 1–24 (2020).
315. Meisel, C., Schwab, J. M., Prass, K., Meisel, A. & Dirnagl, U. Central nervous system injury-induced immune deficiency syndrome. *Nat. Rev. Neurosci.* **6**, 775–786 (2005).